Imperial College London

Intracellular Mapping of Functional Chemistry and Nanoparticle Theranostics with Infrared Nano-imaging

George E. Greaves

2024

Department of Physics

Imperial College London

Submitted in part fulfilment of the requirements for the degree of Physics
Doctor of Philosophy of Imperial College London
and the Diploma of Imperial College London

Statement of Originality

The content of this thesis is my own, except where appropriately referenced. Contributions to the work in this thesis made by others, from Imperial College and other institutions, has been appropriately acknowledged.

Copyright statement

Abstract

Nanoscale imaging is key in studying cell function and pathology at the cellular level, but the diffraction limit (~250nm for visible light) poses a barrier. This necessitates the development of advanced imaging techniques such as electron and super-resolution microscopies, which generally require samples to be stained or labelled to operate at their full potential. In the handful of label-free techniques, it can be challenging to obtain chemical information at the nanoscale spatial resolutions required. At the same time, infrared spectroscopy and imaging is routinely used to obtain chemical information in a label-free way, but suffers from poor spatial resolution due to the diffraction limit (here ~3–5μm), rendering it of little value at the cellular level.

This thesis presents advancements in the cellular imaging capabilities of scattering-type scanning near-field optical microscopy (s-SNOM), a scanning probe microscopy technique that is here combined with infrared quantum cascade lasers to image cells with nanoscale (~30nm) spatial resolution and chemical sensitivity. In one of the key results of this thesis, multiple myeloma cells are imaged label-free at several wavelengths to isolate intracellular structures based on the infrared signatures of chemical groups occurring naturally in biomolecules. Several organelles such as mitochondria and endoplasmic reticulum are identified, having never been seen before at this spatial resolution in a directly optical way.

s-SNOM is also demonstrated as a tool to image interactions between cells and nanoparticles used in drug delivery. This has huge potential in nanomedicine, whereby the intracellular biochemical response of cells could be correlated with the uptake of such nanoparticles. Additionally, combining chemical mapping with the topographical information also obtained with s-SNOM is shown to provide a way of determining whether nanoparticles have internalised into cells, which is crucial in evaluating the efficacy of nanomedicines.

This page intentionally left blank

Acknowledgements

I would first like to thank my supervisor Chris Phillips for his support and encouragement over the last four years. I feel very privileged to have had the opportunity to work on this project and it has been a pleasure being part of his lab.

I would also like to thank the many collaborators who have helped shape this project and ensured I had no shortage of interesting samples to investigate in the lab (and explaining their biological relevance!). I'd particularly like to thank Darya Kiryushko for the huge part she played in this, as well as the insight she shared into the worlds of the life sciences, medicine and beyond.

Finally, I would like to thank my amazing girlfriend Annie for being willing to move to London with me in the first place(!), and for all the support throughout.

Contributions

Experiments were designed by Chris Phillips, Alex Porter and Darya Kiryushko with input from George Greaves (the author), all of Imperial College London. The s-SNOM system, quantum cascade laser and detection modules were installed and aligned by the author. s-SNOM and atomic force microscopy (AFM) images were acquired and analysed by the author. Transmission electron microscopy (TEM) images were acquired and analysed by Darya Kiryushko and Pedro Machado of King's College London. Infrared absorption spectra were acquired and analysed by the author.

The multiple myeloma cells used for s-SNOM and TEM imaging were produced by Darya Kiryushko from stocks donated by Holger Auner of Imperial College London. The formalin-fixed paraffin-embedded multiple myeloma cells used for generating infrared absorption spectra were prepared by Sandra Iles (formerly of Imperial College London) and the author. The hippocampal neurons used for s-SNOM and TEM imaging and generating infrared absorption spectra were prepared by Darya Kiryushko, Corinne Morfill (Imperial College London), Pedro Machado and Leanne Allison (King's College London). The malignant glioma cells used for s-SNOM imaging were prepared by Jonny Taylor (Imperial College London) and Darya Kiryushko.

Publications, conferences and outreach

Publications

Greaves, G.E., Kiryushko, D., Auner, H.W., Porter, A.E. and Phillips, C.C.

'Label-free nanoscale mapping of intracellular organelle chemistry'.

Communications Biology **6**(1)**:** p. 583 (2023).

https://doi.org/10.1038/s42003-023-04943-7

Greaves, G.E., Allison, L., Machado, P., Morfill, C., Fleck, R.A., Porter , A.E. and Phillips, C.C.

'Infrared nanoimaging of neuronal ultrastructure and nanoparticle interaction with cells'.

Nanoscale, **16**, 6190-6198 (2024).

https://doi.org/10.1039/D3NR04948E

Conferences

American Physical Society March Meeting 2023, Las Vegas

'Label-free nanoscale chemical mapping of intracellular structures'

Bulletin of the American Physical Society (2023)

Poster Presentation

BioMedEng 2022, University College London

'Mid-infrared Chemical Nano-imaging and Mapping with s-SNOM'

Poster Presentation

Royal Microscopical Society Frontiers in Bioimaging 2022, University of Birmingham

'Mid infrared chemical nanoimaging with s-SNOM'

Speaker

Outreach

Cancer Research UK Technology Away Day 2019, Francis Crick Institute, London

's-SNOM imaging for cancer research'

Invited Speaker

Table of Contents

List of figures

Chapter 1

Introduction

Advances in the fields of the life sciences and medicine have long been linked to improvements in the ability to image biological systems. Such improvements are typically in the spatial resolution of imaging systems, enabling the imaging of smaller objects in greater detail, but also in specificity, whereby components of biological systems can be identified by, for example, their chemical make-up.

This thesis concerns advancements in the nanoscale imaging of cells and intracellular structures using infrared (IR) scattering-type scanning near-field optical microscopy (s-SNOM). It explores the key advantages of this technique, chiefly the ability to map the functional chemistry in systems at the nanoscale without having to apply stains and/or labels. Applications in nanomedicine are also demonstrated by using s-SNOM to image interactions between cells and nanoparticles used for drug delivery, whilst simultaneously mapping the cell chemistry.

This chapter first introduces the diffraction limit, a key concept that sets a limit on the resolving power of many microscopies and necessitates the development of advanced techniques. The most relevant

of these advanced techniques are discussed, namely electron microscopy (EM), super-resolution microscopy and two scanning probe microscopies similar in operation to s-SNOM. Some of the shortcomings of these techniques are introduced here, but much of the detail is left for chapter 4.

1.1 The imaging landscape

1.1.1 Diffraction-limited imaging

The maximum spatial resolution achievable with standard optical microscopes (that is, not EM, nor the super-resolution or scanning probe techniques discussed later) is set by a property of light known as diffraction. This stipulates that the spatial resolution of an imaging system is limited in a way that is tied to the wavelength of light it uses. In the simple case of a point source object imaged with a lens with a circular aperture (figure 1.1 (a)), the resulting image is not point-like as the object is, but, due to diffraction, it forms a pattern known as an Airy disc.

If two point-sources are sufficiently close together, their Airy discs overlap such that the two objects cannot be distinguished. Often the minimum separation at which objects are still resolvable is given as the Rayleigh criterion, whereby the centre of the Airy disk of one source coincides with the first minimum of the other source [1]. This is shown in figure 1.1 (b), where the intensity profiles shown are for lines through the centre of each Airy disc.

Closely related to the Rayleigh criterion, the diffraction-limited spatial resolution of an imaging system, r, is often given as the Abbe limit

$$r = \frac{\lambda}{2 \cdot NA} \tag{1.1}$$

where λ is the wavelength of the light and NA is the numerical aperture of the imaging system [2]. Consequently, the spatial resolution of an imaging system can be improved by using light of a shorter wavelength and/or by increasing the numerical aperture of the system (for example, by increasing the aperture size of lenses).

The diffraction limit affects a range of imaging systems, including those that use visible light, as well as IR microscopies used for chemical mapping. For light in the visible part of the electromagnetic

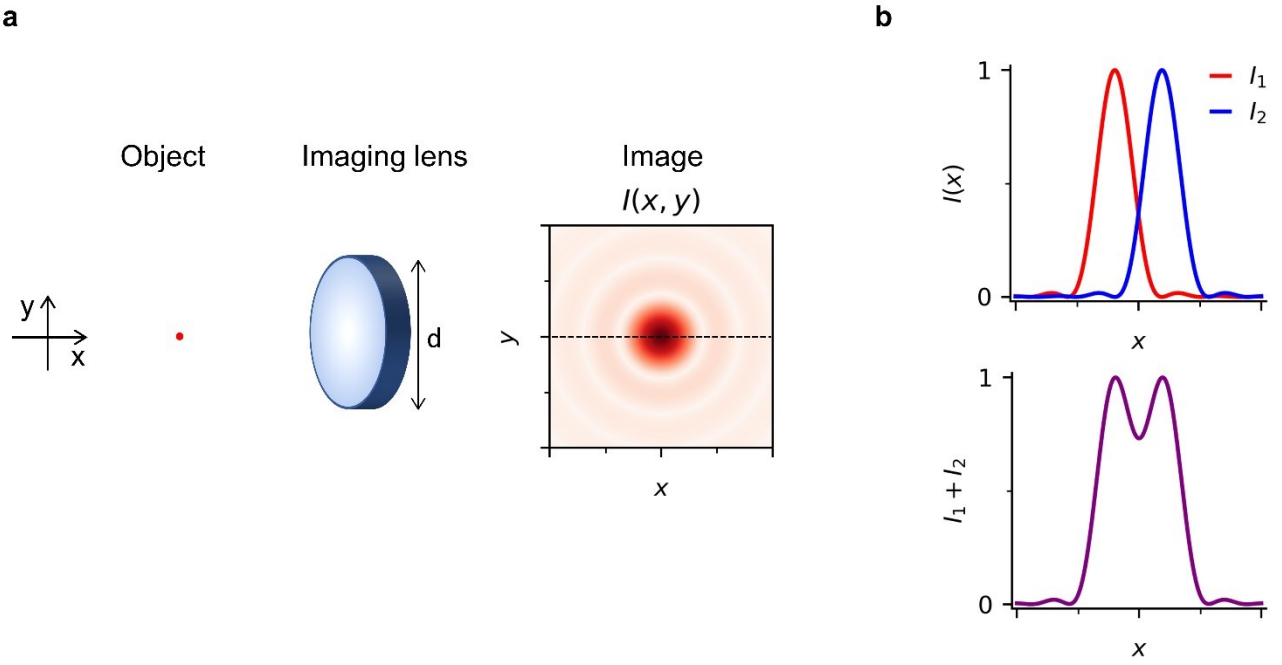

Figure 1.1 Diffraction-limited imaging. ***(a)*** *A point source imaged by a lens of finite aperture, d, produces a pattern at the image plane known as an Airy disc.* ***(b)*** *Intensity profiles along lines through the centres of Airy discs (shown in (a)) for two point sources separated by the distance from the centre of an Airy disc to its first minimum. This separation is known as the Rayleigh criterion.*

spectrum, the diffraction limit is approximately 250nm, varying with the wavelength of the light and the configuration and types of optical elements used. In the context of bioimaging, this is generally sufficient to resolve individual cells, and even identify large structures such as nuclei, but there is a great wealth of intracellular structures that cannot be resolved at this spatial resolution. Many fluorescence-based techniques are similarly limited, since they generally use fluorescent labels that operate in the visible, near-IR and near-UV parts of the electromagnetic spectrum [3]. IR microscopies operate at much longer wavelengths, with 5–10μm being common. Thus, the diffraction limit imposes a much more severe limit on the spatial resolution of IR microscopies, and it is therefore challenging to resolve intracellular structures.

1.1.2 Electron microscopy

EM is an analogue of optical microscopy that uses electrons instead of photons and electromagnetic lenses instead of refractive and reflective optical components. The extremely short wavelength of electrons means that EM has a far-superior spatial resolution compared to standard optical microscopies. One of the earliest applications of EM, in the late 1930s, was the imaging of viruses

[4, 5]. This resulted in the coining of the term “ultrastructure”, the fine structure of cells that requires an imaging technique such as EM, or one with comparable spatial resolution, to be visualised. EM is now widespread in the life sciences and medicine and allows routine visualisation of cell ultrastructure and nanomaterials [6, 7].

Several EM techniques exist to suit a variety of sample types. Transmission electron microscopy (TEM) is generally performed on sections of cells and tissues that are chemically fixed, embedded in epoxy resin and sliced thinly (~100nm) using an ultramicrotome [8]. As its name suggests, this technique measures the transmission of electrons through a sample, which is generally stained with heavy metals such as osmium tetroxide (OsO_4), uranyl acetate and lead citrate to generate electron contrast.

Another common technique, scanning electron microscopy (SEM), relies on detecting electrons scattered off samples. Like TEM, samples prepared for SEM are generally chemically fixed and stained with heavy metals but differ in that they need not be embedded in resin [9]. This means SEM can be used for imaging whole cells grown on substrates [10].

In electron cryomicroscopy (cryo-EM), samples are neither chemically fixed nor stained with heavy metals. Instead, they are frozen at cryogenic temperatures in an attempt to better preserve biological structures. The lack of staining means that electron contrast is reduced and that samples are more easily damaged in the electron beam, so a low power beam is used [11]. As such, images are generally quite noisy, so complex image processing is required to interpret images.

Identification of specific molecules and structures can be achieved in EM through immunolabelling, whereby an antibody tag attaches to an antigen target in the specimen. A metallic nanoparticle (NP) is conjugated to the antibody tag to provide contrast in EM images [12, 13]. Other techniques such as energy dispersive X-ray spectroscopy (EDX) and electron energy loss spectroscopy (EELS) can be combined with EM to facilitate chemical identification within samples, but it can be challenging to achieve this at the nanoscale resolutions required without the electron beam damaging samples [14, 15].

Three-dimensional techniques that allow entire cells to be resolved in three dimensions are emerging in EM. One such technique, electron cryotomography, involves rotating a sample between capturing successive images and using reconstruction algorithms to generate a 3D image [11]. Other techniques include ion-beam milling and serial-block face EM, which iteratively image with SEM and remove the top layer of a sample using an ion beam or an ultramicrotome, respectively. Three-dimensional imaging is outside of the scope of this thesis[1], but it is worth noting that, in principle, s-SNOM could be combined with ion-beam milling for three-dimensional imaging.

1.1.3 Super-resolution microscopy

Fluorescence microscopy makes use of a wide variety of fluorescent labels that bind to molecules and structures of interest in biological systems. By pumping the labels to an excited state and measuring the fluorescence emission, the target molecules and structures are visualised. Such fluorescent labels typically operate in the visible, near-IR and near-UV parts of the electromagnetic spectrum and thus the spatial resolution of many fluorescent techniques is limited by diffraction to ~250nm [3].

A handful of so-called super-resolution techniques surpass the diffraction limit, however [16, 17]. One group of such techniques, structured illumination microscopy (SIM), uses a spatially structured illumination which generates interference patterns. Careful analysis results in SIM techniques surpassing the diffraction limit, and generally yields an improvement in resolution by roughly a factor of two [18].

Another group of techniques, stimulated emission depletion microscopy (STED), beats diffraction using a ‘depletion beam’ that creates a doughnut-shaped region in the sample where fluorescence is depleted, leaving a central region of sub-diffraction size where fluorescence occurs [19, 20]. Resolutions down to 20nm have been observed with STED [21].

A third group of techniques, single-molecule localisation microscopy (SMLM), uses a series of diffraction-limited images to localise fluorescent molecules by computationally estimating the

[1] Three-dimensional imaging of entire cell volumes is outside of the scope of this thesis. Imaging the surface of whole cells in three-dimensions, without imaging the internal volume, is covered in chapter 6.

locations of the centres of the point-spread functions (PSFs) of the emission from fluorescent labels (that is, the diffraction patterns detected from fluorescence emissions). Such techniques use the fact that fluorescent molecules switch between on and off states, so each diffraction-limited image contains the emission from only a subset of them. The more images (and hence, photons) collected, the more accurately the centres of the PSFs can be located [22]. SMLM techniques include photoactivated localisation microscopy (PALM) [23, 24] and stochastic optical reconstruction microscopy (STORM) [25], the main difference being the fluorescent labels used and the mechanism for switching them on and off.

1.1.4 Other notable fluorescence-based imaging techniques

There are a number of other notable fluorescence-based techniques that, whilst unable to achieve as high spatial resolution as s-SNOM, EM and super-resolution microscopies, are worth including in this review due to their widespread use across the life sciences and medicine.

Confocal and light sheet microscopies

Confocal microscopy involves using pinholes to block out-of-focus light and thus improve the spatial resolution compared to an ordinary fluorescence-based microscope [26]. One such technique, confocal laser scanning microscopy, uses a single pinhole such that only one part of a sample is illuminated at a time. 2D (or 3D) imaging therefore requires raster scanning over the entire specimen [26]. Another technique, spinning disk confocal microscopy, uses a spinning disk with many pinholes to speed up image acquisition time and thus to reduce the effect of phototoxicity and photobleaching [27].

Another widely used fluorescence-based imaging technique, light sheet microscopy, involves illuminating a sample with a sheet of light in a plane whose normal is parallel to the image axis [28]. Since only a thin section of the sample is illuminated at any time, the axial resolution of images is improved in comparison to that of ordinary fluorescence microscopes, and the effects of phototoxicity and photobleaching are reduced [29].

Both confocal and light sheet microscopies are diffraction limited imaging techniques, so their lateral spatial resolutions are restricted to approximately 200nm, but they are both extremely powerful and versatile imaging techniques that enable three dimensional imaging of fixed and living cells [27, 29].

Fluorescence lifetime imaging and fluorescence resonance energy transfer microscopies

As an alternative to conventional fluorescence microscopies, whereby the intensity of fluorophore emission is used to generate image contrast, fluorescence lifetime imaging microscopy (FLIM) instead uses the excited state lifetime of fluorophores. This alternative mechanism for generating contrast can be, for example, sensitive to the changes in molecular environments that can't be detected with conventional fluorescence techniques [30]. There are also significant practical advantages such as FLIM being largely unaffected by fluorophore intensity and concentration and the phenomenon of photobleaching [31, 32]. FLIM can be experimentally realised by adapting confocal or light sheet microscopy techniques [33, 34]. In such cases, of course, the spatial resolution of images is diffraction limited. However, efforts have been made to combine FLIM with super-resolution techniques to enable sub-diffraction FLIM imaging, both with SMLM [35] and STED techniques [36].

Fluorescence resonance energy transfer (FRET) – also known as Förster resonance energy transfer – is a phenomenon in which energy is transferred from a donor fluorophore to an acceptor fluorophore over a short distance (typically several nanometres) [37]. The efficiency of the energy transfer is dependent on the distance between the fluorophores, so measuring the FRET efficiency allows one to infer the proximity of molecules of interest to one another. FRET-based imaging can therefore be used to investigate protein-protein interactions [38], lipid-protein interactions [39] and cellular signalling pathways [40], amongst many other biological systems and processes. FRET can also be combined with FLIM to study interactions between proteins with high spatial and temporal resolution [41, 42]. More recently, FRET has been combined with STED to enable sub-diffraction imaging, demonstrated with the imaging of primary neurons [43].

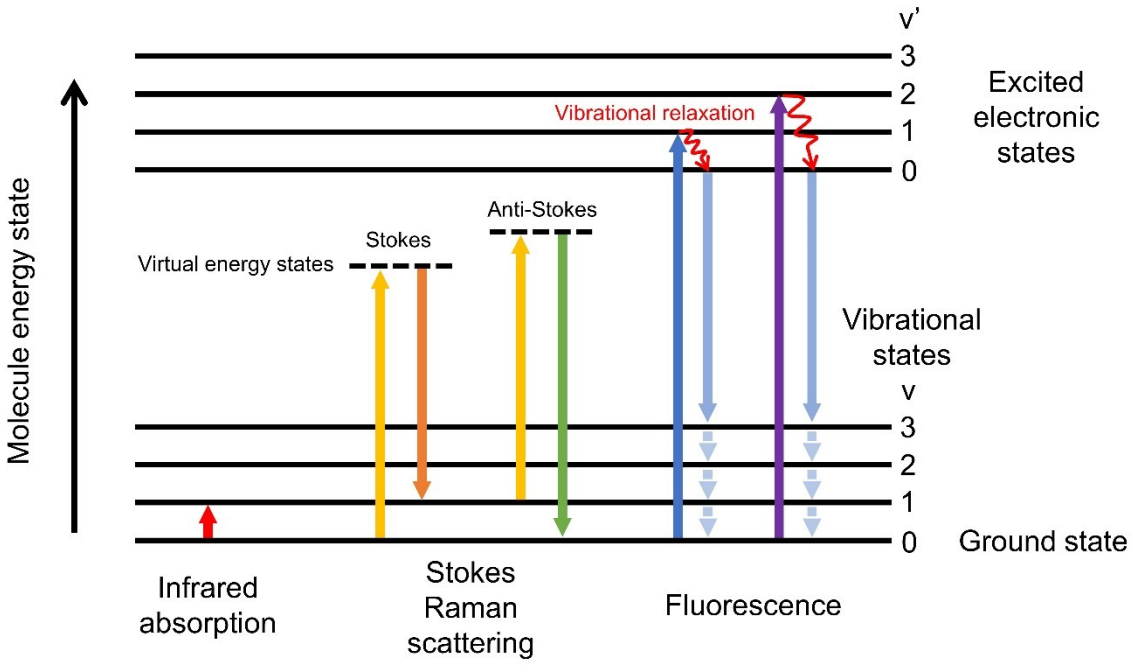

Figure 1.2 Molecular energy level transitions. *Representative molecular energy level transitions in infrared imaging, Raman imaging and fluorescence microscopy.*

1.1.5 Infrared imaging

IR imaging techniques do not require samples to be stained or labelled to generate image contrast. Instead, they exploit vibrational modes of chemical moieties found naturally in specimens. In addition to providing contrast for the morphological identification of structures, probing these vibrational modes enables quantitative mapping of functional chemistry in biological specimens. Vibrational modes can be probed by exciting them directly with IR wavelengths or indirectly through Stokes-Raman scattering (figure 1.2). The former has the significant advantage of using longer wavelength photons with lower energies. This can reduce the exposure of the sample to radiation and thus reduce the potential for damage.

A common infrared imaging technique uses a Fourier transform infrared (FTIR) spectrometer (a technique widely used for generating infrared spectra, formally introduced in section 2.4.2) coupled to a focal plane array (FPA) detector. This has been employed to investigate a variety of biological tissues [44] and its chemical sensitivity gives rise to applications in disease diagnosis [45].

The advent of quantum cascade lasers (QCLs), which offer low noise, single wavelength light tuneable throughout the infrared, has resulted in the emergence of QCL microscope systems that

offer high throughput imaging compared to their FTIR microscope counterparts [46]. Amongst the types of samples investigated with such systems are tissue sections [47], including tissue micro arrays, which are a convenient way of imaging sections of tissues from many specimens at once [48].

Efforts have also been made to develop lower cost, clinic-friendly infrared imaging systems. One such system uses a Globar thermal source instead of a QCL and a microbolometer detector rather than a liquid nitrogen-cooled mercury cadmium telluride (MCT) detector [49]. However, the superior signal-to-noise ratio obtained with FTIR- and QCL-based systems means they are still the most popular choices.

Long imaging wavelengths (several micrometres) mean that the spatial resolutions of IR techniques are generally severely restricted by the diffraction limit. However, a family of scanning probe microscopy (SPM) techniques, discussed below, have been developed that combine the nanoscale resolving power of SPM with the chemical sensitivity of IR imaging techniques.

1.1.6 Scanning probe microscopy

Atomic force microscopy

Atomic force microscopy (AFM) involves raster scanning a sharp probe across a sample to obtain topographical and mechanical information. Whilst originally developed to investigate solid-state samples [50], there is now a multitude of imaging modes to suit all types of biological specimens, from membranes [51, 52] and pore complexes [53, 54], all the way up to whole cells [55] and tissues [56], making it a highly versatile and widely used nanoscale imaging tool [57].

Identifying and monitoring physiological changes to subcellular structures is made possible with AFM through measurements of morphology with sub-nanometre spatial resolution, as well as measuring mechanical properties such as stiffness, adhesion and roughness [57]. To add to this, a family of techniques, all based on AFM, have been developed that combine the chemical sensitivity of infrared spectroscopy with the spatial resolution of SPM. This enables identification and monitoring of subcellular structures through their optical properties [58], rather than through the use of stains and labels as in EM and super-resolution microscopies.

Tip-enhanced Raman spectroscopy

One such IR SPM technique, tip-enhanced Raman spectroscopy (TERS), probes vibrational modes through Stokes-Raman scattering [59], and has been applied to a number of biological systems [60]. Examples include isolated biological systems such as amyloid fibrils [61] and lipid monolayers [62], as well as complex systems such as viruses [63], bacteria [64] and human cells [65]. One practical issue associated with TERS is that exciting vibrational modes with higher energy photons delivers an unnecessarily large energy dose to samples compared with IR wavelengths [60]. Generally, TERS is used to generate locally resolved IR absorption spectra of samples, rather than chemically mapping biological systems.

Sub-nanometre spatial resolution TERS has been demonstrated [66, 67], however this relies on matching molecular vibrational modes with the plasmon resonance of nanocavities between sharp imaging probes and a sample surface. Additional technical challenges such as tip-to-tip variability and sample drift at ambient temperatures make high resolution TERS challenging to realise [68]. Furthermore, the low Raman scattering cross sections of biological molecules such as proteins and DNA make their detection challenging in comparison to the commonly investigated resonant dyes [68].

Photothermal induced resonance AFM (AFM-IR)

Another related technique, photothermal induced resonance (PTIR) AFM, also known as AFM-IR, illuminates samples with IR light and the induced thermal expansion of the sample is detected in the deflection of the AFM tip. It has benefitted from the technical advancement in mid-infrared light sources, namely quantum cascade lasers (QCLs) [69]. It has been used to image a handful of biological systems [68], including whole breast cancer cells [70, 71], red blood cells [72], fibroblast cells [73], viruses [74] and cervical cancer cells [75]. In these examples, specimens were imaged whole, rather than first being sectioned, so intracellular structures were not resolved.

The lack of applications in which intracellular structures have been resolved might be due to the small thermal expansion coefficient of biological systems, which makes imaging challenging [76], particularly for thin sections. The mechanism that generates contrast in images is also rather

complicated, depending on the absorption coefficient, specific heat capacity and thermal expansion coefficient of samples [68]. Furthermore, imaging is complicated by tip-sample contact dynamics affecting the signal [68].

a-SNOM

In aperture-based scanning near-field optical microscopy (a-SNOM), sometimes acronymised as SNOM or NSOM, an apertured fibre is used to collect light in the near-field region of a sample. The near-field is the light that is confined to within a few tens of nanometres of an object's surface and contains high spatial frequency information, formally introduced in section 2.1. The fibre is sharpened by etching to achieve aperture diameters of, typically, 100nm, resulting in spatial resolutions of this size [77]. Thus, the spatial resolution of a-SNOM is typically only marginally better than diffraction-limited techniques.

a-SNOM has been applied to bioimaging a handful of times, for example to image whole oesophageal cancer cells [78, 79], mesothelial cells [80] and human sperm cells [81]. Amongst these investigations, however, there is little evidence of subcellular identification and chemical sensitivity. a-SNOM has also been used to image cervical lymph node tissue sections [82] and resin-embedded lymphocyte and breast cancer cell sections [83], but here again there is very little evidence of ultrastructure identification with chemical contrast.

s-SNOM

s-SNOM is another such IR SPM technique in which light is focused down to a conductive probe in an AFM system, establishing a highly enhanced and localised electric field at the tip of the probe in a nanoscale version of the lightning rod effect [84, 85]. Measuring the backscattered light from the probe allows the sample's optical (and chemical) properties to be inferred in the small region underneath the tip [86]. Tuning the wavelength (here, of IR lasers) allows different chemical moieties to be probed, based on their IR absorption properties. Crucially, the spatial resolution depends on the size of the tip, and not on the wavelength of the light, allowing s-SNOM to surpass the diffraction limit by several orders of magnitude [84, 87].

s-SNOM was pioneered in the mid-1990s and was shown to have a far-superior spatial resolution than its aperture-based counterpart, a-SNOM [88, 89]. It has since been used as an imaging tool in a vast array of fields and applications [90]. Largely, these have been related to solid state phenomena and devices, including plasmonic nanoantennas [91], graphene plasmonics [92, 93], metasurfaces [94-96] and various semiconductor devices [97, 98]. A variety of other applications exist including the development of novel polymers [99, 100] and biomaterials [101, 102], as well as applications in geosciences [103].

There has been increased interest in using s-SNOM to image biological systems, in a large part due to the advent of quantum cascade lasers (QCLs), which offer low-noise, continuous wave output tuneable throughout the IR. The majority of these applications have been isolated systems such as protein complexes [104, 105], oligonucleotides [106], lipid monolayers [107] and bilayers [108], amyloid fibrils [109] and collagen fibrils [110]. There have been some instances of imaging more complex systems such as viruses [111], E. coli cells [112], primary neurons [113] and red blood cells [114]. However, in these cases, the systems were imaged whole, so intracellular structures were not resolved. s-SNOM has also been used to image zebrafish retinal tissue [115], but limited ultrastructural information was obtained in this case.

More recently, s-SNOM has been used to image and identify intracellular structures in single-cell green alga and E. coli cell sections [116], in a way that begins to rival the intracellular imaging capabilities of EM and super-resolution microscopies. This thesis builds on these results by imaging three types of mammalian cells, including two types of human cells, identifying ultrastructure never-before imaged directly optically at the nanoscale, as well as demonstrating s-SNOM as a tool for studying interactions between cells and nanomedicines.

Comparing s-SNOM, TERS, and AFM-IR

It is difficult to directly compare the imaging capabilities of s-SNOM with that of TERS and AFM-IR since each boasts impressive attributes when fine-tuned to a particular sample type that suits it well. However, some general conclusions can be drawn.

i) Chemical sensitivity

In terms of chemical sensitivity, each of the techniques is capable of measuring infrared absorption by probing vibrational modes. However, TERS struggles to do this for complex biological samples [68], which is partly due to the small Raman cross section of biomolecules. AFM-IR is also limited in this regard by the small thermal expansion of biological samples [68]. Being an all-optical technique that directly probes vibrational modes with infrared light, s-SNOM does not suffer from the same limitations in its chemical sensitivity.

ii) Spatial resolution

Exploitation of plasmonic effects associated with scanning tunnelling microscopes has resulted in sub-nanometre spatial resolution TERS, which beats both s-SNOM and AFM-IR [68]. However, this level of spatial resolution has not been realised for complex biological specimens, and tip-to-tip variability makes it unreliable [68].The practical spatial resolution for complex biological samples is closer to that of s-SNOM and AFM-IR, at the level of tens of nanometres. Once again, this is a situation in which the exact details of the sample (topographically and chemically) play an important role.

iii) Image acquisition time

Since the three techniques are all scanning probe techniques, image acquisition time is in principle very similar. The image acquisition time depends much more on the pixel size desired and the signal-to-noise ratio achieved for a given sample, which then informs the choice of pixel integration (dwell) time. The image acquisition times for all images presented in this thesis are given in figure captions. Naturally, these vary hugely depending on the pixel size used.

iv) Cost

s-SNOM and AFM-IR systems both generally use QCLs to produce the best possible images. These are still relatively state-of-the-art light sources, costing upwards of £100,000 for a fully integrated system with QCL chips and external cavity. TERS, on the other hand, makes use of cheaper light sources, typically costing tens of thousands of pounds. Thus, TERS systems can in principle be realised at a lower cost than that of s-SNOM and AFM-IR.

1.2 Scope of this thesis

Chapter 2 of this thesis formally introduces the operational principles of s-SNOM, including key aspects such as AFM operation and the interferometric detection of the backscattered light from the probe. The s-SNOM experimental setup used for measurements in this thesis is discussed together with a discussion on the choices of components and procedures for optical alignment. Details on IR spectroscopy are also discussed, including the absorption signatures of some important chemical moieties.

In chapter 3, a metric for quantifying the quality of images is introduced and used in an attempt to obtain optimum values for key imaging parameters. There is also a discussion on the information that can be obtained from the different optical and mechanical image channels available with s-SNOM.

Chapter 4 begins with a discussion of the advantages that s-SNOM holds over EM and super-resolution microscopies, before demonstrating these with the label-free imaging of multiple myeloma cells. Images of cell sections are presented at several imaging wavelengths, mapping a variety of chemicals and isolating subsets of cell ultrastructure. The images contain many intracellular structures imaged directly optically at the nanoscale for the first time; these include mitochondria, endoplasmic reticulum and nuclear components. Supporting TEM images of the same cell line, stained with uranyl acetate and lead citrate, are shown to help validate identifications made in the s-SNOM images.

In chapter 5, an application of s-SNOM in nanomedicine is demonstrated by using it to image nanoparticle theranostics (nanoparticles with therapeutic, targeting and imaging functionalities) in hippocampal neuron sections. Crucially, it is shown that s-SNOM can be used to map the distribution of these nanoparticle theranostics in multiple interaction modes, whilst simultaneously mapping functional chemistry in the cells. Observations are once again validated with TEM images of the same cell line. It is also shown that osmicating the cells might enable s-SNOM imaging at higher spatial resolution.

Chapter 6 demonstrates the capability to image whole cells (rather than sections of cells) using s-SNOM whilst simultaneously imaging interactions with silica-based nanoparticles. These nanoparticles are non-toxic and can be loaded up with large drug cargos, making them potentially very useful in nanomedicine. Here they are imaged in malignant glioma cells, with emphasis placed on imaging lamellipodia and filopodia, the structures at the peripheries of cells responsible for cell movement, amongst many other functions. It is shown that the embedding status of the nanoparticles can be determined using s-SNOM, which is key in nanomedicine research but can be difficult to achieve with EM and super-resolution microscopy. Additionally, a morphological erosion algorithm is used to correct topography images of cells. This is the first time such an algorithm has been applied to a study using s-SNOM and it is here argued that it is highly important for accurately representing cell topography.

This thesis concludes in chapter 7 with a summary of the conclusions that can be drawn from the results presented and the achievements of this thesis, as well as suggested future work.

Chapter 2

Required Knowledge and Experimental Setup

The first part of this chapter introduces the optical near-field – the surface-confined optical field that is exploited in near-field microscopy. The second part introduces some operational principles of the near-field microscopy technique used for measurements in this thesis, s-SNOM. Included in this are the principles of AFM, the tip-sample optical coupling, and the recovery of sample properties from the backscattered light from the probe. The third part of this chapter provides detail on the experimental setup used specifically for measurements in this thesis, including the choices for the optical components used and the procedures used for achieving optical alignment. The final part of this chapter discusses IR spectroscopy, highlighting absorption features of important chemical moieties, as well as introducing another technique used for measurements in this thesis, Fourier transform infrared (FTIR) spectroscopy.

2.1 The optical near-field

The optical near-field is an electromagnetic field whose strength decays exponentially from the surface of an object. To understand the theoretical origins of the near-field, it is instructive to describe an optical field in its angular spectrum representation. This can be understood as the series expansion of a field in terms of plane and evanescent (spatially confined) waves whose amplitudes and propagation directions vary. One component of such a field, with wavevector $\boldsymbol{k}$ and angular frequency ω, is given by

$$E(r) = E_0 e^{\boldsymbol{k}\cdot\boldsymbol{r}-\omega t}. \tag{2.1}$$

Assuming that the propagation medium is homogeneous, isotropic and linear, all wave components must satisfy the Helmholtz equation:

$$(\nabla^2 + k^2)E(r) = 0 \tag{2.2}$$

where $k = \frac{\omega}{c}n$, n is the refractive index of the medium and c is the speed of light in free space. If the beam propagates in the z-direction, then there are two possible solutions:

$$\begin{aligned} &\text{(i)} && e^{i(k_x x + k_y y)} e^{\pm i|k_z|z}, && k_x^2 + k_y^2 \leq k^2, \\ &\text{(ii)} && e^{i(k_x x + k_y y)} e^{-|k_z||z|}, && k_x^2 + k_y^2 > k^2. \end{aligned} \tag{2.3}$$

where the spatial frequencies in the x, y and z directions are related by $k_z \equiv \sqrt{k^2 - k_x^2 - k_y^2}$ [117].

Solution (i) represents plane waves that propagate in the z direction into the far-field. These waves have transverse spatial frequencies, k_x and k_y, that must be less than the spatial frequency $k \sim \frac{1}{\lambda}$. Thus, there is an upper limit to the spatial information that is carried into the far field that is tied to the wavelength.

Solution (ii) represents evanescent waves whose transverse spatial frequencies exceed k, and thus there is no limit to the spatial frequency information carried by such waves. However, these waves decay exponentially in the z direction and are thus confined to a few nanometres of an object's

surface, forming the optical near-field. Thus, these waves cannot be recovered with conventional imaging techniques.

In s-SNOM, a sharp conductive probe, illuminated by a light source, is brought close to an object's surface such that the electric field distribution around the tip of the probe is modified by the near-field confined to the object's surface. This modification, which contains the high spatial frequency information about the object's surface, is detected in the light that is scattered from the probe into the far-field, from which local sample properties can be recovered. Full details of how this is achieved are provided in the following section.

2.2 s-SNOM operational principles

2.2.1 Atomic force microscopy

In AFM, a sharp probe is raster scanned across a sample to build up an image that maps the sample topography, amongst a variety of other mechanical properties, depending on the intended application [118]. Commonly, a so-called tapping mode is used, whereby the probe oscillates at the end of a cantilever, touching the sample at the bottom of the oscillation. Tapping the sample, rather than maintaining constant contact, has the advantage of reducing the lateral force on the probe. It is also a critical part of recovering the sample properties from the backscattered light, discussed in section 2.2.3.

Figure 2.1 shows the operation of a typical tapping mode AFM system. A sharp probe oscillates at an amplitude A (typically referred to as the tapping amplitude) with frequency Ω. These oscillation parameters are monitored by measuring the deflection of a laser reflected off the top side of the cantilever throughout the oscillation. In s-SNOM, the sample is raster scanned on a piezoelectric stage beneath the probe. The sample is moved, rather than the probe, because the imaging laser must remain focused on the probe throughout image acquisition.

When the probe meets a higher part of the sample, there is less room for the probe to oscillate and the tapping amplitude temporarily decreases. This decrease is measured at the photodiode and a feedback system retracts the stage to restore the original tapping amplitude, A_0. Likewise, if the probe

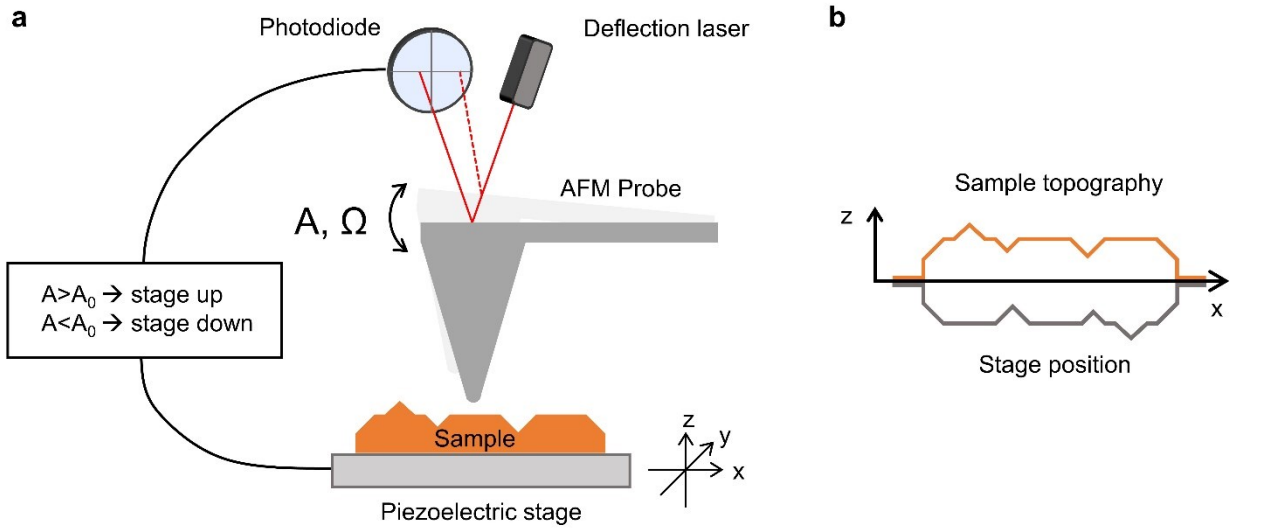

Figure 2.1 Atomic force microscopy (AFM) operation. ***(a)*** *A sharp probe at the end of a cantilever is oscillated with amplitude A and frequency Ω. The oscillation amplitude is monitored by measuring the deflection of a laser resulting from the bending of the cantilever. As the sample is raster scanned below the tip, the oscillation amplitude is maintained at a target tapping amplitude, A_0, by moving the sample in the vertical direction.* ***(b)*** *The stage position throughout the scan (grey line) is used to generate the topographical map of the sample (orange line).*

reaches a lower part of the sample, the tapping amplitude temporarily increases, and the stage moves upwards to restore the tapping amplitude to A_0. The movement of the stage in three dimensions is used to generate a map of the sample topography. Whilst obtaining the sample topography is not the main focus of s-SNOM, it 'comes free' with s-SNOM measurements and is used in parts of this thesis.

2.2.2 Illumination, tip-sample optical coupling and scattering of light from the probe

AFM probes are typically made from monolithic silicon that is wet-chemically etched to leave a sharp tip of nanoscale dimensions. s-SNOM generally uses AFM probes that are coated with a conductive layer. The probes used for measurements in this thesis, and indeed widely in the s-SNOM community, are platinum iridium alloy-coated probes with a stiffness of 42N/m and a typical resonance frequency of 285kHz (Arrow NCPt, available at NanoWorld, Switzerland).

Figure 2.2 shows the illumination of the s-SNOM probe, the optical coupling between the tip and sample and the scattering of light from the probe. The probe is illuminated with light polarised such that a large component is along the long axis of the probe. This establishes an enhanced and highly localised electric field at the tip of the probe [84, 85], which is modified in the presence of a sample such that the tip-sample system is coupled. This coupling is often referred to as the near-field interaction, illustrated by the curved arrows in figure 2.2. Resultantly, a dipole is induced in the tip with an effective polarizability that depends on the tip and sample properties [119].

Several analytical models such as point dipole models [119] and finite dipole models [120] can be employed to estimate the effective polarizability given tip and sample properties. Accounting for higher harmonic detection schemes (section 2.2.3) then allows theoretical estimates of the s-SNOM signal to be generated and compared with experimental data [120]. Whilst analytical models can be applied to layered systems [121-124], they cannot be applied to systems with spatial variation in the scanning directions, meaning they are of little use for complex systems such as cells. Finite element simulations have been applied to homogeneous samples [125, 126], as well as samples with very simple spatial distributions in the scanning directions [127] such as metal-dielectric boundaries in the read/write head of hard disk drives [128, 129], but even with this simple geometry the simulations are very computationally demanding.

The tip scatters light according to the strength of the induced dipole and thus the sample's optical properties are encoded in the backscattered light. In particular, the phase of the backscattered light corresponds to the absorption of the sample in the small region underneath the tip [130]. Once again, the confinement of the tip-sample coupling to the region underneath the probe means that the spatial resolution of s-SNOM depends on the size of the tip of the probe, rather than the wavelength of light. The typical apex radius of a tip is ~25nm, meaning that chemical information can be obtained with a spatial resolution that surpasses diffraction by several decades.

Figure 2.2 shows that, in addition to the direct illumination of the probe, there is an additional component of illumination due to reflection from the sample. This increases the strength of the electric field confined to the tip. The scattered light from the probe is also reflected by the sample, increasing the strength of backscattered light that can be detected. Designing a sample with a highly

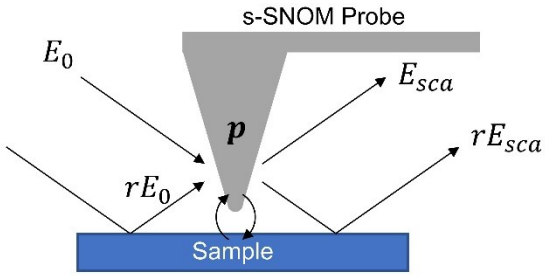

Figure 2.2 Illumination, tip-sample optical coupling and scattering of light from the s-SNOM probe. *The s-SNOM probe is illuminated directly by the incident field E_0 and indirectly by the reflection of the incident field from the sample with magnitude rE_0. The tip-sample system can be described by a dipole, $\boldsymbol{p}$, scattering light with magnitude E_{sca}. Reflection of the scattered light from the sample increases the total scattering by rE_{sca}. Note that the incident and scattered fields are shown on opposite sides of the probe for clarity; the scattered light that is detected, however, travels back along the incident beam.*

reflective substrate can therefore increase the illumination of the probe and the strength of the scattered field that is measured [122]. Using a reflective substrate can additionally boost the s-SNOM signal through its near-field interaction with the tip, but the magnitude of this effect is only significant for thin samples (<30nm), otherwise the substrate is too far from the tip [122].

Tuning the wavelength of illumination allows different chemical moieties in samples to be probed based on their IR absorption signatures. Such wavelengths can be generated with QCLs which produce mid IR wavelengths by exploiting intersubband transitions in semiconductor quantum well heterostructures [131]. The output of a QCL is tuned to a particular wavelength using an external cavity (fully integrated in our system) containing a blazed grating in Littrow configuration, whereby the angle of incidence of the light is matched to the first order diffraction angle [132]. In the imaging setup used for measurements in this thesis, an array of four tuneable, continuous wave QCL chips in one fully integrated benchtop system is used, covering a spectral range of 5–11μm (MIRcat QT-2400, Daylight Solutions, USA).

2.2.3 Recovering optical properties of samples

The majority of the backscattered light from the probe comes from its shaft, not its tip where the sample's optical properties are encoded. This means that there is a large background signal many orders of magnitude greater than the useful signal that contains the sample's optical properties. To

overcome this issue, a higher harmonic detection scheme is employed, whereby the intensity of the backscattered light is analysed at harmonics of the probe oscillation frequency.

The exponential decay of the near-field, discussed in section 2.1, means that when the probe is oscillated above a sample there is a highly non-linear component to the light that is backscattered from the probe that corresponds to the high spatial frequency information carried by the near-field. This non-linearity means that the backscattered light has frequency components at harmonics of the probe oscillation frequency. The light backscattered from the shaft (the background) does not have this strong non-linear component. Thus, analysing the signal at harmonics of the probe oscillation frequency provides a means of isolating the near-field signal from the background.

For a more detailed explanation of this process, it is useful to consider 'approach curves', which show how the s-SNOM signal decays as the minimum tip-sample separation (that is, the distance between the tip and sample at the bottom of the tip oscillation), ζ, is increased. Note that approach curves are generally used as a diagnostic tool and, during imaging, ζ is approximately zero. Figure 2.3 shows approach curves generated by the author using a finite dipole model [120] and accounting for demodulation at harmonics of the probe oscillation frequency. The finite dipole model takes into consideration the dimensions of the probe, modelled as a prolate spheroid, the optical properties of a semi-infinite sample, and the tip-sample separation [120]. In this case, the tip is modelled as a prolate spheroid of polar axis length 300nm and a radius of curvature at the apex of 25nm, and the sample is modelled as a semi-infinite slab of silicon.

To account for the detection scheme used in s-SNOM, the scattered light is computed for a range of tip heights representing the sinusoidal oscillation of the probe. The time-variation of the scattered light is then demodulated at the probe oscillation frequency to obtain the s-SNOM signal and taking the absolute value yields the s-SNOM amplitude at each harmonic, s_n. Figure 2.3 shows that s_n decreases as ζ is increased. This is because, at larger ζ, there is less modulation of the electric field surrounding the probe (and thus of the scattered light) throughout its oscillation. This results in there being smaller frequency components at harmonics of the probe oscillation frequency when the signal is demodulated. It can also be seen that the signal demodulated at higher harmonics of the probe

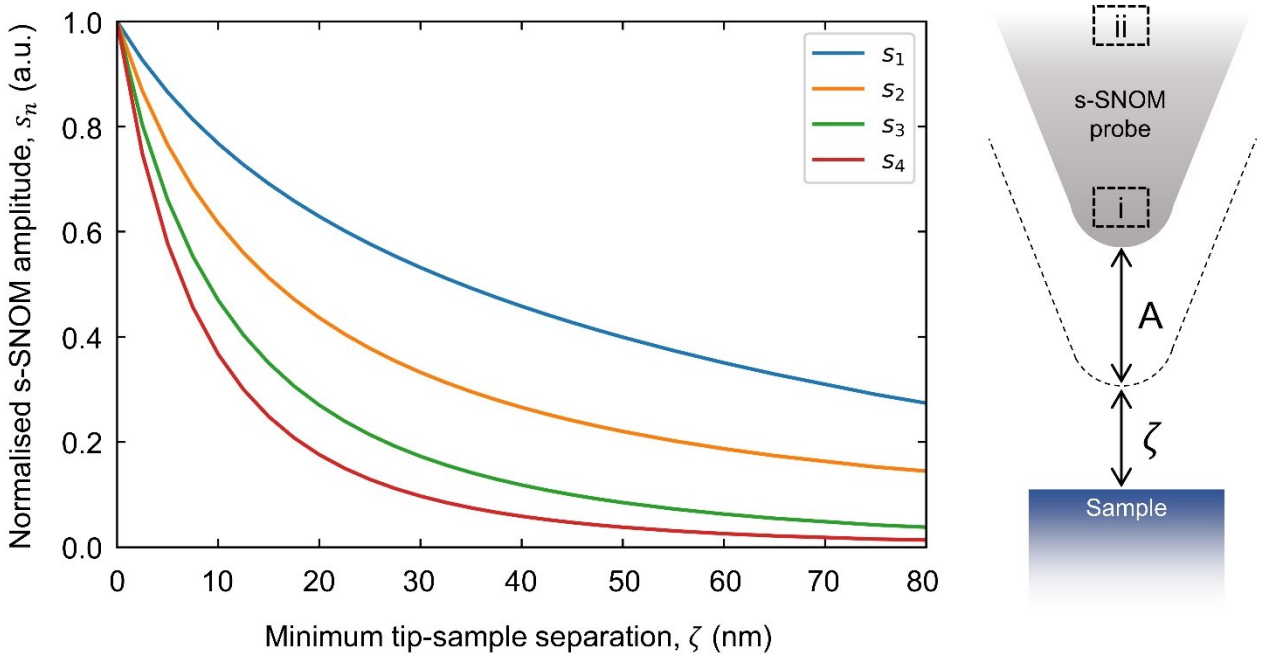

Figure 2.3 Approach curves. *The normalised s-SNOM amplitude, s_n, evaluated using a finite dipole model and accounting for demodulation at harmonics 1–4 of the probe oscillation frequency, is plot against the minimum tip-sample separation, ζ. The tapping amplitude, A, is kept constant. The two regions of the probe, i and ii, represent regions close-to and far away from the tip apex, respectively.*

oscillation frequency decays more quickly. This is because detecting at higher harmonics requires greater modulation of the scattered light.

Now, consider a region of the probe close to its apex (such as region i in figure 2.3) and another region further up the shaft (such as region ii in figure 2.3), both with ζ = 0. The region close to the probe apex is like the low ζ case in figure 2.3 in that it experiences large modulation throughout an oscillation and thus contributes a large s-SNOM signal. The region further up the shaft is like the high ζ case in figure 2.3 in that it experiences little modulation throughout an oscillation and thus contributes a much smaller s-SNOM signal. Therefore, by measuring the component of the signal at harmonics of the probe oscillation frequency, the signal originating from the tip of the probe can somewhat be isolated from the background signal arising from the shaft of the probe.

However, even in this higher harmonic detection scheme, the s-SNOM signal is still contaminated with a multiplicative background signal that arises because detectors measure intensity, or the square of the electric field strength [133]. Fortunately, this problem can be overcome by using an

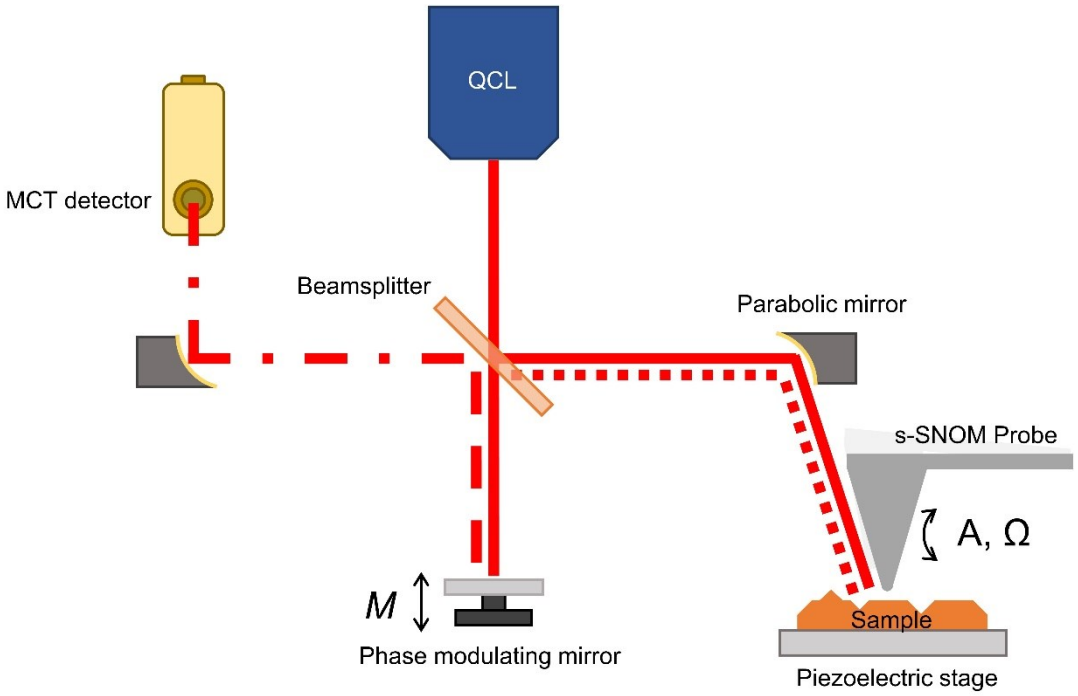

***Figure 2.4 s-SNOM setup showing interferometric detection**. Continuous wave light from a quantum cascade laser (QCL) is split into two arms with a beamsplitter. In one arm, light is focused with a parabolic mirror to a sharp conductive probe which oscillates above a sample with amplitude A. The reference arm is phase modulated with a mirror vibrating at frequency M. Both arms are detected with a mercury cadmium telluride (MCT) detector. Local sample properties are extracted from a large background signal by demodulating the signal at side bands, separated by M, of harmonics n of the probe oscillation frequency, Ω. The sample is raster scanned on a piezoelectric stage to form an image.*

interferometric setup. Very commonly (and in the setup used for measurements in this thesis), a so called pseudoheterodyne detection scheme [133] is employed, shown in figure 2.4. In this detection scheme, light from a QCL is split with a beamsplitter, with one arm focused down using a parabolic mirror to the tip of the probe and the other reflected off a vibrating mirror which adds a phase modulation to the light. The backscattered light from the probe (illustrated with short dashes in figure 2.4) recombines with the reference beam (illustrated with long dashes in figure 2.4) and both are detected with a mercury cadmium telluride (MCT) detector.

The frequency of vibration of the reference mirror, *M*, is approximately 300Hz, which is much less than the probe oscillation frequency of approximately 285kHz. Thus, when the signal is analysed in frequency space, the higher harmonics of the probe oscillation frequency are split into sidebands

separated by *M.* These sidebands are not contaminated with a background signal, so extracting the signal from them retrieves a purely near-field signal [133].

The phase modulation of the reference beam also enables simultaneous retrieval of the amplitude and phase of the backscattered light at each harmonic. This is achieved by combining adjacent sidebands into an nth harmonic complex amplitude, τ_n. With a suitable choice for the amplitude of vibration of the reference mirror (the choice depends on the imaging wavelength), τ_n becomes

$$\tau_n = 2.16k(u_{n,2} + iu_{n,1}) \qquad (2.4)$$

where the coefficient 2.16 arises in the setting of the amplitude of the mirror vibration, k is a complex constant and $u_{n,m}$ is the frequency component of the signal at harmonic n and sideband m [133]. The s-SNOM amplitude, s_n, and the phase, ϕ_n, are then the amplitude and phase of τ_n, respectively. Note that it is not important to determine the value of k when working with relative contrast measurements (that is, comparing to some kind of reference material such as a substrate) [134], as is the case in this thesis.

In the case of weak oscillators, such as the vibrational modes probed here, s_n and ϕ_n relate to the illumination wavelength in a way that resembles the real and imaginary parts of the dielectric function of the sample, respectively [135, 136]. Since the imaginary part of the dielectric function exhibits a peak centred at the resonant frequency of the oscillator(s), mapping ϕ_n at chemically specific wavenumbers provides a means of generating images which display chemical contrast. Since the real part of the dielectric function does not exhibit peaks at resonant frequencies, but rather has a more complicated relationship with the illumination wavelength, it is more complicated to extract chemical information by mapping s_n.

2.3 s-SNOM experimental setup

New s-SNOM and QCL systems were installed and aligned by the author. This section provides details of some of the underlying reasons for the choices of optical components, the steps taken to install and align the systems, and the steps required to setup routine measurements thereafter.

2.3.1 Choices for optical components

Illumination sources suitable for s-SNOM imaging should have a short laser linewidth and should be either continuous wave or pulsed with a repetition rate that far exceeds the mechanical oscillation frequency of the imaging probe [137]. These requirements ensure that the near-field signal can be suitably extracted via an interferometric detection regime. For imaging biological specimens with chemical sensitivity, the illumination source should also have a high signal-to-noise ratio and should be tuneable throughout the infrared. An array of QCLs can provide the spectral range required, and an external cavity can be used to produce the short laser linewidth illumination required. We chose a fully-integrated QCL system (MIRcat QT-2400) from Daylight Solutions, USA. Daylight solutions provide QCL chips that, when assembled in an array of four, cover the entire spectral range we require ~(5–11μm). The chips are also continuous wave and come in a fully integrated benchtop system with an external cavity for ease of tunability, with automatic switching between active chips.

The beamsplitter should be made from a material that provides a high transmission of light across the spectral range used (here, 5–11μm). Both ZnSe and KBr satisfy this condition, with KBr being the typical choice for FTIR spectrometers. However, over time, KBr degrades if not kept completely dry. Since the beamsplitter in the s-SNOM system is exposed, it is better to use a more durable material such as ZnSe, and this is what is used in the s-SNOM system used for measurements in this thesis.

The parabolic mirror used to focus laser light down to the tip of the imaging probe should have a high numerical aperture such that it can accept light from a large solid angle. The parabolic mirror used for the this s-SNOM system has a numerical aperture of 0.46 and focal length of approximately 11mm. This is important both for delivering light to the s-SNOM probe as well as collecting the small amount of light that is backscattered from the probe from which the sample properties are inferred.

The detector used for this imaging setup is a single channel HgCdTe (MCT) photodiode (Model KLD-0.5-J1/11/DC, Kolmar Technologies, USA). It has a spectral range of (2–12μm) and a specific detectivity, D*, of $4x10^{10}$ Jones, which means it can very effectively detect weak signals. The window in front of the photodiode is ZnSe with an antireflection coating, for maximum transmission of the

infrared light. The detector is cooled with liquid nitrogen to prevent thermal noise from saturating the detector. Such detectors are the standard for infrared applications such as infrared spectroscopy, and indeed for s-SNOM.

2.3.2 Initial setup and alignment

In the first step of aligning the system, a flat section of the parabolic mirror immediately before the imaging probe is used such that the beam reflects back along itself and the interferometer can be aligned (that is, the probe is ignored for now). An iris located between the QCL and the beamsplitter is used to check that the beams reflected from both mirrors (the flat part of the parabolic mirror and the reference mirror) are well overlapped with the incident beam. Since the IR laser light is invisible to the eye, its path is ‘painted’ (overlapped) with another visible laser. We are fortunate that our QCL system has an aiming beam (a diode laser) that fulfils this purpose. The parabolic mirror immediately before the MCT detector is also adjusted such that the signal reaching the detector is maximised.

With the interferometer now aligned, the parabolic mirror next to the tip is translated so that the beam is now reflected from the parabolic surface and onto the tip of the probe, which is in contact with a sample. The reference arm of the interferometer is temporarily blocked. The probe is translated such that the signal measured by the detector is maximised. The probe arm is now temporarily blocked and the reference arm is unblocked and the flat mirror between the beamsplitter and the reference mirror is adjusted to maximise the reference arm signal measured at the detector.

With both arms unblocked (and now aligned) and the probe oscillating, the reference arm is again adjusted to maximise the interference between the arms, measured at the detector. When maximised, the vibration of the reference mirror is then activated, and the near field signal is then recovered with pseudoheterodyne detection as described in section 2.2.3. The probe position is then translated at a fine step size to maximise the near field signal recovered.

Mechanical vibrations arising from building vibrations, equipment operation and even conversations between lab occupants can generate noise in the optical s-SNOM images through their coupling to the mechanical oscillation of the probe. To reduce the impact thereof, the setup is situated on an optical table supported by vibration isolator legs (S-2000 Series, Newport, USA). The setup is also

enclosed in a casing lined with acoustic damping foam to absorb vibrations. Having the setup enclosed in this way also helps to stabilise the temperature of the setup. This reduces sample drift due to thermal expansion which is otherwise noticeable with long scan times over small sample areas (e.g., a 1-hour scan of a 10μm x 10μm region).

The chiller used to pump chilled water to the QCL unit (TCube edge, Solid State Cooling Sytems, USA) also has the potential to introduce vibrations into the setup. These can manifest acoustically, from the operation of the centrifugal pump and of the fan used to cool the thermoelectric chips, and can also manifest due to variations in the flow rate of the water. The former is damped by the acoustic damping casing enclosing the s-SNOM setup (the chiller is outside of this casing). The latter is damped, in our setup, by running the flexible water hose through containers of sand, which helps to dissipate some of the vibration.

2.3.3 Setup for routine measurements and maximising the signal-to-noise ratio

With careful operation of a s-SNOM system, and dry, flat, samples, imaging probes can be used for hundreds of hours, if not more. However, a new scanning probe is required whenever a probe is broken, blunted, or contaminated during imaging. Such events are marked by a reduction in the near-field signal recovered or a loss of spatial resolution in s-SNOM and AFM images. When a new probe is installed, a picture of the position of the previous probe, viewed from the top-down microscope built into the s-SNOM system, is used to ensure that the new probe is close to the position of the old one. This means that only very minor translations of the parabolic mirror position are required to regain optimal optical alignment. The resonant frequency of each probe varies slightly and must be determined whenever a new probe is installed. This is measured with the deflection laser and photodiode shown in figure 2.1.

With the probe oscillating at its resonant frequency, it should then be brought into contact with a sample to check that a near-field signal is being recovered. This is marked by the exhibition of an approach curve, shown in figure 2.3. Put simply, measurements of s_n and ϕ_n should be close to zero

when the probe is not in contact with the sample, and then rapidly increase as the probe is brought into contact with the sample, for the reasons discussed in section 2.2.3.

As part of the process to maximise the signal-to-noise ratio of the s-SNOM signal, the signal measured by the detector should then be inspected in the frequency domain. Inspection of the signal in the frequency domain reveals noise peaks that arise from, for example, electrical noise from power adapters that are coupled into the laser output. The oscillation frequency, Ω, should be fine-tuned such that its harmonics, nΩ, do not coincide with such noise peaks. This results in a near-field signal with a higher signal-to-noise ratio.

When a new sample is loaded into the system, it is brought into contact with the tip using an automated routine which iteratively moves the piezoelectric element of the sample stage through its ~3μm range, then brings the stage closer to the tip with a coarser movement linear actuator. This process repeats until the sample makes contact with the probe while the piezoelectric element is engaged. The tapping amplitude of the probe should be set to approximately 50nm in most cases. This can be adjusted to increase the signal, reduce the contamination due to a background signal, or to increase the spatial localisation of the recovered signal; an explanation of this is given in section 3.2.2.

The attenuation of the laser beam, adjusted using a metal grid attenuator (Lasnix, Germany), should be set to avoid saturating the MCT detector and causing sample damage. This is especially important when changing the imaging wavelength, as the laser power varies with wavelength. Generally, the minimum required attenuation should be used to maximise the signal measured at the detector.

For samples which generate a small s-SNOM signal, e.g. biological samples, the pixel integration time can be increased to improve the signal-to-noise of measurements. However, this slower scanning speed can make noticeable the effects of sample drift due to thermal fluctuations. For most measurements shown in this thesis, the minimum integration time of 3ms was used.

Typically, this integration time is combined with a pixel size of 15nm, meaning that a 15μm x 15μm cell can be imaged in approximately 1 hour and 40 minutes (since the system records images in both the forwards and the backwards directions. Images can also be acquired much more quickly by

performing a serpent scan, whereby only one in every five rows are scanned, for example, to dramatically increase image acquisition time (here, ten-fold, as the forward and backward direction scans are combined to produce one image). Interpolation is then used to fill in the pixels in the rows that are skipped.

High resolution imaging is achieved by reducing the pixel size. The pixel size can be reduced to 0.2nm in closed-loop operation, whereby the limit is set by the piezoelectric sample stage (Physik Instrumente, UK) which uses capacitive sensors to monitor its position. However, setting the pixel size below 2nm reduces the scan speed such that sample drift due to thermal fluctuations generally becomes noticeable. This results in sample features no longer being accurately measured in the scanning directions. Thus, for high resolution images, a step size of 2nm was typically used.

The combination of ~3ms pixel integration time and 15nm pixel size yields a scan speed of approximately 5μm/s. For flat samples such as resin embedded cells, this is a suitable speed that avoids damage to the tip from shearing forces. For samples that have larger topographical variations, such as whole cells, it is important to lower the scanning speed to reduce the chance of damaging the tip. This can be achieved by decreasing the pixel size or increasing the pixel integration time.

2.4 Infrared spectroscopy

Whereas visible light drives electronic transitions in molecules, mid-IR light (here, defined as being inclusive of wavelengths in the 3–11μm range) drives vibrational modes. The excitation of these modes is the basis for the chemical identification of samples, as well as generating chemical contrast in IR imaging techniques including s-SNOM. Figure 2.5 shows some examples of vibrational modes that can be excited in molecules. Figure 2.5 (a) shows the stretching mode of a C=O bond in formaldehyde. C=O bonds are also found elsewhere, including in amide functional groups in proteins and nucleobases. Figure 2.5 (b) shows symmetric and asymmetric stretching modes that can be excited when there are active bonds between more than two atoms, here in a water molecule. Note that symmetric stretching in polar molecules such as water results in a change in dipole moment,

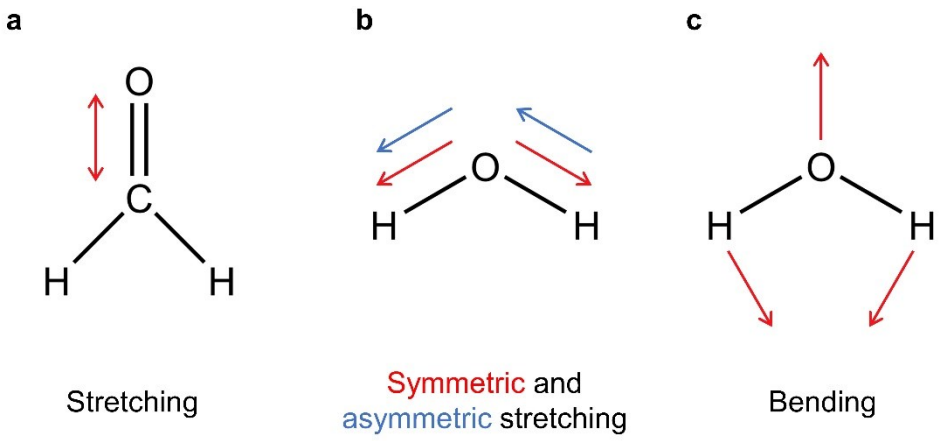

Figure 2.5 Vibrational modes in molecules. ***(a)*** *C=O stretching in formaldehyde.* ***(b)*** *Symmetric and asymmetric stretching in a water molecule.* ***(c)*** *Bending in a water molecule.*

and thus IR absorption, whilst symmetric stretching in non-polar molecules such as carbon dioxide does not. Water molecules also exhibit a bending mode, shown in figure 2.5 (c).

Vibrational modes have associated resonance frequencies where the modes are strongly driven and, accordingly, light is strongly absorbed. The spectral location and width of the resonance is determined by the strength of the bond and the atoms involved, as well as the constitution and structure of the rest of the molecule. For example, C=O bonds in aldehydes, such as the formaldehyde molecule shown in figure 2.5 (a), have resonance frequencies in the 1720–1740cm^{-1} range, whilst C=O bonds in amide groups exhibit resonance in the 1640–1690cm^{-1} range [138].

2.4.1 Absorption features of important chemical moieties

The aggregation of the absorption exhibited by all the vibrational modes in a specimen can be shown as an absorption spectrum. This shows how the absorption, calculated as the natural logarithm of the transmission of light through a sample, depends on wavelength. Figure 2.6 is an absorption spectrum of multiple myeloma cells prepared with a formalin-fixed paraffin-embedded (FFPE) protocol and deparaffinised, whereby the cells are chemically fixed with formalin, embedded in paraffin, sliced into sections (in this case ~1μm thick), deparaffinised, and dried with ethanol. Thus, the absorption spectrum is representative of the fixed biological material without being affected by the paraffin embedding medium.

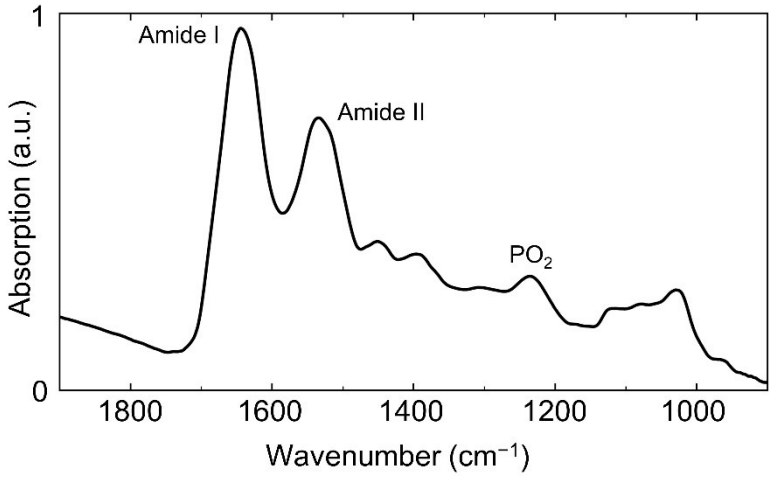

Figure 2.6 Absorption spectrum of multiple myeloma cells. *A normalised absorption spectrum of multiple myeloma cells prepared with a formalin-fixed paraffin embedded process and deparaffinised. The spectrum was measured with a Fourier transform infrared spectrometer.*

The absorption peaks labelled in figure 2.6 are typical of all cells and tissues in terms of their spectral location and amplitude. The amide I absorption peak is an aggregation of vibrational modes exhibited by amide moieties. It is dominated by C=O stretching, but also has contributions from C–N stretching and N–H bending [138]. The amide II absorption peak is constituted of N–H bending and C–N stretching in amide moieties [138]. Both peaks provide a means of probing the amide content of specimens. The phosphodiester (PO_2) absorption peak is primarily constituted of vibrational modes of PO_2-containing moieties that form the backbone of nucleic acids and are also found in lipids and carbohydrates. The remaining features in the absorption spectrum are the aggregate of the 'chemical fingerprints' of the many molecules that constitute the sample. In this, there is a large contribution from C–O bonds in nucleic acids, lipids and carbohydrates, as well as various other vibrational modes of PO_2-containing moieties [139].

2.4.2 Fourier transform infrared spectroscopy

FTIR spectroscopy is the primary way of obtaining infrared absorption spectra such as the spectrum shown in figure 2.6, and is used multiple times throughout this thesis. A diagram of the measurement setup of an FTIR spectrometer is shown in figure 2.7. The setup is arranged in a Michelson interferometer configuration, with light from a broadband IR source (commonly a heated silicon carbide rod) split with a beamsplitter. One arm is reflected off a fixed mirror, M_1, and the other is

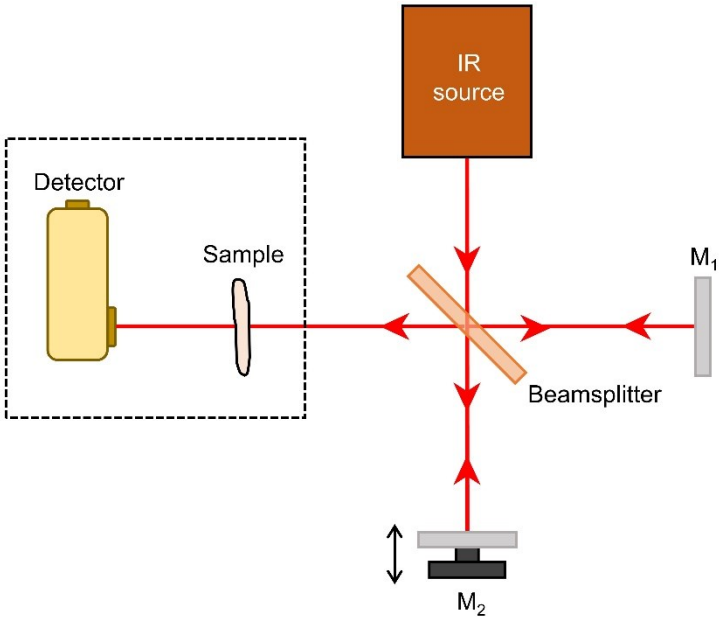

Figure 2.7 Fourier transform infrared spectrometer setup. *A broadband infrared (IR) light source is split with a beamsplitter, with one arm reflected off a fixed mirror (M_1) and the other from a movable mirror (M_2). The beams are recombined and measured at the detector after passing through the sample. Moving M_2 introduces a phase difference between the two beams, modifying the interference measured at the detector. Analysing the intensity of the light as a function of the mirror position allows the spectral dependence of the measured intensity to be retrieved. The region in the dashed box is often integrated in a microscope with reflective optical elements.*

reflected off a movable mirror, M_2, which allows the path length to be changed. In transmission mode FTIR (shown in figure 2.7), the beam is transmitted through the sample before being measured. In reflection mode (not shown), the reflection off the sample is instead measured. Usually, an MCT detector is used to measure the beam intensity, and is often integrated into a microscope, together with the sample, to enable FTIR spectroscopy of microscopic regions.

Full details of how absorption spectra are computed from FTIR measurements can be found in Griffiths et al. [140]. Briefly, when M_2 is moved such that the path lengths of each arm are no longer equal, the two arms interfere with each other. The nature of the interference (constructive or destructive) depends on difference in path length and, crucially, the wavelength of the light. This means there is a mix of constructive and destructive interference of the light from the broadband source for any position of M_2 except for when arms have equal path length. The intensity of light is recorded whilst M_2 is moved, generating a so-called interferogram. Computing the inverse Fourier

transform of the interferogram yields the intensity transmitted through the sample as a function of wavelength, from which the absorption spectrum can be calculated.

Often, s-SNOM systems have an additional detection module for generating FTIR-like spectra for nanoscale regions local to the imaging probe. The so-called nano-FTIR modules use a broadband IR source in an asymmetric Michelson interferometer, where the sample is located in one of the arms of the interferometer. A reference mirror is moved to generate an interferogram as in far-field FTIR. Since the sample is in one of the interferometer arms, nano-FTIR retrieves amplitude and phase spectra, as opposed to far-field FTIR which retrieves just the amplitude [130, 136, 141]. Nano-FTIR measurements are often used to complement s-SNOM images, showing the spectral dependence of the amplitude and phase signals for locations within images. The s-SNOM system used for measurements in this thesis does not have a nano-FTIR module. Instead, far-field FTIR measurements are used to inform the choice of imaging wavelength, and focus is put on the imaging capabilities of s-SNOM, rather than the nanoscale spectroscopy that is enabled with nano-FTIR.

Chapter 3

Optimising measurement parameters

Many measurement parameters require optimising to produce s-SNOM images with a high signal-to-noise ratio (SNR). This is especially important when imaging biological samples which generally generate a small s-SNOM signal. Amongst these measurement parameters are those related to the pseudoheterodyne detection scheme, such as the frequency and amplitude of the vibration of the reference mirror, and those related to the oscillation of the probe, such as its tapping amplitude and frequency.

For many of these parameters, it is clear how they should be optimised. For example, the amplitude of the reference mirror is set such that there is complete decoupling between the phase and amplitude signals recovered with pseudoheterodyne detection. In the case of the tapping frequency of the probe, it is set such that it, and its harmonics, do not overlap with noise peaks from electronic equipment, which can be achieved by inspecting the s-SNOM signal in frequency space.

For some of these parameters, however, it is less clear how they should be optimised. For example, the imaging wavelength should be set close to the peak of the absorption feature being measured

(which is generally very well documented [139] and measurable with an FTIR spectrometer) but atmospheric absorption (mainly from water vapour) and instabilities in the laser output introduce noise. This means fine tuning of the imaging wavelength is required. In another example, increasing the tapping amplitude generally yields a better SNR, but, for reasons explained in this chapter, it also reduces the contrast observed between cell regions and can even introduce a background signal.

This chapter introduces a metric, the contrast-to-noise ratio (CNR), and uses it in an attempt to find the optimum imaging wavelength in the amide I absorption band and the optimum tapping amplitude. The CNR is commonly used in other areas of imaging but has not been applied to s-SNOM images before. There is also a wider discussion on how the tapping amplitude affects the probing depth into the sample, the field confinement, and the noise observed in s-SNOM images. Following this, the information that can be obtained from each of the phase, amplitude and topographical channels is discussed using example images of cells. Finally, images of a cell using each measurement harmonic are shown to justify the choice of imaging harmonic used in the rest of this thesis.

3.1 Contrast-to-noise ratio: a metric for image quality

Setting aside the physical meaning (that is, the chemical information that can be inferred) and the spatial resolution of images, there are two main aspects of an image that can be used to quantify its quality. The first is the contrast, which is the difference in signal between two regions of interest. The second is the noise level, or graininess of the image. Often, as is the case in s-SNOM, these two quantities can be traded-off with one another when parameters are changed. It is helpful, therefore, to combine them by defining a contrast-to-noise ratio, CNR, given by

$$\mathrm{CNR} = \frac{\text{contrast}}{\text{noise}} = \frac{\mu_1 - \mu_2}{\sigma} \tag{3.1}$$

where μ_1 and μ_1 are the averages of pixel values in regions 1 and 2, respectively, and σ is the standard deviation of pixel values in a region without features (here, that is the embedding resin in the extracellular region).

Figure 3.1 shows an example of how an s-SNOM image of a cell can be split into regions so that quantities can be extracted to calculate CNR values. Figure 3.1 (a) is an s-SNOM image of a multiple

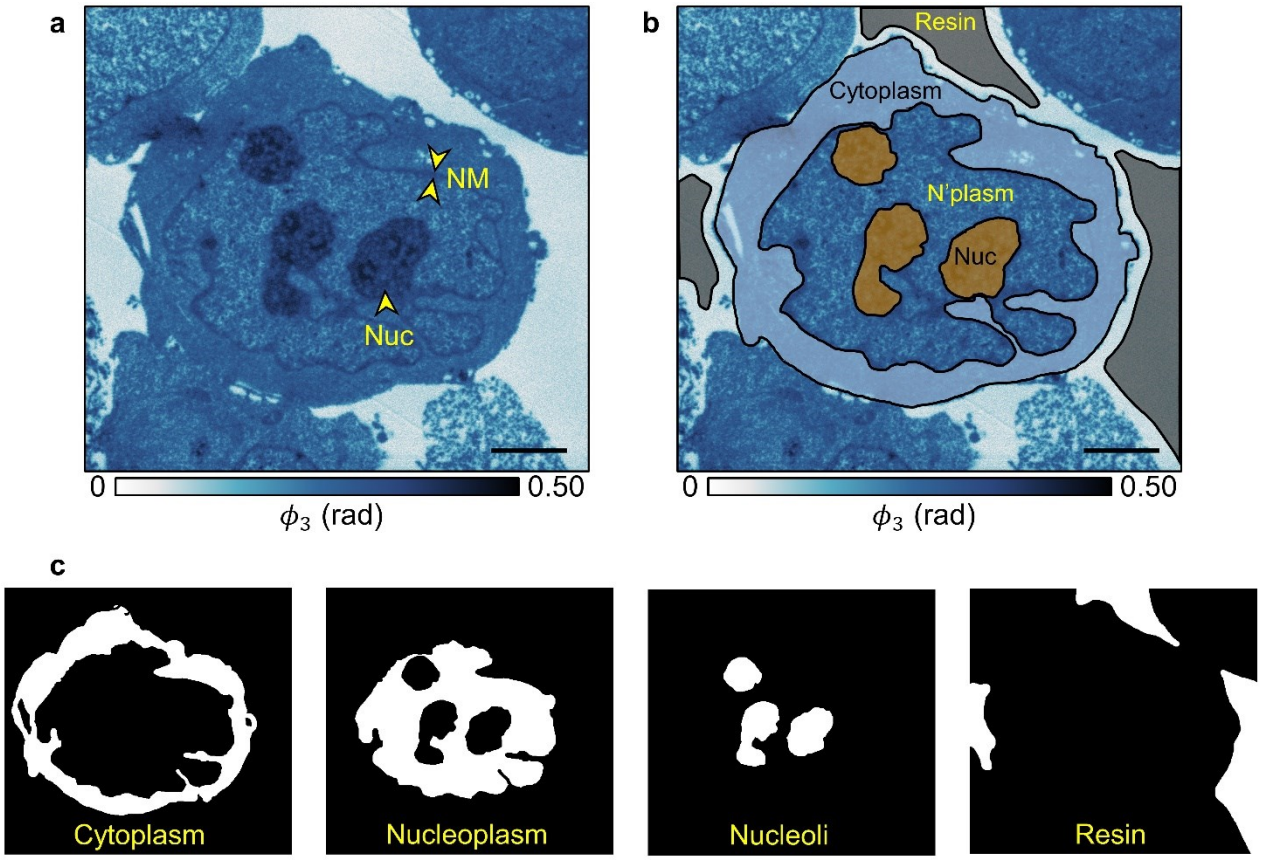

Figure 3.1 Masking regions of interest in cells to extract parameters for contrast-to-noise ratio calculations. (a) *s-SNOM image of a multiple myeloma cell section acquired at an imaging wavelength of 1667cm^{-1}. The image dimensions are 13μm x 12μm with 15nm pixel size. A pixel integration time of 3ms was used and thus the whole image took 1 hour and 10 minutes to acquire. The tapping amplitude was ~59nm.* ***(b)*** *Regions of interest in the cell.* ***(c)*** *Masks, constructed using Gwyddion, that enable quantities to be extracted from s-SNOM images for each cell region. NM; nuclear membrane, Nuc; nucleolus, N'plasm; nucleoplasm. Scale bars 2μm.*

myeloma cell embedded in epoxy resin acquired at an imaging wavelength of 1667cm^{-1} to excite amide moieties. Figure 3.1 (b) labels different regions of interest in the image, namely the cytoplasm, the nucleoplasm, nucleoli (Nuc) and the extracellular space (embedding resin). Full details about the preparation of these samples and the biochemical relevance of each region are left for chapter 4. Figure 3.1 (c) shows the masks used to extract quantities from these regions of interest. Mean pixel values are extracted from images using each of these masks so that the contrast between two regions (for example, the cytoplasm and the embedding resin) can be computed. The standard deviation is extracted from pixel values in the embedding resin as a measure of the image noise.

Masks are constructed using Gwyddion with a combination of automatic construction using threshold signal levels and manual drawing. Thus, there is some human subjectivity associated with

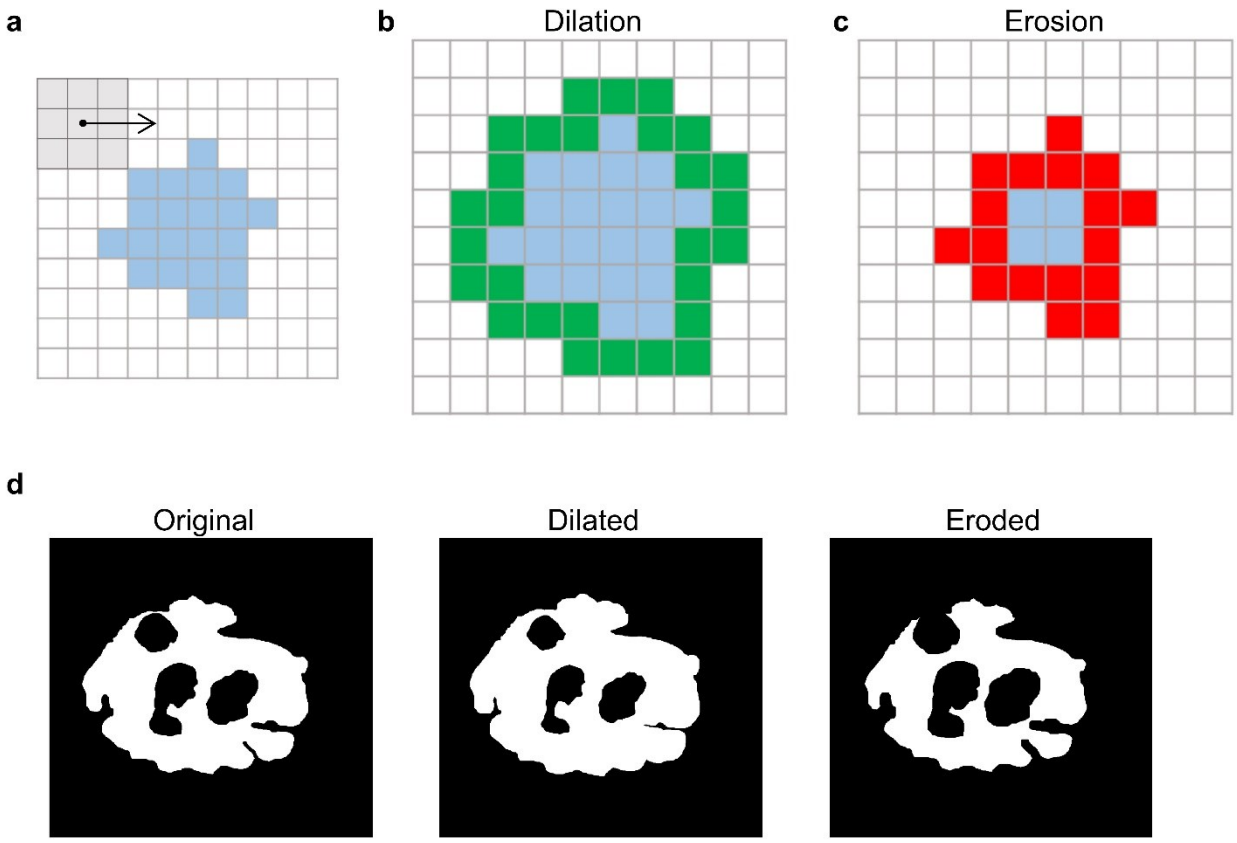

Figure 3.2 Dilation and erosion of masks. ***(a)*** *A shape (blue squares) is operated on by a 3x3 box-shaped structuring element (grey squares) which is raster scanned across all pixels. New dilated and eroded images are generated from the sets of structural element central pixels that satisfy dilation and erosion conditions, respectively.* ***(b)*** *For dilation, at least one pixel in the structuring element must overlap with the original shape. The green squares indicate the pixels that are added in one iteration of dilation.* ***(c)*** *For erosion, all pixels in the structuring element must overlap with the original shape. The red squares indicate the pixels that are removed in one iteration of dilation.* ***(d)*** *The original, dilated and eroded nucleoplasm masks. Five iterations of each algorithm were applied using a 3x3 box-shaped structuring element.*

constructing masks which leads to uncertainty in the CNR value. To account for this, morphological dilation and erosion algorithms are applied to masks to create larger and smaller versions, respectively. Figure 3.2 (a,b,c) illustrates how such algorithms are applied. A structuring element, here a 3x3 box, is raster scanned across all pixels in an image. New dilated and eroded images are generated using the sets of structural element central pixels that satisfy dilation and erosion conditions, respectively. The dilation condition is that at least one pixel in the structuring element overlaps with the original shape. The erosion condition is that all pixels in the structuring element must overlap with the shape. Applying each algorithm to the original masks created in Gwyddion result in a set of three masks for each cell region that accounts for human subjectivity. Figure 3.2 (d)

shows the three masks for the nucleoplasm cell region. For the images presented in this chapter, five iterations of the dilation and erosion algorithms are applied to masks, dilating/eroding pixels of 15nm pixel size. The parameters in equation (3.1) are calculated using each of the three masks, from which a mean and standard deviation are obtained for each parameter. The CNR is calculated using the mean values of each parameter and an error is assigned by propagating the standard deviations of parameters according to equation (3.1).

3.2 Determining optimum measurement parameters using the contrast-to-noise ratio

3.2.1 Imaging wavelength

Figure 3.3 shows how the contrast, noise and contrast-to-noise ratio vary with imaging wavelength when calculated from images of the cell shown in figure 3.3 (a). Two series are shown in the plots of contrast and contrast-to-noise ratio; these are the respective values when the cytoplasm is compared to the embedding resin, and the nucleoli are compared to the nucleoplasm. Two sets of each metric were obtained so that further investigation could be performed if the results indicated that the optimum imaging wavelength depends on the cell regions compared.

Figure 3.3 (b) shows that there is maximum contrast between the cytoplasmic and resin regions at an imaging wavelength of approximately 1660cm^{-1}. This is a slightly higher wavenumber than the peak position recorded with far-field FTIR, a phenomenon that has been previously observed in polymethyl methacrylate (PMMA) film [136]. The maximum contrast between nucleolus and nucleoplasm is at a slightly higher wavenumber, which might be due to a slightly different chemical constitution, for example an increased density of nucleobases.

Figure 3.3 (c) shows how the noise level of images depends on imaging wavelength. Variations in the noise level are suspected to be due to instabilities in the laser output, as well as atmospheric absorption exhibited by water vapour, which has many absorption lines in this region [142].

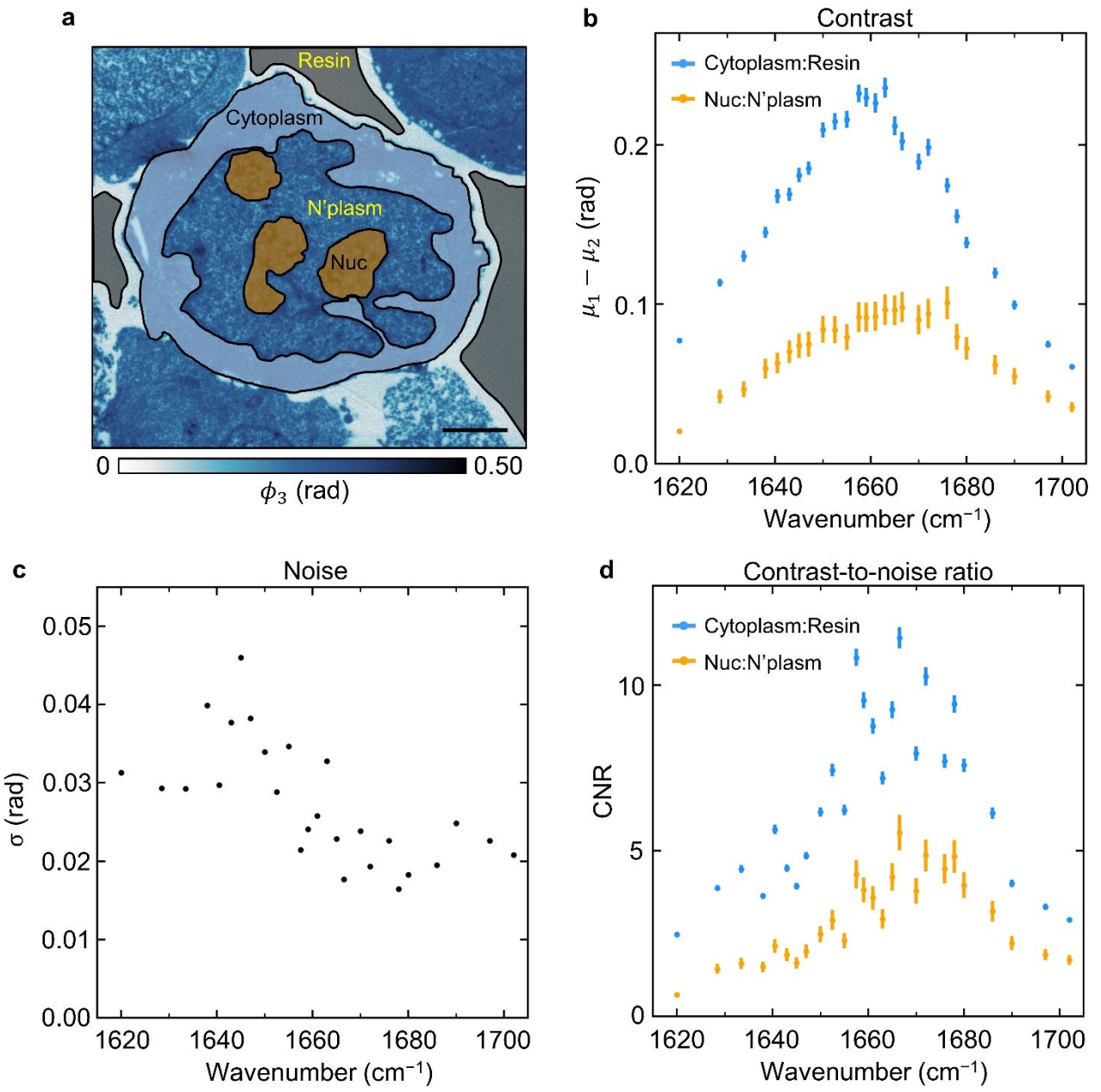

Figure 3.3 Optimum imaging wavelength in the amide I absorption band. (a) *s-SNOM image of a multiple myeloma cell acquired at 1667cm^{-1}. The extracellular embedding resin, the cytoplasm, the nucleoplasm (N'plasm), and the nucleolus (Nuc) are identified as distinct regions of interest.* ***(b)*** *Contrast (difference in mean pixel values) between the cytoplasm and the resin (blue) and the nucleolus and the nucleoplasm (orange) calculated for images acquired at a range of wavelengths.* ***(c)*** *Image noise (standard deviation of pixel values in the extracellular resin region) calculated at each wavelength.* ***(d)*** *Contrast-to-noise ratio (CNR) calculated at each wavelength. Error bars are calculated by obtaining the mean and standard deviation of parameters in equation (3.1) using three mask sizes and propagating these into an error in the CNR. Scale bar 2μm.*

The CNR plot in figure 3.3 (d) shows that, when image noise is considered, the optimum wavenumber for imaging shifts higher. The maximum CNR value is observed for a wavenumber of 1667cm^{-1}. This is the case for the CNR measured between the cytoplasm and the resin, as well as

that between the nucleolus and the nucleoplasm, suggesting that the optimum imaging wavelength is independent of the cell regions being compared.

3.2.2 Tapping amplitude

Figure 3.4 shows how the contrast, noise and contrast-to-noise ratio vary with tapping amplitude when calculated using images of the cell shown in figure 3.4 (a). Once again, two series are shown, for comparisons between the cytoplasm and the resin, as well as the nucleoli and nucleoplasm.

Figure 3.4 (b) shows that the image contrast decreases as tapping amplitude is increased. This can be explained by considering the portion of the tip that contributes to the signal recovered with pseudoheterodyne detection; with higher tapping amplitude, the electric field surrounding parts of the tip higher up the shaft is sufficiently modulated such that the backscattered light from these parts contributes to the recovered signal. Put simply, at higher tapping amplitude, parts of the tip higher up the shaft become important. Parts of the tip higher up the shaft are also less sensitive to changes in cell regions than parts close to the apex, so their contribution acts to reduce the difference in signal between cell regions, thus reducing the contrast.

Figure 3.4 (c) shows that the noise level of images decreases as tapping amplitude is increased. This is because, as explained above, more of the tip contributes to the signal at higher tapping amplitude, so the recovered signal is greater. This means that the phase can be measured with less noise.

Increasing the tapping amplitude beyond approximately 80nm seems to have no impact on the contrast or the noise. This is probably because the tip-sample interaction is confined to close to the sample surface, so an increase in the tapping amplitude is no longer accompanied by a significant increase the modulation of the electric field surrounding the tip.

Figure 3.4 (d) shows how the CNR depends on the tapping amplitude. The dip in the CNR at 67nm and 73nm seems to be due to the increased noise exhibited at these measurements. This might be due to fluctuations in measurement conditions such as temperature and humidity. The results show that the CNR is maximised at a tapping amplitude of approximately 90nm, suggesting that this is the

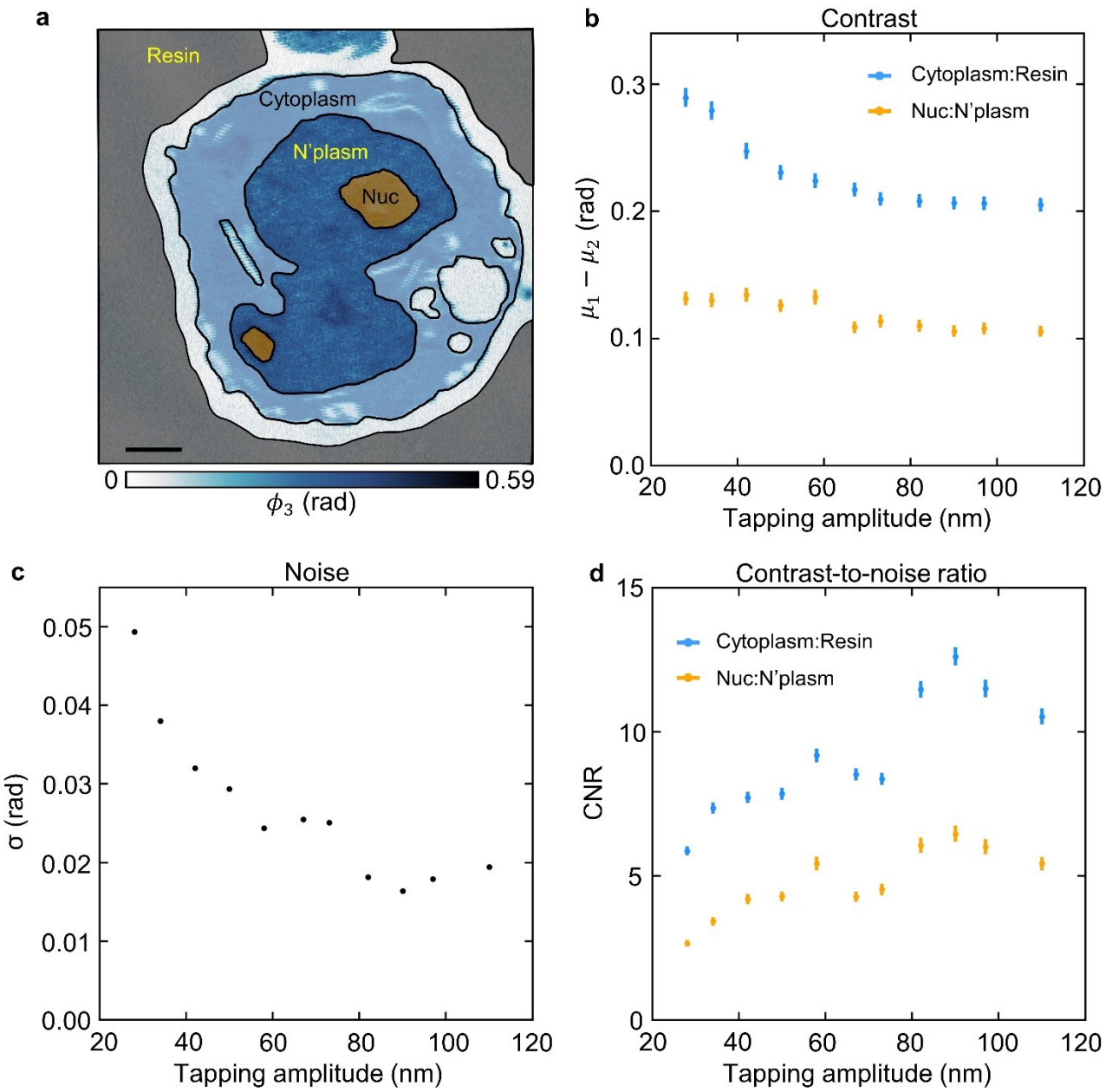

Figure 3.4 Optimum tapping amplitude. (a) *s-SNOM image of a multiple myeloma cell acquired at 1667cm^{-1}. The image dimensions are 15µm x 15µm with 10nm pixel size. A pixel integration time of 3ms was used and a serpent scanning mode was used in which five of every 6 rows were skipped. Thus the whole image took approximately 19 minutes to acquire. The tapping amplitude for the image shown was ~67nm. The extracellular embedding resin, the cytoplasm, the nucleoplasm (N'plasm), and the nucleolus (Nuc) are identified as distinct regions of interest.* ***(b)*** *Contrast (difference in mean pixel values) between the cytoplasm and the resin (blue) and the nucleolus and the nucleoplasm (orange) calculated for a range of tapping amplitudes.* ***(c)*** *Image noise (standard deviation of pixel values in the extracellular resin region) calculated at each tapping amplitude.* ***(d)*** *CNR (contrast divided by noise) calculated at each tapping amplitude. Error bars are calculated by obtaining the mean and standard deviation of parameters in equation (3.1) using three mask sizes and propagating these into an error in the CNR. Scale bar 2µm.*

optimum tapping amplitude. However, at this tapping amplitude, there is a noticeable background

signal that manifests as the pattern shown in figure 3.6 (a). The separation between stripes in the pattern scales with the illumination wavelength, and the pattern is observed strongly in the zero-order harmonic signal. This suggests that the background signal is related to the illumination of the probe. The mechanism for the background signal leaking into images might be that, at high tapping amplitudes, the probe experiences a varying spatial distribution of the illumination profile such that the electric field surrounding the tip is sufficiently modulated to contribute to the signal at higher harmonics. The CNR doesn't encapsulate the negative impact that this background signal has on images, perhaps due to the large regions used for computing it. It does, however, suggest that the tapping amplitude should be increased until the background pattern becomes unacceptably prominent. This was how the tapping amplitude was chosen for the images presented in this thesis, typically resulting in tapping amplitudes between 30nm and 70nm, balancing image contrast, noise and the background signal.

The choice of tapping amplitude also has implications for the field confinement and the probing depth into the sample. There is increased field confinement with smaller tapping amplitudes, leading to better spatial resolution in images [143]. This is a result of the shorter decay length of approach curves at smaller tapping amplitudes [144]. The probing depth into the sample has also been shown to increase when the tapping amplitude increases, in agreement with simulations performed using a finite dipole model [145]. This can be understood in terms of such models by considering the increased depth of mirror charges in the sample when the tip-sample distance increases, as in higher tapping amplitudes.

3.2.3 The role of tip geometry in the s-SNOM signal

The previous section on the optimum tapping amplitude is specific to the PtIr alloy probes (Arrow NCPt, Nanoworld, Switzerland); probes made from different materials and with different tip geometries are likely to have a different associated optimum tapping amplitude. It has been shown, for example, that probes with a smaller tip radius exhibit greater field confinement, demonstrated through the decay lengths of approach curves [87], and this can lead to increased spatial resolution [128].

However, this increase in spatial resolution by using smaller tip radii can come at the expense of increased noise in the signal, attributed to a reduction in the sample volume involved in the near-field interaction with the tip [128]. A different study showed that when the tip radius is increased, noise can be introduced through less stable AFM operation and increased surface roughness, which leads to image artifacts [129]. Thus, the noise in the s-SNOM signal has a complicated dependence on the tip radius.

Since the probing depth is also related to the degree of field confinement at the tip, shown by comparing different demodulation orders [143], it might be expected that the increased field confinement achieved with smaller tip radii are associated with a shallower probing depth.

3.3 Choosing image channels and measurement harmonics

3.3.1 Phase, amplitude and topography

Figure 3.5 shows examples of the optical and topographical images obtained with s-SNOM. Figure 3.5 (a) & (b) are mappings of the phase and amplitude of the backscattered light, respectively, demodulated at the third harmonic of the probe oscillation frequency. Mapping the phase at chemically specific wavenumbers generates images with chemical contrast in a way that depends on the local IR absorption properties of the sample [130]. As explained in section 2.2.3, it is much harder to extract chemical information from amplitude images since its dependence on wavelength is more complicated than the phase-wavelength dependence. Thus, phase images are used in this thesis for chemical mapping.

The amplitude of the backscattered light is also more sensitive than the phase to changes in topography. As such, the knife mark running from the bottom middle of the image to the top-right, as well as the ruffling of sections running diagonally from upper-left to lower-right, appear as artefacts in the topography image (figure 3.5 (c)) and the amplitude image (figure 3.5 (b)), but less so in the phase image (figure 3.5 (a)).

Some intracellular structures such as the nuclear membrane, nuclear region and nucleoli can be identified based on the morphology observed in the topography image in figure 3.5 (c). This is due

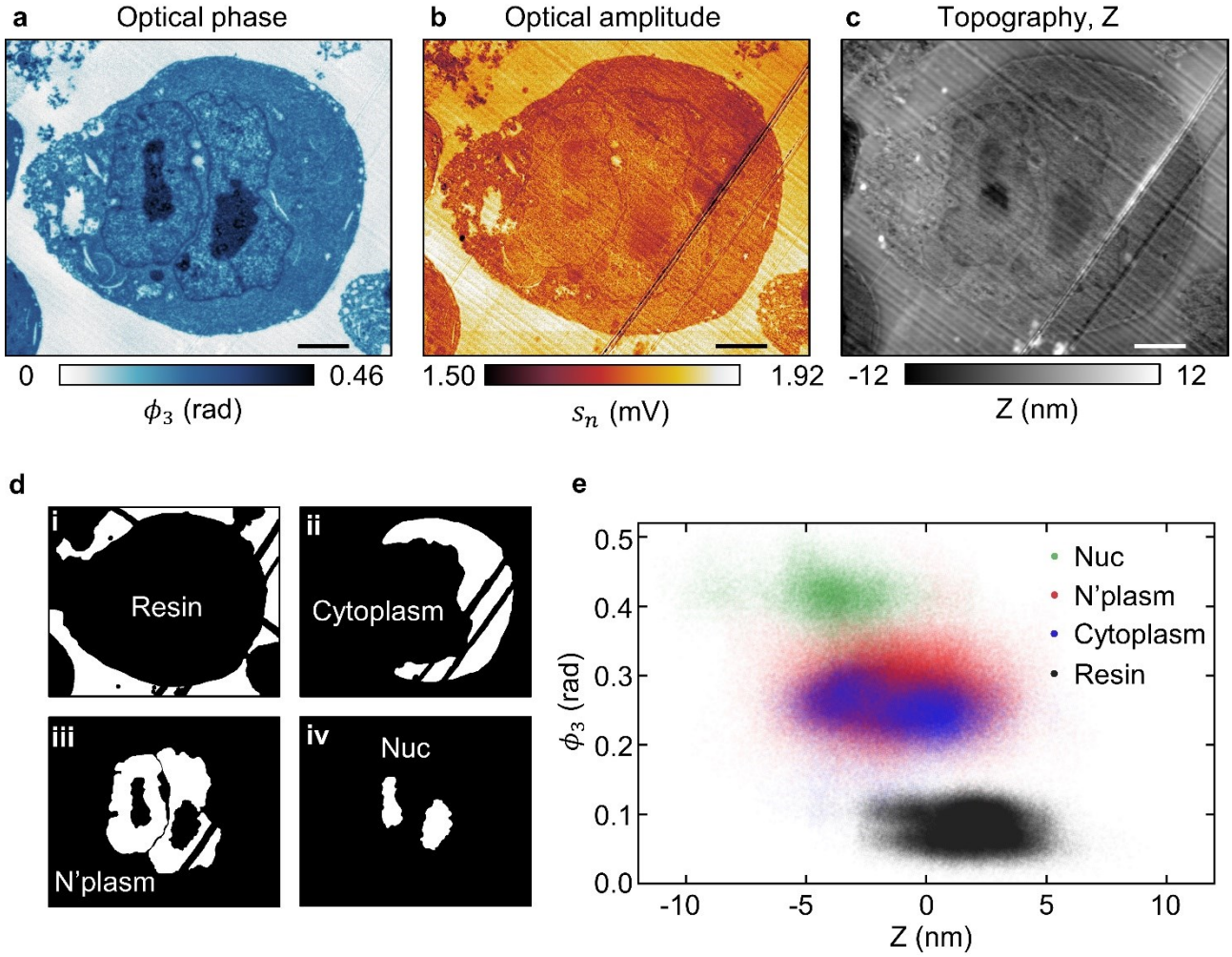

Figure 3.5 Optical and topographical image channels in s-SNOM. ***(a,b,c)*** *Mappings of the phase, amplitude and topography of a multiple myeloma cell respectively. Images acquired at 1667cm^{-1}. The image dimensions are 22µm x 18µm with 15nm pixel size. A pixel integration time of 3ms was used and thus the images took approximately 3 hours to acquire. The tapping amplitude was ~25nm.* ***(d, i-iv)*** *masks used to extract pixel values in cell regions.* ***(e)*** *Phase and topography values at each pixel. Scale bars 3µm.*

to small changes in the thickness of the section in different cellular regions, which might be because of different coefficients of thermal expansion, or expansion due to rehydration once sections have been cut. Since the s-SNOM signal depends on the thickness of the sample [122], the ability to identify structures from topography images raises the question of whether or not phase images contain additional information that is not explainable from the topography of the section.

To investigate the relationship between phase and topography and answer this question, the masks shown in figure 3.5 (d) (i-iv) were used to extract phase and topography measurements at pixels in the extracellular resin, cytoplasm, nucleoplasm and nucleoli regions, respectively. Regions affected

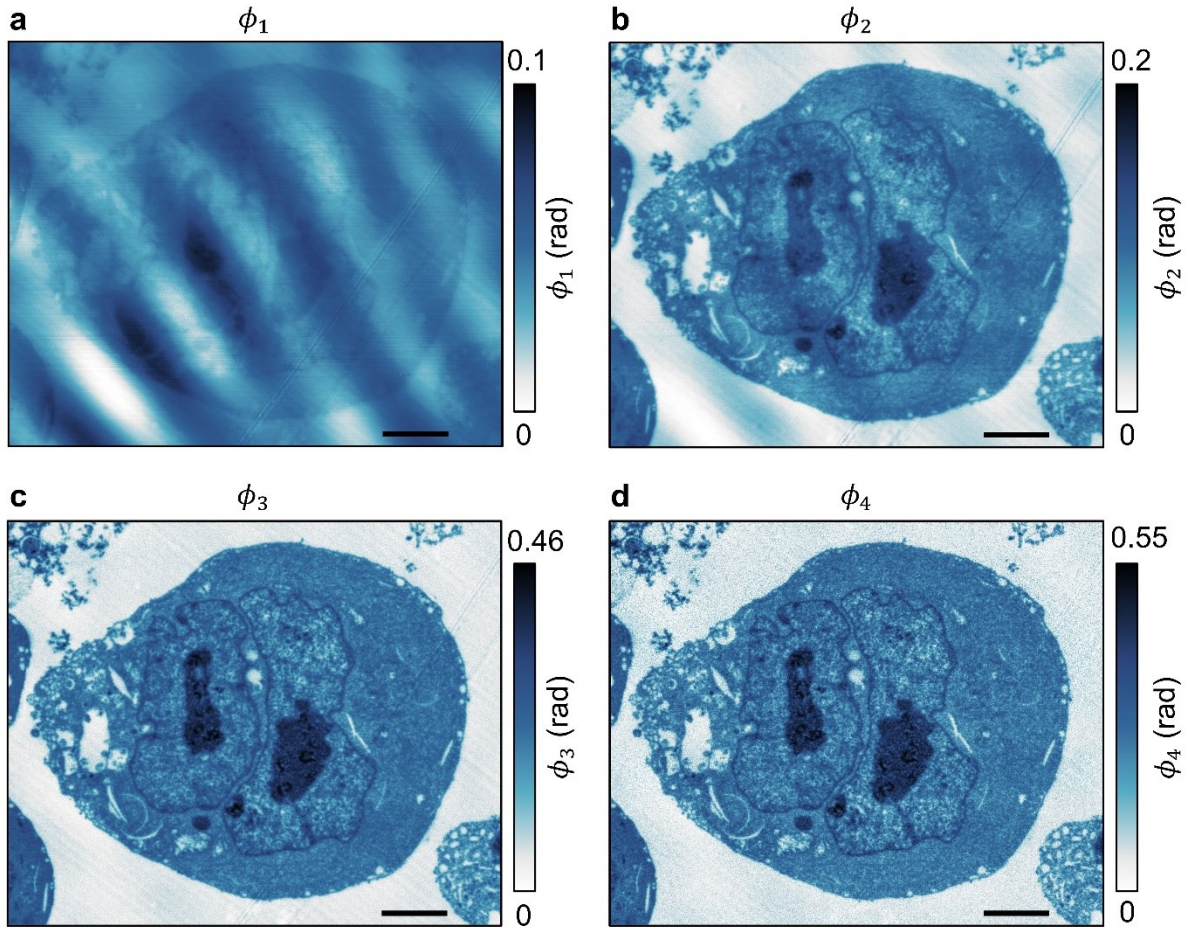

Figure 3.6 s-SNOM images at different harmonics of the probe frequency. *s-SNOM images of a multiple myeloma cell acquired at 1667cm^{-1} using the first (a), second (b), third (c) and fourth (d) harmonics of the probe oscillation frequency. The image dimensions are 22μm x 18μm with 15nm pixel size. A pixel integration time of 3ms was used and thus the images took approximately 3 hours to acquire. The tapping amplitude was ~25nm. Scale bars 3μm.*

by knife marks were excluded from masks of cell regions. Figure 3.5 (e) shows phase plot against topography for each pixel in the image, coloured by cell region. The resin, cytoplasm and nucleoli appear in distinct regions of the plot and variations in the thickness within each cell region has very little correlation with phase. This shows that topography is not a good predictor of the cell region, and therefore that the phase image provides additional (chemical) information.

3.3.2 Choosing a measurement harmonic

Figure 3.6 shows s-SNOM phase images at different harmonics of the probe oscillation frequency. At the first two harmonics (figure 3.6 (a & b)), there is a large background signal. It is expected that the origin of this background is the illumination of the probe, and it leaks into the signal recovered

with pseudoheterodyne detection because the probe experiences a changing illumination as it oscillates (as discussed in section 3.2.2). At the third and fourth harmonics (figure 3.6 (c & d)), this background signal is not present. In other words, this background signal has a low amplitude (in frequency space) at the third and fourth harmonics of the probe oscillation frequency.

Figure 3.6 also shows that there is increased contrast in higher harmonic images. This can be explained by considering the approach curves shown in figure 2.3 and recalling that, as discussed in section 2.2.2, a region close to the apex of the tip behaves like the low ζ case, whilst a region further up the shaft behaves like the high ζ case. Because the approach curves decay more quickly at higher harmonics, the contribution from a region close to the tip (low ζ) relative to the contribution from a region further up the shaft (high ζ) increases with each harmonic. Put simply, higher harmonics have a greater dependence on the tip apex. Parts of the tip closest to the apex are also more strongly influenced by the sample. Thus, at higher harmonics, the recovered signal is more sensitive to changes in the sample composition, which manifests as a larger phase difference.

Figure 3.6 also shows that there is more image noise in higher harmonic measurements. This is because the recovered signal at these harmonics is smaller, so the phase is measured with more noise. There is therefore a trade between contrast and noise when increasing the measurement harmonic. For the images shown in figure 3.6, both the third and fourth harmonics have relatively high contrast and low noise. However, in cases where a lower signal is obtained, such as when imaging at different wavelengths, or with different samples, fourth harmonic images sometimes become noticeably noisy, and third harmonic images are superior. Thus, for consistency, third harmonic images are presented in the rest of this thesis.

3.4 Conclusions

In this chapter, a metric known as the contrast-to-noise ratio was employed with the aim of obtaining the optimum imaging wavelength in the amide I band and the optimum tapping amplitude. The optimum imaging wavelength was deemed to be 1667cm^{-1}, which accounts for the spectral location where maximum contrast is exhibited, as well as the spectral dependence of atmospheric and laser

noise. The CNR metric failed to aid in obtaining the optimum tapping amplitude due to the introduction of a background signal at high tapping amplitude that isn't accounted for in the CNR calculation. It did, however, suggest that the tapping amplitude should be maximised as much as possible before the background signal becomes too large.

This chapter also discussed the different information that can be obtained from each of the imaging channels, namely the topography, the phase, and the amplitude. A plot of phase versus topography for each pixel in an image was shown to demonstrate that phase images provide additional chemical information compared to topography images. Finally, the choice to use third harmonic measurements was explained by considering the differences in contrast, noise and background signal associated with each measurement harmonic.

Chapter 4

Label-free nanoscale chemical mapping of multiple myeloma cells

This chapter is based on the publication:

Greaves, G.E., Kiryushko, D., Auner, H.W., Porter, A.E. and Phillips, C.C.

'Label-free nanoscale mapping of intracellular organelle chemistry'.

Communications Biology **6**(1)**:** p. 583 (2023).

https://doi.org/10.1038/s42003-023-04943-7

4.1 The need for label-free nanoscale imaging

The standard approach to intracellular imaging, electron microscopy (EM) (section 1.1.2), generally requires that specimens are stained with heavy metals to produce sufficient contrast in images. The

stains used in EM – most commonly osmium tetroxide, uranyl acetate and lead citrate – must be administered in specialist facilities due to their toxicity, and a trained practitioner is required to perform the procedure which typically takes several days [8, 146]. This creates a large barrier to ultrastructural imaging. Such 'blanket' stains enable identification of ultrastructure based on morphology, but it is very difficult to obtain any chemical information. Furthermore, only the structures which take the stain are revealed in images.

Chemical specificity can be achieved in EM through immunogold labelling, whereby gold nanoparticles are functionalised with antibodies to bind to molecules of interest in specimens [12]. The high electron density of gold provides contrast in EM images and reveals the location of the target molecules. The accuracy to which targets can be localised is inherently limited, however, by the size of the antibodies and gold nanoparticles used, and typically results in the gold particle being 15-30nm away from the target [12].

In super-resolution microscopy (section 1.1.3), specimens are labelled with fluorophores that are functionalised to bind to particular molecules so that molecules and intracellular structures can be identified. Fluorescent labels are specific to the problem at hand, however, and prior knowledge of the sample is often required for effective labelling. Also, variations in the labelling density can impair the ability to quantify the number of structures observed as well as their apparent sizes [147], which is a key aspect of microscopy. Further, the introduction of labels into the system may even perturb the biology of the specimen [148].

Practical limitations such as photobleaching of fluorophores can also make nanoscale resolution hard to achieve. Even if practical challenges are overcome, the accuracy to which targets can be localised is limited by the length of labels, with fluorophores and linking molecules typically being several nanometres in length [149].

4.1.1 Label-free imaging with s-SNOM

As mentioned in chapter 1, since the advent and commercialisation of tuneable infrared quantum cascade lasers, s-SNOM has increasingly been used to image biological systems. Many of these have been isolated biological specimens such as protein complexes [104, 105], oligonucleotides

[106], lipid monolayers [107] and bilayers [108], amyloid fibrils [109] and collagen fibrils [110]. Whole-cell imaging has been performed on neurons [113], E. coli cells [112] and red blood cells [114], but, since s-SNOM is a surface-sensitive technique, intracellular structures were not imaged in these experiments. Zebrafish retinal tissue has also been imaged [115], but intracellular structures were not identified. More pertinently, s-SNOM has recently been used to image single-cell green alga and E. coli cell sections [116], in which several intracellular structures such as nuclei and chloroplasts were identified.

Generating high quality (high contrast-to-noise ratio and high spatial resolution) s-SNOM images of intracellular structures remains challenging due to the small s-SNOM signals generated by biological samples, but it is hoped that the images presented here go some way to closing the gap between s-SNOM and techniques such as TEM. This chapter also provides an example of how s-SNOM might in future be used to study pathological states of cells. Here it is applied to an important human disease, multiple myeloma, where the crucial pathological mechanisms are exhibited at the cellular level [150].

4.2 Preparing multiple myeloma cells for s-SNOM and TEM imaging

To demonstrate intracellular imaging with s-SNOM, the technique is here used to image resin-embedded cell sections similar to those used by the EM community. This allows the chemical sensitivity of s-SNOM to be showcased whilst producing images that are recognisable to the EM community and can be cross-correlated with EM images. Cell sections can also be cut with very flat surfaces (height variations of a few nanometres), which reduces the chance of generating morphological artefacts in s-SNOM images and improves image quality. Additional sections cut from the same cell block are poststained with uranyl acetate and lead citrate and imaged with TEM. These images are compared with s-SNOM images and serve as validation for the identifications of structures made with s-SNOM.

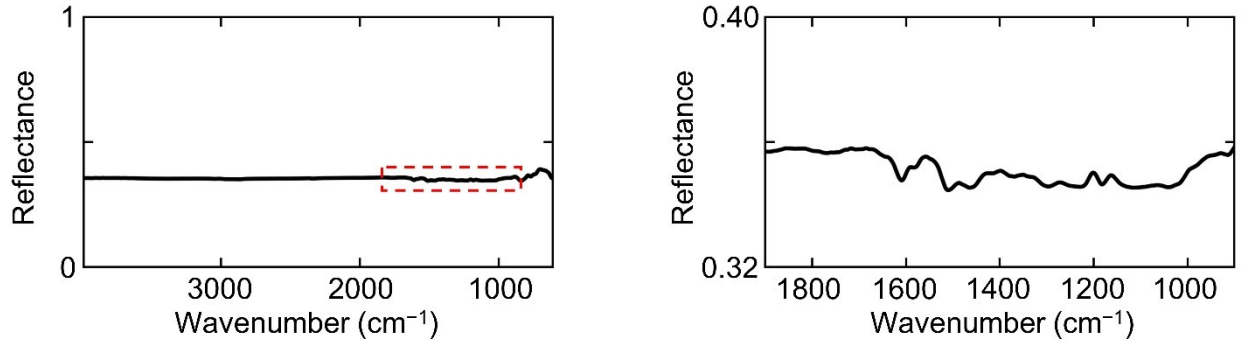

Figure 4.1 Reflectance of silicon wafer chips used as substrates for s-SNOM samples. *Reflectance of a silicon wafer chip measured with an FTIR spectrometer. The red boxed region (right) shows the spectral region important for s-SNOM measurements performed in this thesis.*

4.2.1 Sample preparation protocol

A typical TEM sample preparation protocol was used to produce a single cell block used for both s-SNOM and TEM imaging. The procedure was as follows (performed by Dr. Darya Kiryushko, Imperial College, adapted from [151]):

1. RPMI-8226 cells were grown in an RPMI 1640 medium supplemented with 10% fetal bovine serum, penicillin (100 U/mL), and streptomycin (100 µg/mL) as previously described [152].
2. 25×10^6 cells were pelleted, washed in 0.1 M 4-(2-hydroxyethyl)-1-piperazineethanesulfonic acid (HEPES) buffer (pH 7.2), fixed with 2.5% glutaraldehyde in HEPES for 2 hours at 4°C, and washed with HEPES in 3x10 minute cycles. Thereafter, pellets were dehydrated in a graded ethanol concentration (50%, 70%, 95%, and dry 100% v/v) each for 3x5 minute cycles, followed by 3x10 minute cycles in acetonitrile (Sigma-Aldrich, UK).
3. The samples were then progressively infiltrated with 50%, 75%, and 100% solutions of Quetol resin (Sigma) in acetonitrile at room temperature (50% resin for 2 hours, 75% resin overnight and two changes of 100% resin over 3 days) and cured at 60°C for 24 hours.
4. The embedded pellets were cut using a Leica UC7 ultramicrotome (Leica, Austria) with a 35° diamond knife (Diatome, Switzerland) to a thickness of 70–200nm. Sections were immediately collected on carbon-coated copper grids (Agar Scientific, UK) for TEM imaging, or on silicon wafer chips (NanoAndMore) for s-SNOM imaging.

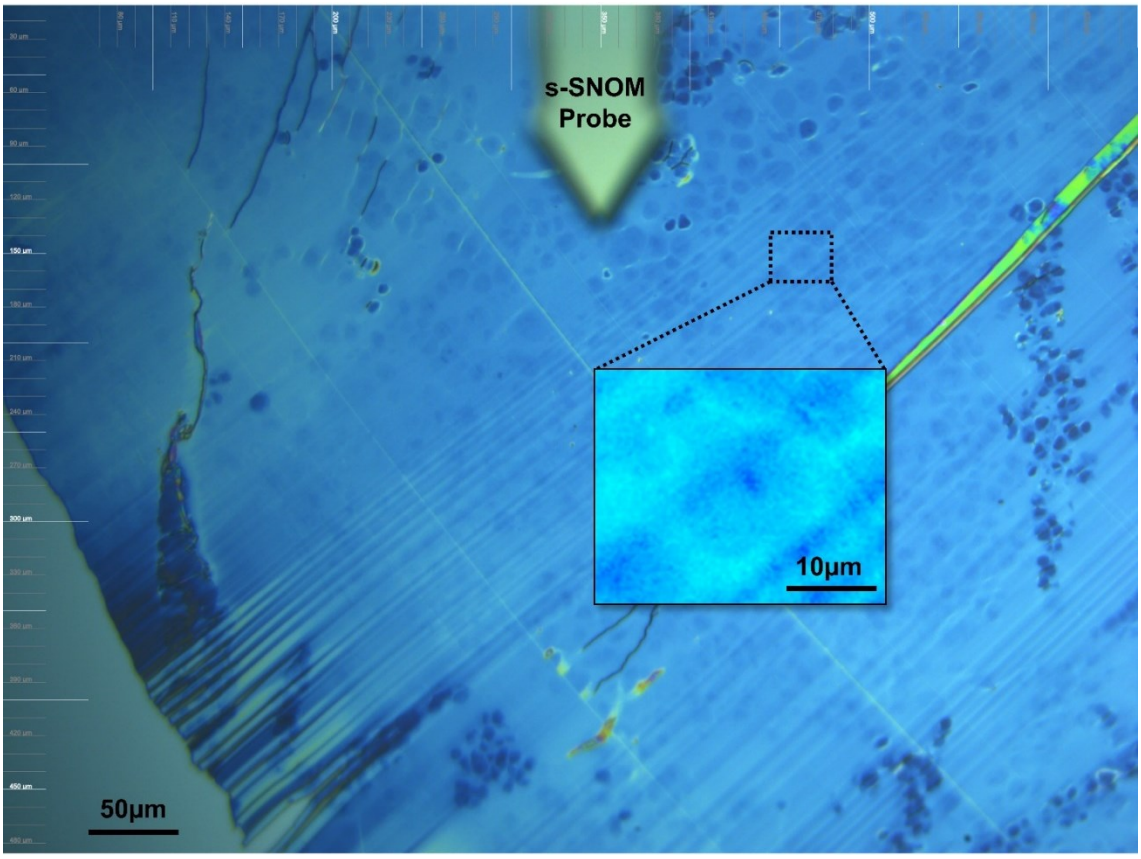

Figure 4.2 Optical microscope image of resin-embedded multiple myeloma cell sections. *Optical microscope image (20x magnification) of multiple myeloma cells prepared to the protocol described in section 4.2.1. Inset shows a region of the section and has been edited to maximise contrast.*

5. Sections used for TEM imaging were post-stained with 5% uranyl acetate (UA) and 3% lead citrate (LC) for 5 minutes each, both made up in double-distilled water.

4.2.2 Imaging with s-SNOM and TEM

s-SNOM imaging was performed with a commercially available s-SNOM system with a pseudoheterodyne detection module (NeaSNOM, NeaSpec, Germany) using platinum-iridium alloy s-SNOM probes (Arrow NCPt, Nanoworld, Switzerland) at a tapping amplitude of approximately 50nm. A QCL (MIRcat QT-2400, Daylight Solutions, USA) was used to generate imaging wavelengths in the 1020–1740cm^{-1} range. Various wavelengths in this range were used to target specific chemicals naturally occurring in the cells. Silicon substrates were used for s-SNOM samples due to their reflectivity, shown in figure 4.1, which boosts the s-SNOM signal [122]. TEM imaging of

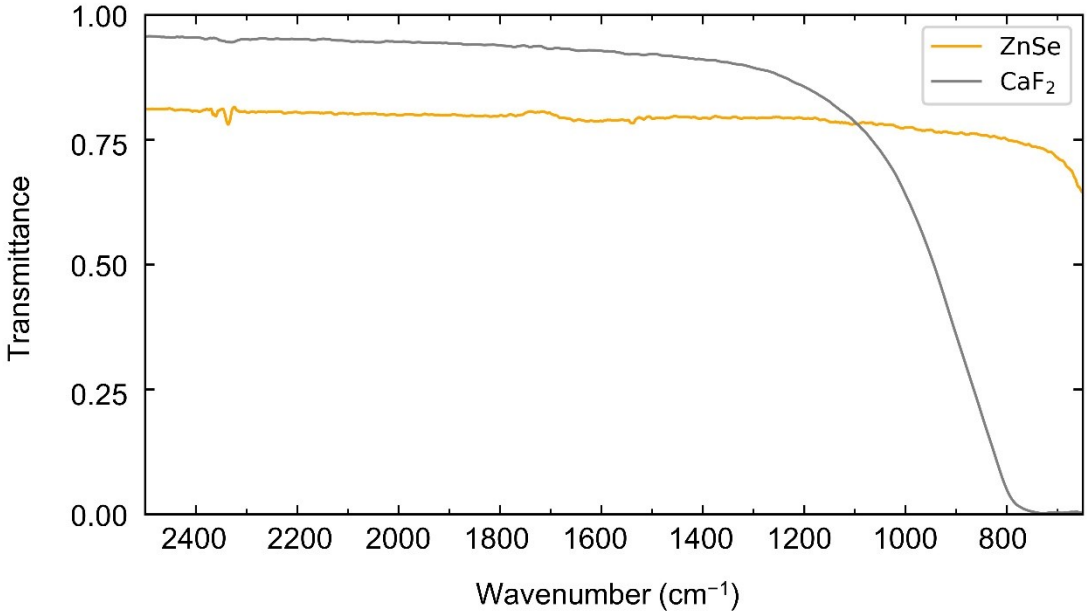

Figure 4.3 Transmittance of zinc selenide (ZnSe) and calcium fluoride (CaF_2) substrates. *The transmittance of ZnSe and CaF_2 substrates measured with an FTIR spectrometer.*

sections poststained with uranyl acetate and lead citrate was performed at 120kV on a JEOL 2100 TEM by Dr. Darya Kiryushko (Imperial College).

The s-SNOM images presented in this chapter are mappings of the third-harmonic phase quantity, ϕ_3, corresponding to the background-free local absorption of the sample. Gwyddion, an open-source software specifically designed for image analysis in SPM, was used to perform basic functions such as line-noise correction and extracting line profiles from image data.

A region of a section imaged with the built-in optical microscope in the s-SNOM system is shown in figure 4.2. Each section typically contains hundreds of cells. The inset shows one of the cells in greater detail and is edited to maximise contrast. The dark region near the centre of the cell is likely to be a nucleolus, but no other organelles are identifiable.

4.2.3 Obtaining far-field absorbance spectra

A Bruker Vertex Fourier transform infrared (FTIR) spectrometer with Hyperion microscope attachment was used to obtain far-field absorption spectra of myeloma cells. In the interest of obtaining absorption spectra without contributions from the embedding resin, nor any other embedding medium, absorption spectra were obtained for myeloma cells prepared with a standard

FFPE protocol and subsequently deparaffinised. Sections of FFPE cell blocks were cut to a thickness of 1µm using a Leica 1400 microtome (Leica, Germany) with 22° stainless steel blade (S22, Feather, Japan) and collected on calcium fluoride (CaF_2) microscope slides. CaF_2 was chosen due to its high transmittance of the wavelength range required, shown in figure 4.3. The transmittance of zinc selenide (ZnSe) is also shown, which also would have been a suitable substrate and is used for measurements in chapter 6. Sections were deparaffinised with xylene and ethanol and the FTIR spectrometer was then operated in transmission mode. Absorption spectra were also obtained for the resin-embedded cells imaged with s-SNOM. Sections were cut to a thickness of 500nm and collected on gold-coated coverslips. The FTIR spectrometer was then operated in reflection mode.

4.3 Results and discussion

The results presented in this chapter build on examples in the literature by using s-SNOM to image human multiple myeloma cell sections. The s-SNOM images reveal a wealth of ultrastructure, including some structures that have never been seen before directly optically at this spatial resolution. Identifications of intracellular structures are validated with TEM images of myeloma cells which are poststained with uranyl acetate and lead citrate to provide contrast.

Additionally, the imaging wavelength is tuned to target various absorption features in the cells and perform chemical mapping. Subsets of cell ultrastructure are isolated based on chemistry in a way that is traditionally only achieved with highly specific labelling.

4.3.1 Ultrastructure identification and validation with TEM

Figure 4.4 (a) is an s-SNOM image of a myeloma cell acquired at an imaging wavelength of 1667cm^{-1}. This wavelength excites vibrational modes in amide groups in proteins and nucleobases. As such, regions of the cell with high protein and nucleic acid density provide a stronger s-SNOM signal and appear darker in the pseudo colour scale applied to this image.

The morphological features in the image enable the identification of several intracellular structures such as a multi-lobed nucleus, typical of cancerous cells [153], outlined by a nuclear membrane (NM) and containing and nucleolus (Nuc). The nucleolus contains many proteins involved in

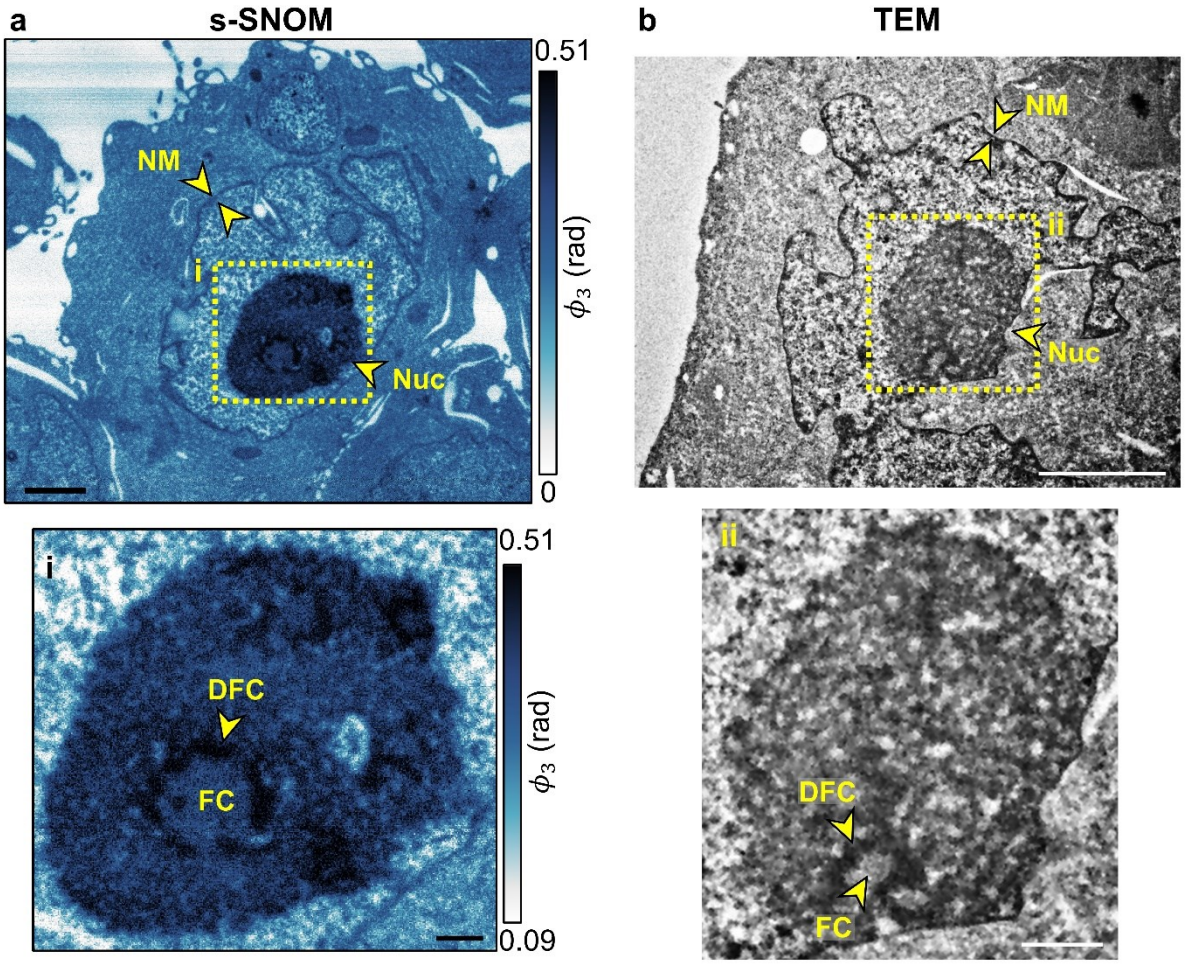

Figure 4.4 s-SNOM and TEM images of myeloma cells. (a) *s-SNOM image of a myeloma cell acquired at 1667cm^{-1} to excite amide moieties. The image dimensions are 16.8μm x 14.8μm with 12.5nm pixel size. A pixel integration time of 7ms was used and thus the image took approximately 6 hours to acquire. The tapping amplitude was ~30nm.* ***(b)*** *TEM image of a myeloma cell. Insets (i,ii) show nucleoli in greater detail. NM; nuclear membrane, Nuc; nucleolus, DFC; dense fibrillar component, FC; fibrillar centre. Scale bars 2μm (a,b), 500nm (i,ii).*

ribosome biogenesis, including fibrillarin, nucleolin and nucleophosmin [154-156], whilst the nuclear membrane contains proteins involved in transport and regulating gene expression [157]. Hence, both structures provide a strong s-SNOM signal at this wavelength, enabling their identification in a totally label-free way.

Other identifiable structures include a granular component in the nucleus known as chromatin, which is constituted by DNA tightly wound around histone proteins [158]. Inset i reveals several dense fibrillar components (DFCs) in the nucleolus, each with fibrillar centres with lower s-SNOM signal. The rest of the nucleolus is made up of a granular component [159]. The same intracellular structures

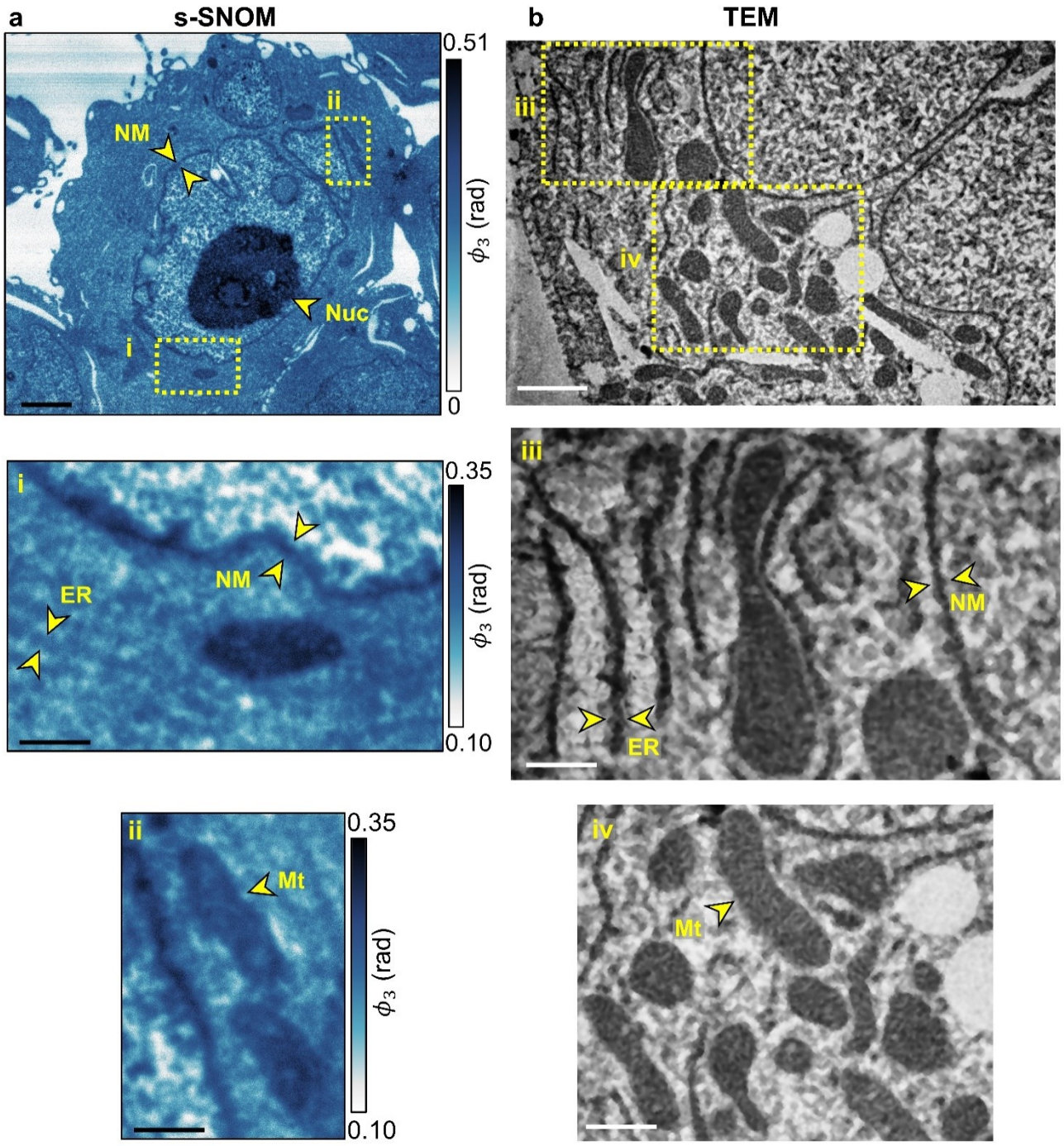

Figure 4.5 s-SNOM and TEM images of myeloma cells at higher resolution. (a) *Two regions (i,ii) of a myeloma cell imaged with 2nm pixel size enables visualisation of endoplasmic reticulum (ER) and mitochondria (Mt). The image dimensions are 3μm x 2μm for (i) and 1.5μm x 2.2μm for (ii). A pixel integration time of 7ms was used and thus (i) took approximately 6 hours to acquire and (ii) took approximately 3 hours to acquire. The tapping amplitude used for both images was ~53nm.* ***(b)*** *TEM images of ER and Mt show similar morphology. Scale bars 2μm (a), 1μm (b), 500nm (i-iv).*

identified in the s-SNOM images are also seen in the TEM image in figure 4.4 (b) and inset ii, supporting the identifications made in the s-SNOM images.

In figure 4.5 (a), higher resolution s-SNOM images (2nm pixel size) are shown in insets i and ii. These images allow the identification of endoplasmic reticulum (ER) and mitochondria (Mt), two deeply sub-wavelength structures that are visible at this wavelength due to their high protein content [160, 161]. Similar morphology is seen in TEM images of ER and Mt (figure 4.5(b)), supporting the identifications made with s-SNOM.

4.3.2 Multi-wavelength chemical mapping

Figure 4.6 (a) is a far-field absorption spectrum of myeloma cells that have been prepared with an FFPE protocol, sliced to a section thickness of 1μm, and deparaffinised so that the paraffin used for embedding does not contribute to the measured absorption. The amide I and II bands are aggregates of many vibrational modes of amide moieties in proteins and nucleobases. Both bands are routinely used to analyse the protein content of samples [138].

The band labelled PO_2 is predominantly constituted of vibrational modes of phosphodiester (PO_2) moieties found in the backbone of nucleic acids, as well as lipids and carbohydrates. It has been shown that this band can be used together with the amide I band as a reliable biomarker for cancer [162]. The band labelled C-O is largely made up of vibrational modes of C-O bonds in ribose, the five-carbon sugar in nucleic acids, as well as C-O bonds in lipids and carbohydrates. Both the PO_2 and C-O bands are routinely used for analysing nucleic acid contents of biological specimens [139].

Figure 4.6 (b) (i-iv) are s-SNOM images of a single myeloma cell acquired at wavelengths representing each of the bands indicated in the absorption spectrum in figure 4.6 (a). Figure 4.6 (b) (i) was acquired with a wavelength in the amide I band and therefore maps the amide density in the cell. Figure 4.6 (b) (ii) also maps the amide density but instead uses a wavelength in the amide II band. The same structures are identifiable in the image – namely the nuclear membrane, nucleolus and the granular pattern formed by chromatin – but all exhibit lower levels of absorption. This corresponds to the difference in the absorption peak heights in the absorption spectrum in figure 4.6 (a). In both images, the ubiquity of proteins in cells results in the entire cell exhibiting strong absorption compared to the embedding resin, which absorbs weakly at each of these wavelengths.

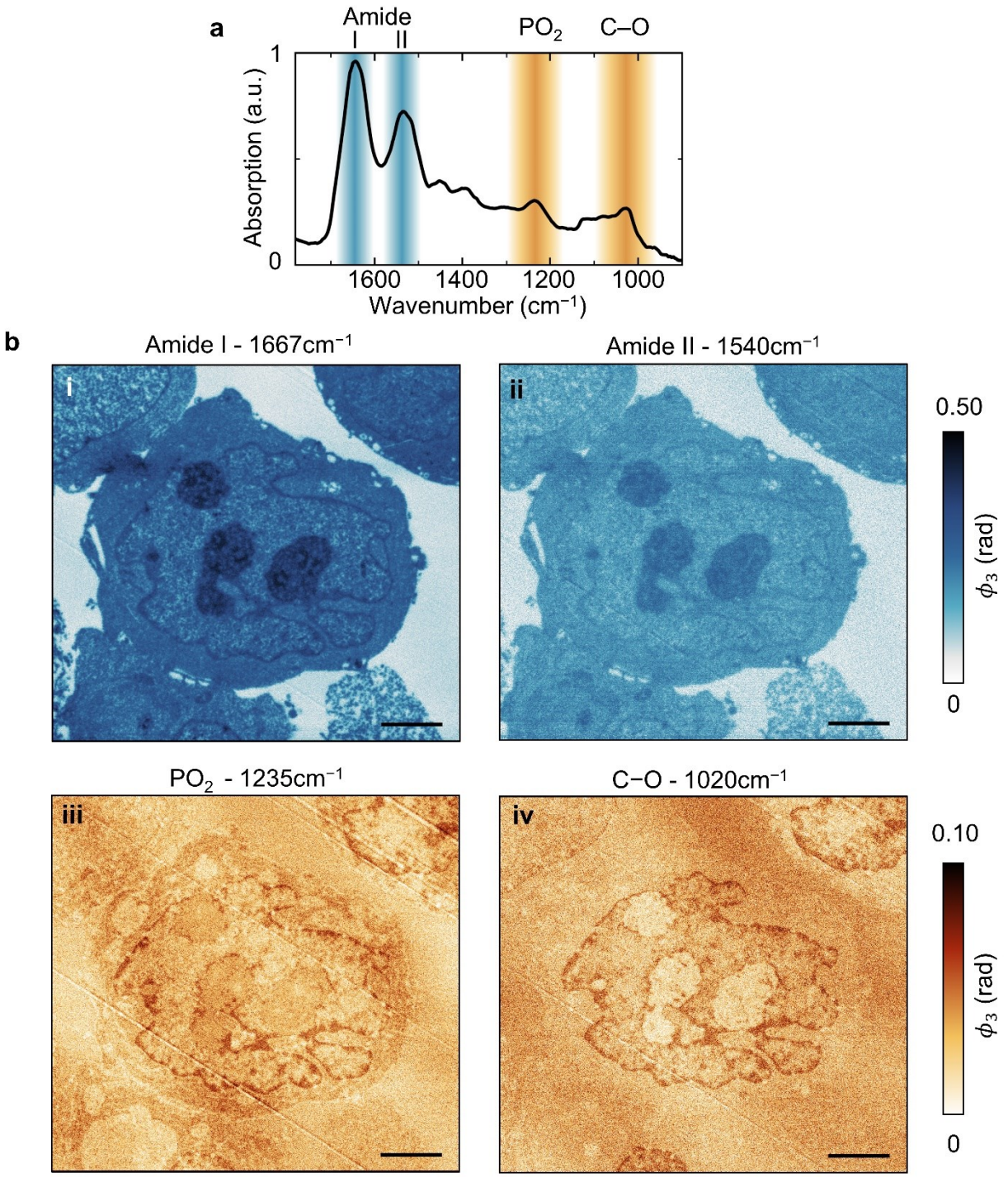

Figure 4.6 Multi-wavelength chemical mapping of myeloma cells with s-SNOM. (a) *Far-field absorption spectrum of deparaffinised myeloma cell sections (FFPE preparation) acquired with an FTIR spectrometer.* ***(b)*** *s-SNOM images of resin-embedded myeloma cells acquired with wavelengths representing each band indicated in (a). The image dimensions are 13μm x 12μm with 15nm pixel size. A pixel integration time of 3ms was used and thus the images each took approximately 1 hour and 10 minutes to acquire. The tapping amplitude used was ~59nm. Scale bars 2μm.*

Figure 4.6 (b) (iii) and (iv) are s-SNOM images acquired at wavelengths in the PO_2 and C–O bands respectively. Strong absorption is exhibited close to the nuclear membrane and at the periphery of

nucleoli at both wavelengths. This is attributed to the presence of chromatin, which is densely packed with nucleic acids [158]. The nucleoli and much of the cytoplasm exhibit greater absorption at 1235cm^{-1} than at 1020cm^{-1}. This is attributed to the presence of phospholipids in these regions [157], which have many active vibronic modes in the PO_2 band, but far fewer at the edge of the C–O band [139]. It is therefore surmised that the imaging wavelength of 1020cm^{-1} is more suitable for isolating structures containing nucleic acids.

4.3.3 Isolating ultrastructure in nucleoli

Figure 4.7 shows a myeloma cell imaged in the amide I and C–O bands which map the amide and nucleic acid densities respectively. Insets i and ii show one of the nucleoli in higher resolution and allows deeply sub-wavelength structures to be identified. In inset i, several strongly absorbing DFCs can be seen. Interestingly, the DFCs are not visible in inset ii, suggesting that they have a low density of nucleic acids. Conversely, there are regions of high nucleic acid density in inset ii, indicated with cyan arrows, that are not detectible in inset i, suggesting that they have a low protein density. This is a demonstration of how the tuneability of the imaging wavelength allows subsets of cell ultrastructure to be isolated based on their constituent chemicals.

The spatial variation of the s-SNOM signal across one of the DFCs (the magenta line in inset i) is shown for both imaging wavelengths in figure 4.7 (c). This confirms that DFCs are detectable when mapping with an imaging wavelength in the amide I band but not in the C–O band. Figure 4.7 (d) shows the spatial variation in the s-SNOM signal across the strongly absorbing structures in inset ii (magenta line) at both imaging wavelengths. Whilst there are variations in the amide density along this line, it is not correlated with the nucleic acid density.

4.3.4 Contributions from the embedding resin to the s-SNOM signal

The resin used for embedding the myeloma cells also exhibits absorption in the range of wavelengths used to image cells here. Figure 4.8 (a) is an absorption spectrum of the embedding resin acquired with an FTIR spectrometer. A region of a section without any cells was used to generate this spectrum. The spectrum shows two main absorption features in the resin. The first, centred at 1735cm^{-1}, is attributed to the stretching of C=O bonds. The second feature, peaking at 1155cm^{-1},

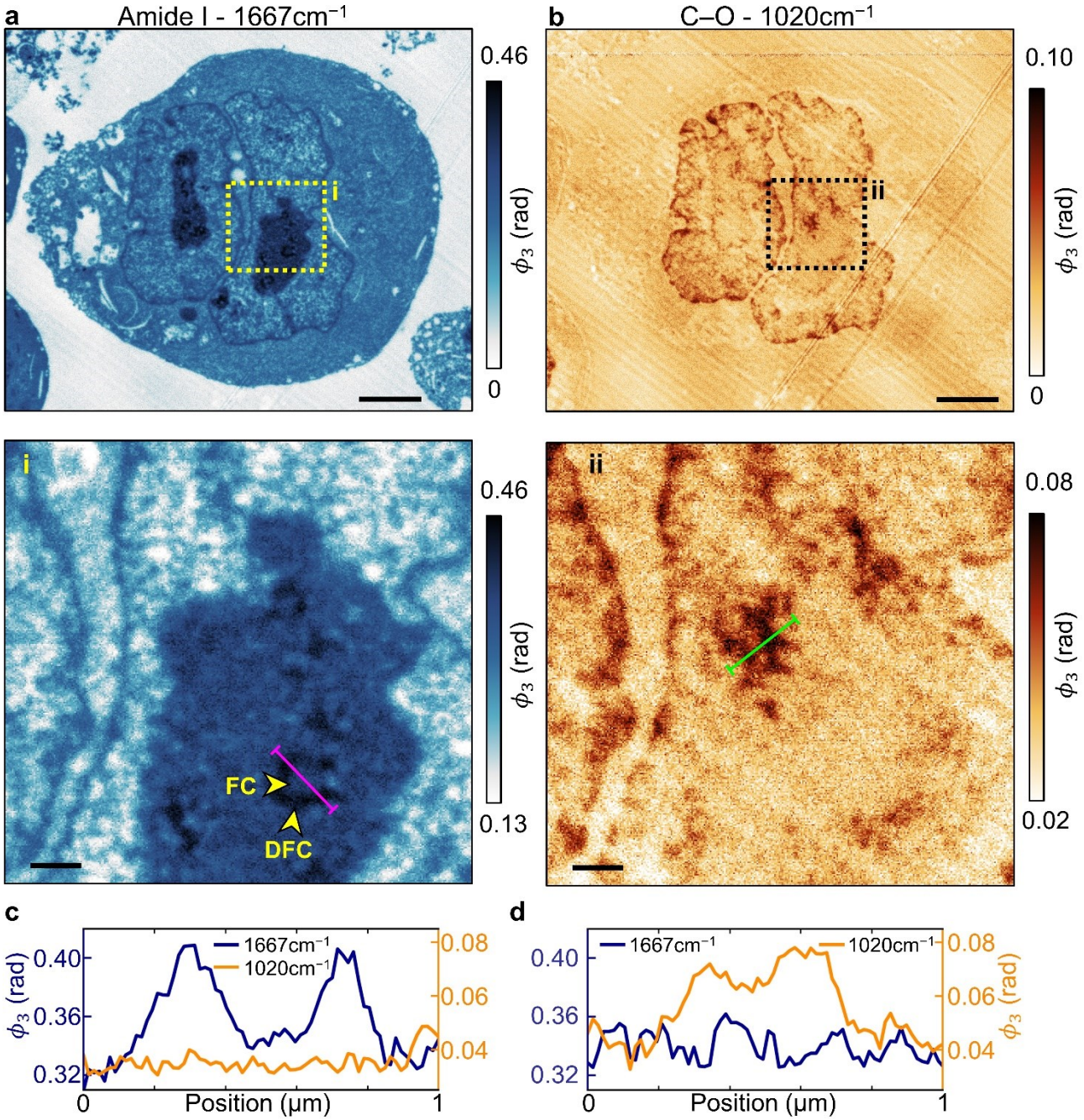

Figure 4.7 Isolating ultrastructure using multi-wavelength chemical mapping. ***(a)*** *s-SNOM image of a myeloma cell acquired at 1667cm^{-1} to excite amide moieties.* ***(b)*** *s-SNOM image of the same myeloma cell acquired at 1020cm^{-1} to excite C–O bonds in nucleic acids. The image dimensions of (a) and (b) are 22μm x 18μm with 15nm pixel size. A pixel integration time of 3ms was used and thus the images each took approximately 3 hours to acquire. The tapping amplitude used was ~25nm.* ***(c)*** *Profile of the s-SNOM signal across a dense fibrillar component (DFC) and fibrillar centre (FC) at both imaging wavelengths.* ***(d)*** *Profile of the s-SNOM signal across a region of high absorption in (b) at both imaging wavelengths. Profiles are averaged over a width of 75nm (5 pixels). Scale bars 3μm (a,b) and 500nm (i,ii).*

is attributed to the stretching of C–O–C bonds in epoxy groups in the resin. The absorption feature at 1735cm^{-1} is spectrally narrow which should mean that the embedding resin has little contribution

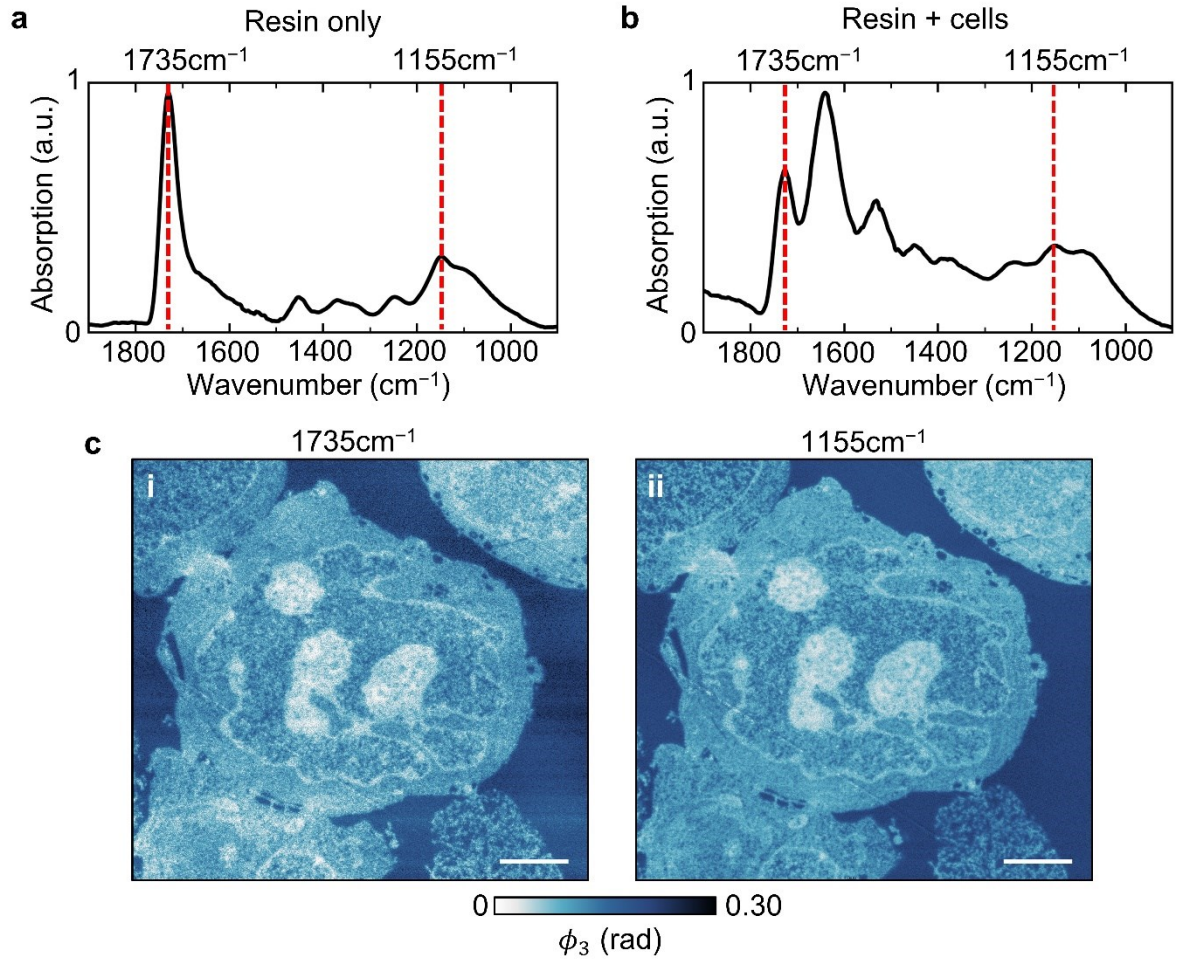

Figure 4.8 Absorption features in the embedding resin. ***(a)*** *Far-field absorption spectrum of Quetol embedding resin in an area of a section without any cells.* ***(b)*** *Far-field absorption spectrum of resin-embedded myeloma cells.* ***(c)*** *s-SNOM images acquired at the wavelengths indicated in (a) and (b), where the resin absorbs strongly. The image dimensions are 13μm x 12μm with 15nm pixel size. A pixel integration time of 3ms was used and thus the images each took approximately 1 hour and 10 minutes to acquire. The tapping amplitude used was ~59nm. Scale bars 2μm.*

to the s-SNOM signal when imaging at a wavelength in the amide I band. The absorption feature at 1155cm^{-1} is broader and overlaps with much of the C–O band. The resin therefore contributes to the s-SNOM signal at wavelengths in the C–O band, but imaging at 1020cm^{-1}, at the edge of this absorption feature, limits its contribution.

Figure 4.8 (b) is an absorption spectrum of a region of a section containing cells and therefore shows the absorption features of both the embedding resin and the cells. Absorption in the 1000–1500cm^{-1} range appears to be dominated by the resin, but this is because there is a large amount of resin contributing to this absorption spectrum and it is not representative of the local absorption measured in s-SNOM. In figure 4.8 (c), the same myeloma cell in figure 4.6 is imaged at wavelengths at which

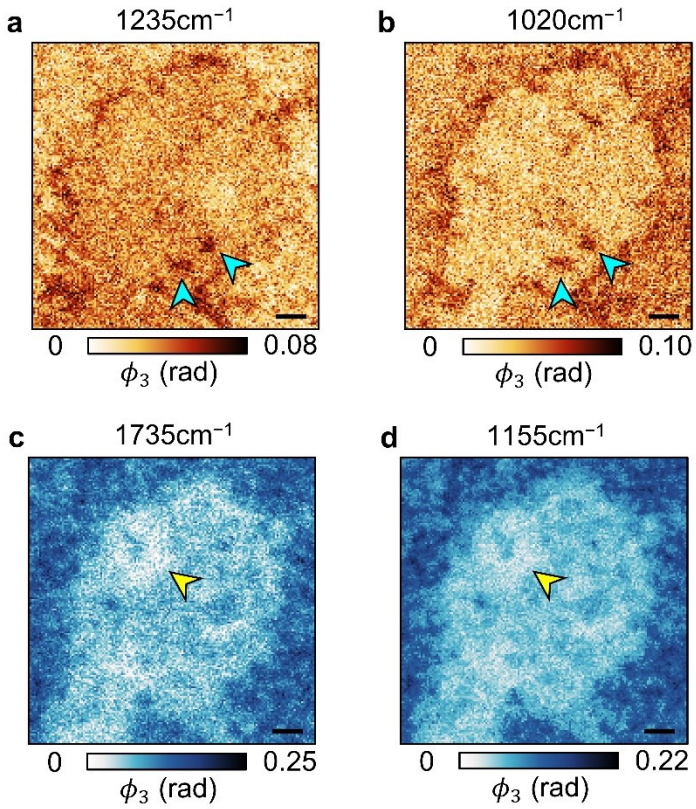

Figure 4.9 Distribution of embedding resin in nucleoli. *s-SNOM images of multiple myeloma celll nucleoli at 1235cm^{-1} (a), 1020 cm^{-1} (b), 1735 cm^{-1} (c) and 1155 cm^{-1} (d). The image dimensions are 2.25μm x 2.25μm with 15nm pixel size. A pixel integration time of 3ms was used and thus the images each took approximately 2 minutes to acquire. The tapping amplitude used was ~59nm. Dense fibrillar components (yellow arrows) can be identified from embedding resin distribution. Dense nucleic acid regions (cyan arrows) are not identifiable from embedding resin distribution. Scale bars 250nm.*

the resin absorbs strongly. This largely shows the distribution of resin throughout the cell and is informative of the extent to which the resin infiltrates different regions of the cell during the embedding process. Generally, the resin density is lowest where the amide density is highest, such as in the nuclear membrane and nucleoli. To put this another way, there is less resin infiltration in regions of the cell with high amide density and hence more cross-linking of proteins. Resultantly, mapping the resin density provides an additional mode of visualising intracellular structures, and might be informative of the cell density.

In figure 4.9, a myeloma cell nucleolus is imaged at wavelengths which excite PO_2 moieties (a), C–O bonds (b), C=O bonds in the embedding resin (c) and C–O–C bonds in epoxy groups in the embedding resin (d). Structures such as DFCs (yellow arrows) are identifiable in images (c) and (d) due to variations in the density of embedding resin. These structures are not present in images (a)

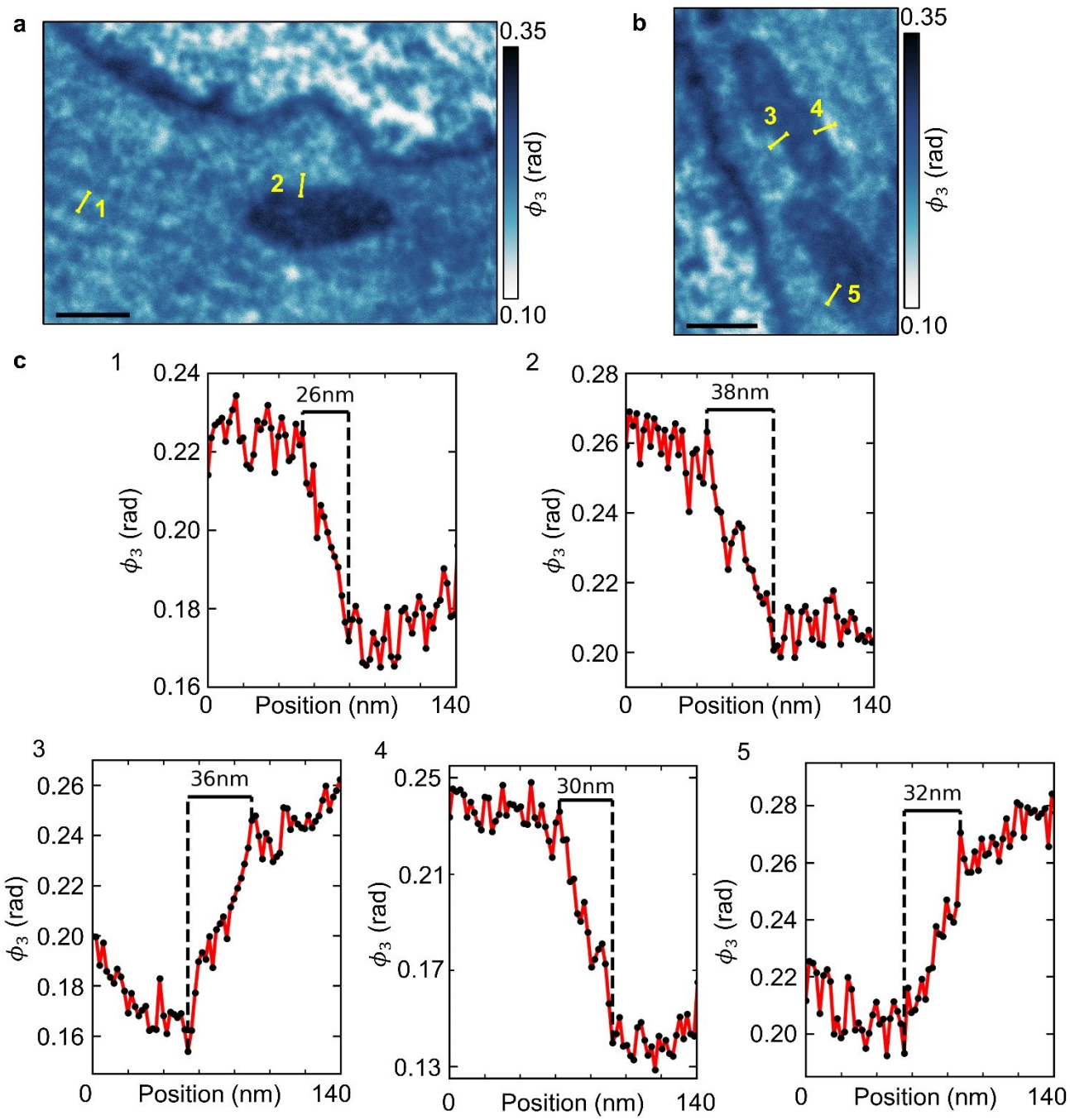

Figure 4.10 Spatial resolution of s-SNOM images. (a, b) *s-SNOM images of mitochondria and endoplasmic reticulum showing the locations of line profiles (1–5). The image dimensions are 3μm x 2μm for (a) and 1.5μm x 2.2μm for (b), both with 2nm pixel size. A pixel integration time of 7ms was used and thus (a) took approximately 6 hours to acquire and (b) took approximately 3 hours to acquire. The tapping amplitude used for both images was ~53nm.* ***(c)*** *Spatial profiles of the s-SNOM signal averaged over a width of 6nm (3 pixels). Scale bars 500nm.*

and (b). This suggest that, whilst the embedding resin likely contributes a small amount to the s-SNOM signal at the imaging wavelengths in (a) and (b), this contribution doesn't appear to cause the introduction of image artefacts. Additionally, structures with high nucleic acid density indicated

with the cyan arrows in (a) and (b) are not identifiable in (c) and (d), confirming that they are specific to the wavelengths they were imaged at and not artefacts of the embedding resin.

4.3.5 Spatial resolution of images

To quantify the spatial resolution of images, line profiles crossing boundaries of structures were extracted from the images in figure 4.10 (a) and (b). Line profiles (figure 4.10 (c)) were constructed by averaging over a width of 6nm (3 pixels), which was determined to be large enough to sufficiently reduce noise in the profiles, but not too large to be affected by the curvature of boundaries and other small-scale morphological features.

The line profiles in figure 4.10 (c) indicate a spatial resolution of approximately 30nm in these samples. The spatial resolution might be improvable towards the 5nm level reported in inorganic specimens [128] through refinement of the technique and through improvements in fixation and other sample preparation steps, which would help to better preserve the chemistry and morphology of samples. Using sharper tips might also improve the spatial resolution. This would come at the expense of image signal-to-noise, but if necessary this could be mitigated somewhat by using a more reflective substrate such as gold, or by making use of recent developments such as the use of IR nanoantennas incorporated into samples [105] or tip-enhancement techniques [163].

4.3.6 Detecting variations in cell chemistry

Figure 4.11 (a) shows s-SNOM images of three myeloma cells from the same cell block acquired with wavelengths in the amide I band (i–iii) and in the C–O band (iv–vi). The amide mappings appear characteristically different across the three cells. In figure 4.11 (a) (i), there is strong amide absorption in some parts of the cell such as the nucleolus, the nuclear membrane, endoplasmic reticulum, and various other organelles. Outside of these regions, the amide density is lower than it is in the other cells, and there are regions that exhibit the same s-SNOM signal as the extracellular resin and thus appear to contain a very low density of amide moieties. In figure 4.11 (a) (ii), the amide density in the nucleolus and nuclear membrane is similar to that of figure 4.11 (a) (i), but outside of these regions the amide density is greater. In figure 4.11 (a) (iii), the maximum amide density is similar to that in the other cells, but it is also much more uniform across the cell, making it

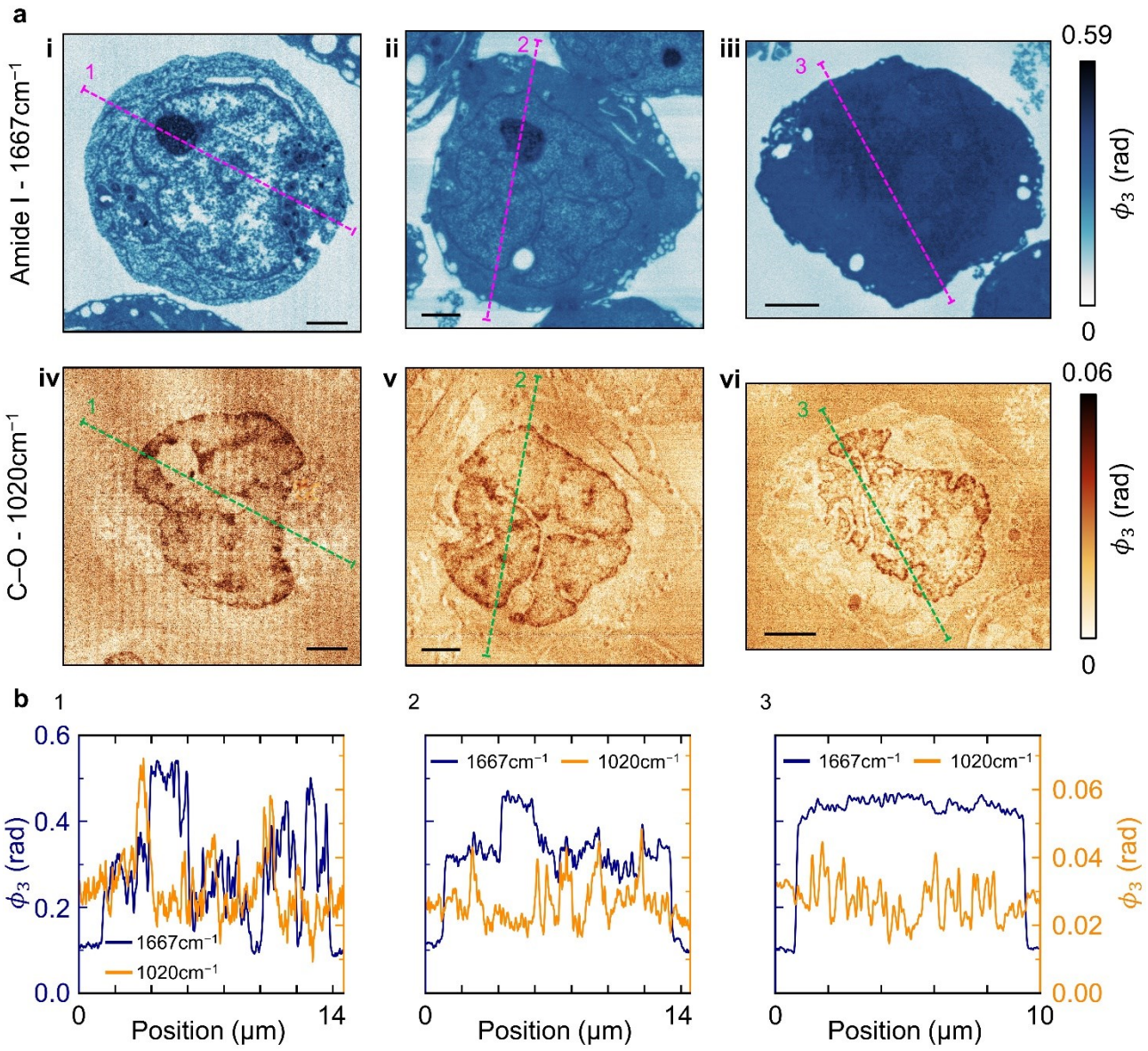

Figure 4.11 Chemical variations among cells. (a) *s-SNOM images of three cells acquired at 1667cm^{-1} (i,ii,iii) and at 1020cm^{-1} (iv,v,vi). The image dimensions are 14μm x 14μm for (i,iv), 15μm x 15μm for (ii,v) and 11μm x 10μm for (iii,vi). The pixel size is 10nm for (i,iv) and 15nm for (ii,iii,v,vi). A pixel integration time of 3ms was used for all images and thus (i,iv) each took approximately 3 hours and 15 minutes to acquire, (ii,v) each took 1 hour and 40 minutes to acquire and (iii,vi) each took approximately 50 minutes to acquire. The tapping amplitude used was approximately 30nm in each case.* ***(b)*** *s-SNOM signal along the lines shown in (a) at both imaging wavelengths. Profiles are averaged over a width of 10 pixels in (ii,iii,v,vi) and 15 pixels in (i,iv), equivalent to 150nm in all cases. Scale bars 2μm.*

difficult to identify intracellular structures. Figure 4.11 (b) shows the s-SNOM signal at both imaging wavelengths along lines shown in figure 4.11 (a). Line profiles were constructed by averaging over a pixel width equivalent to 150nm in each case. The line profiles confirm that the maximum amide

density in each cell is similar, but there is greatest variation in figure 4.11 (a) (i), and least in figure 4.11 (a) (iii).

In the images acquired at a wavelength in the C–O band (figure 4.11 (a) (iv–vi), there doesn't appear to be the same characteristic difference between the cells. In figure 4.11 (a) (v&vi), the s-SNOM signal appears to exhibit similar variations and is of approximately the same magnitude. Figure 4.11 (a) (iv) exhibits a slightly larger s-SNOM signal around the nuclear membrane region (and thus higher contrast), and this is confirmed in the line profiles shown in figure 4.11 (b).

At this stage, it is not clear whether the images shown in figure 4.11 (a) are representative of the full extent of the chemical variations exhibited by the entire population of cells. The reasons for the chemical variations are also unknown, although a first guess at this early stage is that they are representative of different stages of a cell's lifecycle. These first results demonstrate how s-SNOM might be used to characterise various processes through nanoscale chemical mapping. In future work, multi-wavelength imaging such as this should be performed on many more cells to allow quantities to be extracted from large samples.

4.4 Conclusions

In this chapter, s-SNOM has been used to image intracellular structures at the nanoscale without using stains or labels. Many intracellular structures have been identified based on morphology and these identifications have been validated with TEM images of cell sections that have been post-stained. Amongst the s-SNOM images are the first fully optical and deeply sub-wavelength images of endoplasmic reticulum, mitochondria, dense fibrillar components and fibrillar centres.

Various absorption features exhibited in biological specimens have been targeted by tuning the imaging wavelength. This enabled chemical mapping of the cells, in which morphological and chemical information are obtained simultaneously. Wavelengths in the amide I and II absorption bands were used to visualise protein dense regions of cells, whilst wavelengths targeting PO_2 and C–O absorption were used to visualise nucleic acid-dense regions of cells. This allowed subsets of

cell ultrastructure to be isolated, for example protein dense DFCs and regions of high nucleic acid density in the nucleolus.

A spatial resolution of approximately 30nm has been demonstrated, beating diffraction by around a factor of 100 for an imaging wavelength of 6μm. This is likely limited by the radius of the tip of the probe. Using sharper probes might yield a better spatial resolution if the decrease in signal-to-noise can be mitigated. There are not currently any commercial probes available that are significantly sharper, so attempts to improve spatial resolution might focus on developing bespoke probes.

Far-field absorption spectra revealed that the embedding resin contributes two main absorption features in the wavelength range used for imaging cells. Whilst this does not appear to impair with identifying ultrastructure or imaging with chemical sensitivity, it still contributes a background to the images which is important to account for if quantitative studies are performed. The same type of resin, hardener and curing procedure should be used for the results of different experiments to be compared.

4.5 Further work

4.5.1 Correlative s-SNOM and EM imaging

Correlative s-SNOM and EM imaging (that is, imaging the exact same cell with both techniques) would be highly useful to further validate the conclusions drawn from s-SNOM images. s-SNOM imaging was attempted with the samples prepared on copper grids for TEM. Unfortunately, it seems that the copper grid is insufficient as a thermal sink, resulting in sections being damaged by the heat of the laser. An alternative and more promising approach might be to use SEM to image s-SNOM samples (sections on silicon substrates) after coating the surface with a conductive layer.

If imaging the exact same section proves challenging, a more immediate solution might be to produce serial sections for imaging with TEM and s-SNOM, locating the same cell on serial sections with each technique. If sections are sliced thin enough, the morphology of many structures should be consistent enough across the two sections for validation purposes.

4.5.2 Nanoscale biomarkers

Biomarkers are measurable quantities that characterise biological processes and responses to exposure and therapy, with uses including diagnosis, monitoring, prediction and prognosis [164]. The quantitative chemical mapping presented in this chapter could be used to discover nanoscale biomarkers which provide clinical or research value where spatially resolved information at the subcellular level is important.

An example of a biomarker relevant to this work is the nuclear-to-cytoplasmic ratio (NCR) of cancerous tissues, which has been shown to correlate with the grade assigned to cases of breast cancer by pathologists, and can be obtained from measurements of tissue absorption at wavelengths in the amide I and PO_2 absorption bands [162]. Such measurements have so far only been demonstrated using diffraction limited techniques and therefore cannot resolve at the subcellular level. They therefore fail to capture the nanoscale changes in cells that contribute to the increased NCR. The chemical mapping demonstrated in this chapter could be used to study such nanoscale processes to better understand the development of cancers.

Machine learning has recently been demonstrated to be a useful tool for extracting pathological value from SPM images [165]. It can be expected that the chemical information obtainable with s-SNOM would make a useful feature in predictive models to complement morphological and mechanical-based features available with other SPM techniques.

Chapter 5

Simultaneous mapping of cell chemistry and nanoparticle theranostics in hippocampal neurons

This chapter is based on the publication:

Greaves, G.E., Allison, L., Machado, P., Morfill, C., Fleck, R.A., Porter , A.E. and Phillips, C.C. 'Infrared nanoimaging of neuronal ultrastructure and nanoparticle interaction with cells' Nanoscale, **16**, 6190-6198 (2024).

https://doi.org/10.1039/D3NR04948E

5.1 Why label-free chemical mapping is important in nanomedicine

Nanomedicine is the use of nanotechnology for the treatment and prevention of disease. It encompasses sensing, diagnosis and the delivery of drugs and other therapeutics to cells and tissues [166]. A large branch of nanomedicine, nanoparticle theranostics (NPTs), concerns using nanoparticles that are modified to perform multiple functions including cell targeting, imaging and drug delivery [167]. NPTs are often made of noble metals such as gold [168] or inorganic materials such as silica [169]. In such cases, their high electron densities relative to the biological material allow them to be visualised in EM [170, 171]. NPTs can also be visualised with fluorescence techniques if they are first modified with fluorescent labels [172].

Typical applications within the field of nanomedicine involve determining the uptake and intracellular location of NPTs in cells as part of studying the operational mechanisms and efficacy of the drugs they are carrying [171-173]. One major challenge is understanding how NPTs interact with organelles, and, in particular, how the health and biochemistry of organelles is affected. In this instance, imaging with chemical sensitivity is key.

5.1.1 EM and super-resolution imaging in nanomedicine

Super-resolution microscopy techniques have been used extensively for imaging the distribution of nanoparticle theranostics in cells [172, 174]. In addition to labelling nanoparticles, fluorescent labels can be used to label cellular components to understand how, for example, cell metabolism and biochemistry are affected in relation to the distribution and uptake of NPTs. However, there are several limitations to using fluorescent-based techniques. Primarily, fluorophores can become dissociated from nanoparticles, resulting in inaccuracies in locating NPTs [175]. Secondly, if cells are not suitably labelled, some of the biochemical response to the NPTs might go undetected. It is also possible that modifying NPTs with fluorescent labels might interfere with their targeting or treatment functionalities. These limitations are in addition to the limitations discussed in chapter 4,

which include the limit on resolution set by the size of fluorescent molecules and linkers [149], as well as the potential for perturbations to the sample biology [148].

TEM can also be used to map the distribution and measure the uptake of NPTs in cells [171, 176], but generally only provides morphological information and not the chemical information that is required. In some instances, TEM can be combined with electron energy loss spectroscopy (EELS) to obtain information about the elemental composition of samples. This combination has been employed to image cellular structures and interactions of nanomaterials with cell organelles [15]. However, it is extremely difficult to image with chemical specificity at the nanoscale resolutions required since samples are prone to electron beam damage.

5.1.2 s-SNOM imaging in nanomedicine

s-SNOM has enormous potential as an imaging technique for applications in nanomedicine, owing to its ability to simultaneously map nanoparticle distribution and cell chemistry. Crucially, this can be done in a label-free way, avoiding the problems associated with labelling listed in the last section.

s-SNOM has recently been used to image polymer-coated gold nanoparticles (AuNPs) [177], which have a multitude of applications in nanomedicine [178, 179]. However, s-SNOM has so far not been employed for imaging cells treated with NPTs. There has been more interest in nanomedicine applications using AFM-IR techniques (section 1.1.5) [180], including the imaging of polymeric nanoparticles in whole THP-1 macrophages [181]. However, AFM-IR can suffer from poor spatial resolution, since probing depths in samples can be large and translate into poor lateral resolution through thermal transport [182]. s-SNOM, on the other hand, is highly surface sensitive, and might provide better spatial resolution, thus having a greater impact in the field of nanomedicine.

5.2 Preparing nanoparticle theranostic-treated neurons for s-SNOM and TEM imaging

In this chapter, s-SNOM is demonstrated as an imaging tool for applications in nanomedicine by simultaneously mapping cell chemistry and nanoparticle theranostics in hippocampal neurons

(henceforth referred to as neurons). Neurons are treated with gold nanoparticles (AuNPs) that are conjugated with peptide dendrimers (branch-like polymers containing peptide bonds). The peptide dendrimers used, H3 and H6, mimic the neuroprotective properties of the protein S100A4 and have previously been shown to protect against neurodegenerative diseases [176, 183]. H3- and H6-conjugated AuNPs have previously been imaged in hippocampal neurons using TEM [171]. By imaging this same system using s-SNOM, it is here shown that s-SNOM can be used to reliably map NPTs and can additionally provide chemical information that cannot be obtained with TEM.

The NPT-treated neurons were originally prepared for use in TEM only. This means, as well as being fixed and resin-embedded, the neurons have additionally been osmicated (that is, they are stained with osmium tetroxide (OsO_4)). Whilst this wasn't desirable when imaging myeloma cells in chapter 4, here it has led to obtaining the first s-SNOM images of osmicated cells, and to observing the benefits of osmicating, such as the preservation of membranous structures through the fixation of lipids [184].

5.2.1 Sample preparation protocol

The process for producing sections of hippocampal neurons treated with peptide dendrimer-conjugated AuNPs was as follows (adapted from [185]). Step 1 was performed by Dr Corinne Morfill, Imperial College. Steps 2–4 were performed by Dr. Darya Kiryushko, Imperial College. Steps 5–8 were performed by Pedro Machado and Leanne Allison, both of King's College London.

1. Gold nanoparticles (spherical and star-shaped) were synthesised using a surfactant-free seed-mediated method as described in Yuan et al. [186]. This starts with 12nm gold 'seeds' and, depending on the conditions [171], yields either spherical nanoparticles or particles that are covered with gold spikes (star-shaped nanoparticles). H3 and H6 peptides were conjugated to the AuNPs through thiol modification as described in Morfill et al. [171]. Briefly, the peptide dendrimers are modified with a thiol (-SH) group, which enables conjugation to the AuNPs through a gold-sulphur bond.

2. Neurons were dissociated from pregnant Wistar rats (embryonic day 18) as described in Soroka et al. [187]. Briefly, this involves homogenising, trypsinizing (administering the

enzyme trypsin) and incubating to release cells from their adherent state. Wistar rats were from Charles River, UK and were handled in accordance with European Union (European Directive 2010/63/EU) and UK legislation.

3. Dissociated neurons were cultured on poly-L-lysine coated Thermanox coverslips (Thermo Fisher, UK) in RPMI 1640 medium supplemented with 10% fetal bovine serum, penicillin (100 U/mL) and streptomycin (100µg/mL).

4. Neuron cultures were treated with peptide dendrimer-conjugated AuNPs for 24 hours, rinsed with 0.1 M HEPES buffer (pH 7.2), fixed with 2.5% glutaraldehyde in HEPES for 2 hours at 4°C, and washed with HEPES in 3×10 minute cycles.

5. The fixed neurons were stained with osmium tetroxide (1% OsO_4 in HEPES for 1 hour at room temperature) to better preserve membranous structures and provide better contrast in TEM.

6. Neurons were washed six times with deionised H_2O, then dehydrated in a graded ethanol concentration (50%, 70%, 95%, and dry 100% ethanol) for 3×5 minute cycles each, and subsequently in acetonitrile (Sigma-Aldrich, UK) for 3x10 minute cycles.

7. A cell block was produced by progressively infiltrating with 50%, 75%, and 100% solutions of TAAB 812 resin (Sigma) in acetonitrile at room temperature (50% resin for 2 hours, 75% resin overnight, and three changes of 100% resin over 3 days) and cured at 60°C for 24 h.

8. Neuron sections were produced using a Leica UC7 ultramicrotome (Leica, Austria) with a 35° diamond knife (Diatome, CH). The section thickness was set to 70 nm. For s-SNOM imaging, sections were collected on silicon substrates. For TEM imaging, sections were collected on carbon-coated TEM copper grids (Agar Scientific, UK) and dried.

5.2.2 s-SNOM and TEM imaging of hippocampal neurons

TEM imaging of hippocampal neurons was performed at 120 kV (JEOL JEM 1400Plus, JEOL, Japan) by Pedro Machado, King's College London. s-SNOM imaging was performed with the setup described in section 4.2.2 using a tapping amplitude of approximately 50nm. Additional sections

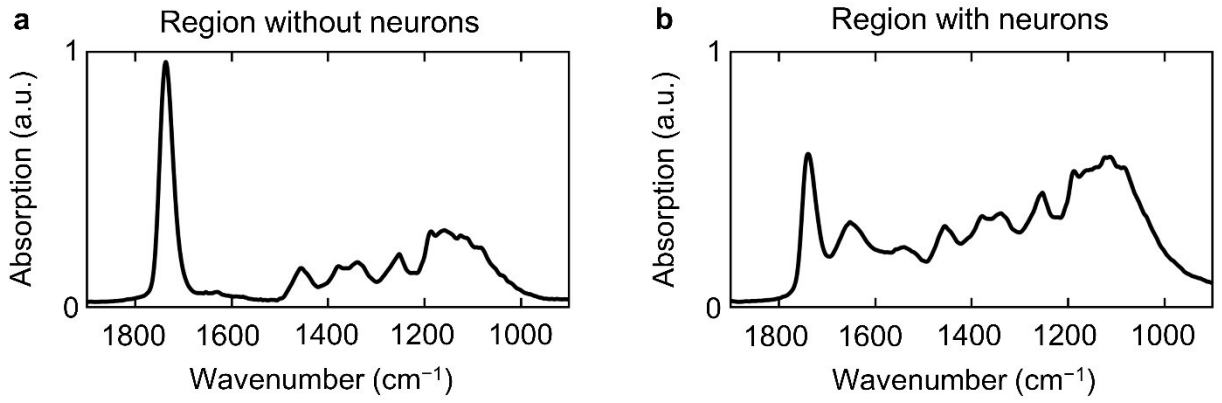

Figure 5.1 Absorption spectra of hippocampal neuron resin-embedded sections. *Absorption spectra acquired with an FTIR spectrometer in regions of the section without any neurons (a) and with neurons (b).*

were cut to 500nm thickness and deposited on gold-coated coverslips for use in a FTIR spectrometer. The absorption was subsequently measured in reflectance mode.

Note that a mixture of H3- and H6-treated neurons make up the images presented in this chapter. Since the focus is on mapping AuNPs and cell chemistry simultaneously, rather than detecting differences in the peptide dendrimers, no distinction is made between the two.

5.3 Results and discussion

The results presented in this chapter begin with s-SNOM images of osmicated hippocampal neurons shown together with TEM images of neurons from the same block of cells. Many intracellular structures are identified from the morphologies observed in the s-SNOM images and are validated by comparing with the supporting TEM images.

Following this, it is shown that osmication of the cells better preserves membranes, which is apparent through the visualisation of the plasma membrane. Notably, osmication also appears to improve the achievable spatial resolution when compared to that of the non-osmicated multiple myeloma cells in chapter 4.

Finally, simultaneous mapping of AuNP distribution and cell chemistry is demonstrated, showcasing how s-SNOM might be used for applications in nanomedicine. To add to this, s-SNOM images of three characteristic stages of AuNP internalisation are shown and are supported by TEM images.

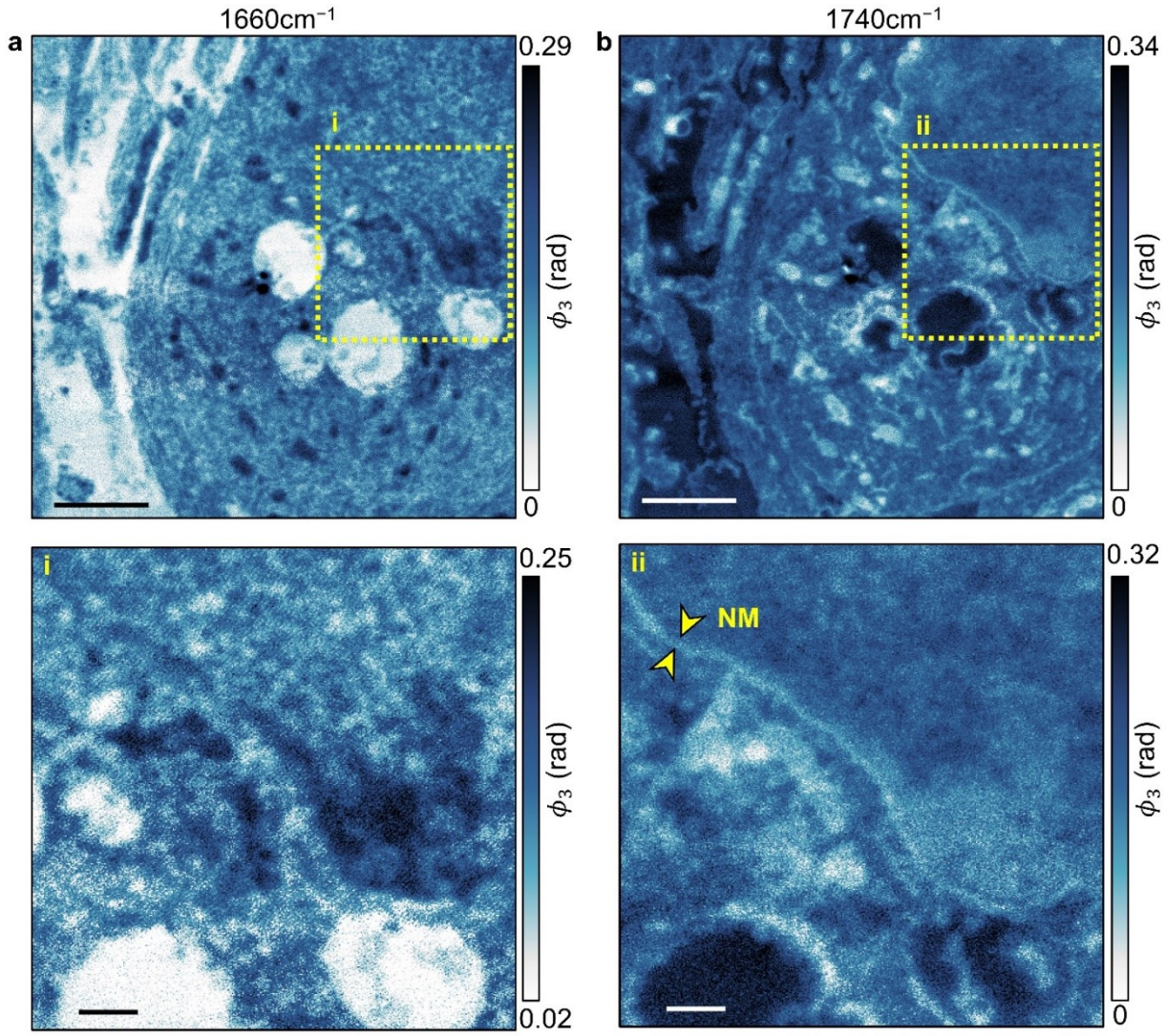

Figure 5.2 Multi-wavelength s-SNOM imaging of a hippocampal neuron. (a) *s-SNOM image acquired at an imaging wavelength of 1660cm^{-1}, mapping amide moieties in the cell.* ***(b)*** *s-SNOM image acquired at an imaging wavelength of 1740cm^{-1}, primarily mapping the resin density, although there may be contributions from lipids, the osmium tetroxide stain and fixatives. The image dimensions of (a) and (b) are 10μm x 10μm with 10nm pixel size. A pixel integration time of 3ms was used and thus the images each took approximately 1 hour and 40 minutes to acquire. The tapping amplitude was ~72nm. NM; nuclear membrane. Scale bars 2μm (a,b), 500nm (i,ii).*

5.3.1 Intracellular imaging of osmicated hippocampal neurons

Figure 5.1 (a) and (b) are absorption spectra of a resin-embedded neuron section acquired in a region without any neurons (blank resin) and with neurons, respectively. Like the Quetol resin used for the multiple myeloma cells in chapter 4, the TAAB 812 resin used here produces a strong absorption peak at approximately 1735cm^{-1}. The absorption features at lower wavenumbers differ for each type of resin, but both show strong absorption at around 1155cm^{-1}. In figure 5.1 (b), the

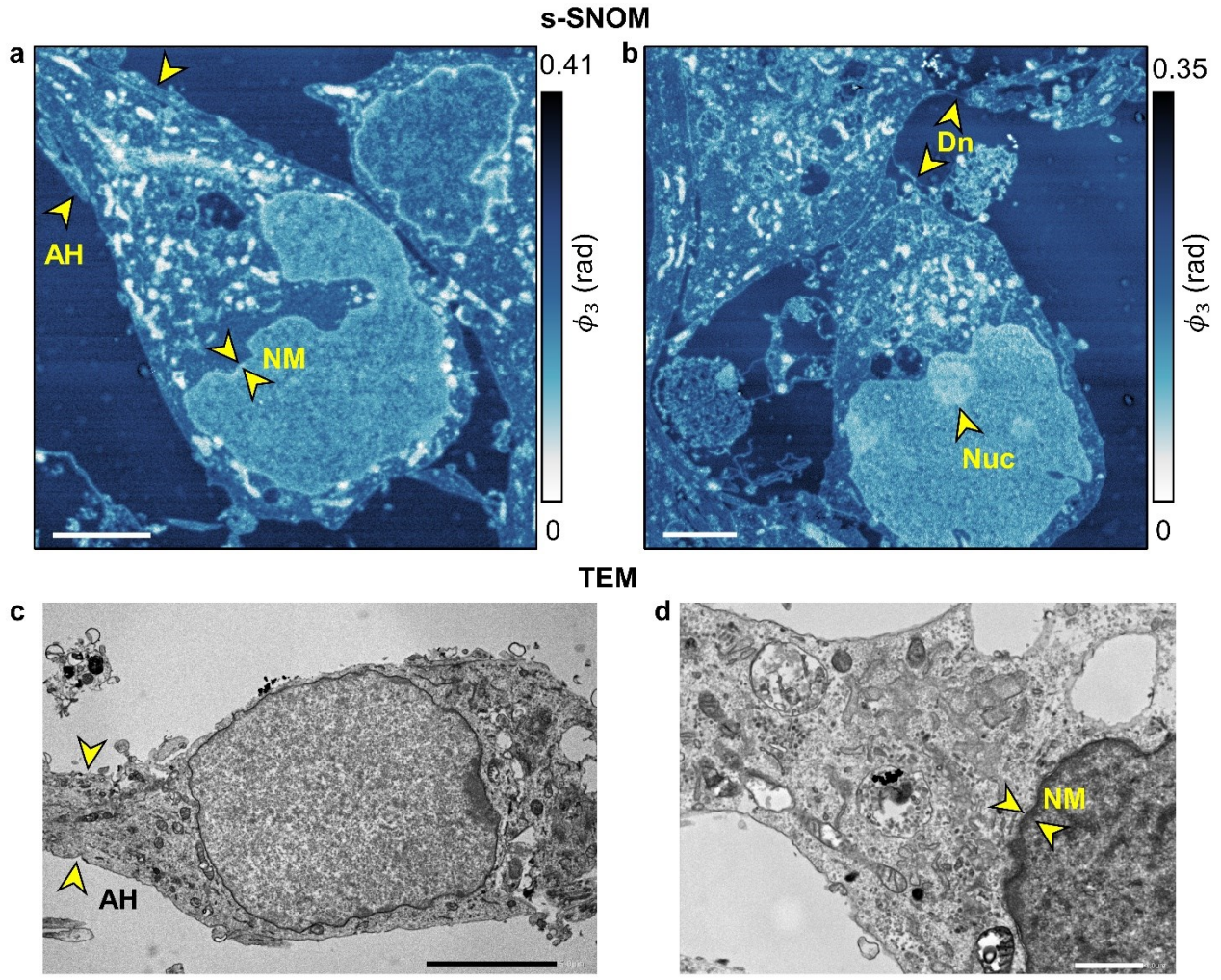

Figure 5.3 s-SNOM and TEM imaging of hippocampal neurons. (a,b) *s-SNOM images of hippocampal neurons acquired at an imaging wavelength of 1740cm^{-1}. The image dimensions are (a) 15µm x 15µm and (b) 20µm x 20µm, both with 20nm pixel size. A pixel integration time of 3ms was used and thus the acquisition time was (a) ~1 hour and (b) 1 hour and 40 minutes. The tapping amplitude was ~51nm for both images.* ***(c,d)*** *TEM images of hippocampal neurons. NM; nuclear membrane, Nuc; nucleolus, AH; axon hillock, Dn; dendrite. Scale bars 3µm (a,b), 5µm (c), 1µm (d).*

contribution to the absorption from the neurons can be seen in the amide I and II absorption bands. Other expected absorption features such as those from nucleic acids are too small to be distinguished from the absorption of the resin. This is attributed to the sections having a large resin content, as well as the area measured with the FTIR spectrometer covering a large amount of resin in the extracellular space.

Figure 5.2 shows s-SNOM images of a neuron acquired at two different imaging wavelengths. Imaging at a wavelength of 1660cm^{-1} (figure 5.2 (a)) excites amide moieties in the cell and allows visualisation of areas with high amide density. The nuclear membrane is identifiable, as well as

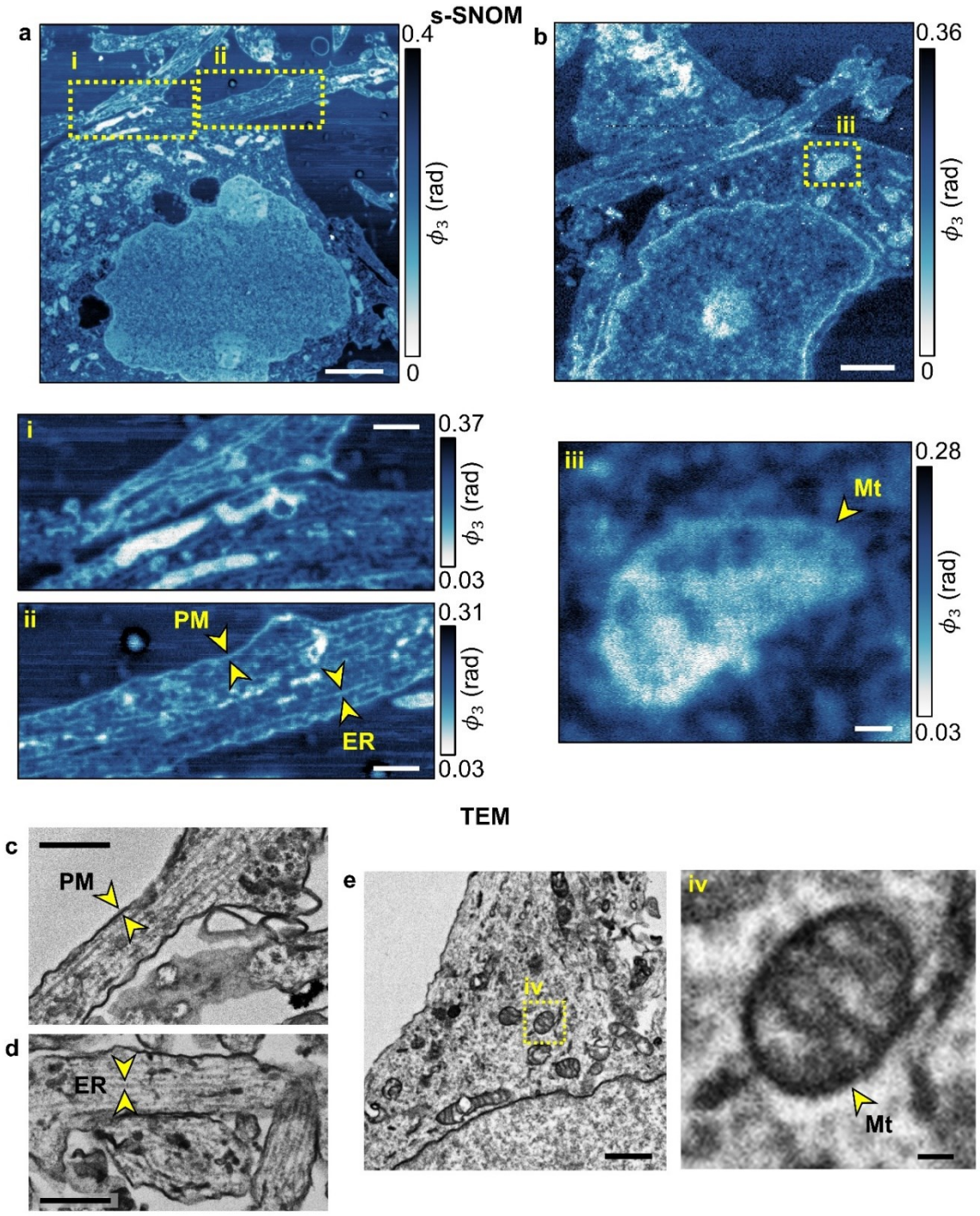

Figure 5.4 High resolution s-SNOM and TEM imaging of hippocampal neurons. (a,b) *s-SNOM images showing neuronal ultrastructure acquired at an imaging wavelength of 1740cm^{-1}. The image dimensions are (a) 12μm x 12μm, (b) 6.6μm x 6.6μm, and (iii) 1μm x 1μm, with 10nm, 25nm and 2nm pixel sizes, respectively. (i) and (ii) are cropped from (a). The pixel integration time was (a) 10ms, (b) 7ms and (iii) 13ms and thus the images took approximately 8 hours, 15 minutes, and 4 hours to acquire, respectively. The tapping amplitude was ~40nm in each case.* ***(c,d,e)*** *TEM images of neuronal ultrastructure. Mt; mitochondria, PM; plasma membrane, ER; endoplasmic reticulum. Scale bars 2μm (a), 1μm (b,e), 500nm (i,ii,c,d), 100nm (iii,iv).*

amide-dense regions in the nucleus (inset i). Amide-dense regions in the cytoplasm are also visible, which are likely to be mitochondria and other organelles such as ribosomes and lysosomes.

Imaging at a wavelength of 1740cm^{-1} (figure 5.2 (b) and inset ii) primarily maps the resin density in the cell, which enables the visualisation of intracellular structures. There might also be contributions from lipids and fixatives, which each contain aldehyde groups which exhibit absorption features at this wavelength [139]. Interestingly, the osmium tetroxide stain that provides much of the contrast in EM also has a sharp absorption peak at this wavelength [188]. Imaging at this wavelength might, therefore, provide a means of correlating s-SNOM with TEM.

The NM exhibits higher contrast and is much more clearly identifiable when imaged at a wavelength of 1740cm^{-1} when compared to an imaging wavelength of 1660cm^{-1}. This might be because the NM is densely packed with lipids [157] and the resin is unable to penetrate it after fixation with OsO_4, leading to a large variation in resin density across the membrane and thus high contrast when imaged at a wavelength of 1740cm^{-1}. On the other hand, the amide-dense region in the nucleoli is more easily identified at 1660cm^{-1} than at 1740cm^{-1}. The low contrast at 1740cm^{-1} is likely to be because the resin density varies less in this area, which is probably due to there being a lower concentration of lipids in less membranous areas of the cell. Thus, it seems that 1660cm^{-1} is the better wavelength for mapping amide groups such as those found in proteins and nucleobases, whilst 1740cm^{-1} is the better wavelength for imaging membranous structures.

Figure 5.3 (a) and (b) are s-SNOM images showing typical neuronal morphology. The protrusion from the cell body is an axon hillock (AH), which connects the cell body to the axon of the neuron. An axon hillock can also be seen in the TEM image (figure 5.3 (c)) with similar morphology, supporting the identification. There are also much smaller protrusions from the cell body which might be dendrites (Dn). These are branch-like structures that receive input from other cells. Dendrites are not seen in this sample of TEM images of neurons, however, so this identification is made with less confidence.

5.3.2 Improved spatial resolution and visualisation of membranous structures with osmicated cells

The s-SNOM images in figure 5.4 (a), (b) and insets (i-iii) show neuronal ultrastructure in high-resolution. Membranous structures such as ER and the internal membranes of mitochondria known

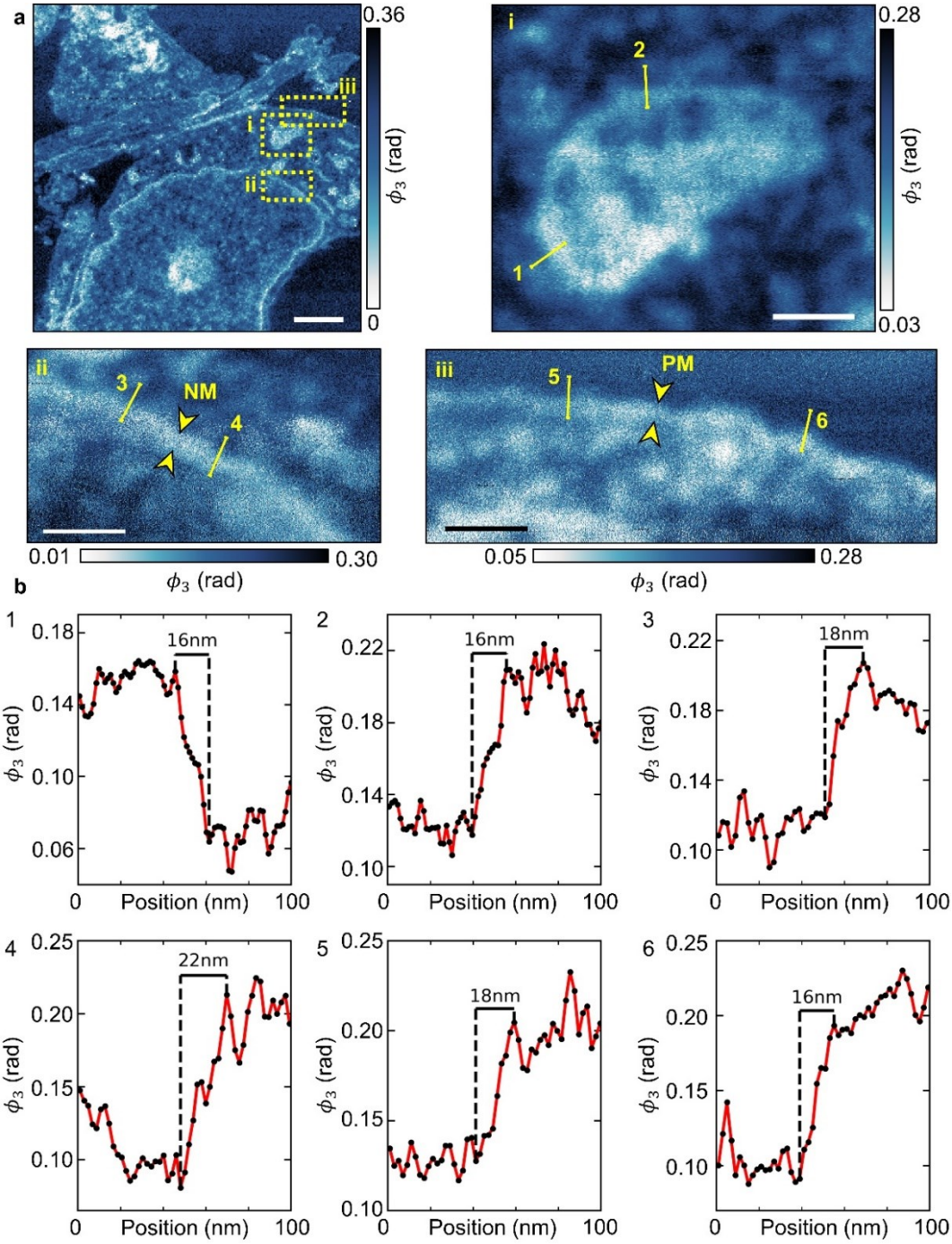

Figure 5.5 Spatial resolution of hippocampal neuron s-SNOM images. (a) *s-SNOM images acquired at 1740cm^{-1}. The image dimensions are (a) 6.6μm x 6.6μm, (i) 1μm x 1μm, (ii) 0.85μm x 0.47μm and (iii) 1.64μm x 0.47μm. The pixel sizes are (a) 25 nm and (i,ii,iii) 2nm. The pixel integration time was (a) 7ms, (i) 13ms and (ii,iii) 3ms. It took approximately 15 minutes, 8 hours, 10 minutes, and 20 minutes to acquire (a),(i),(ii) and (iii), respectively. The tapping amplitude was ~40nm in each case.* ***(b)*** *Spatial profiles (1–6) of the s-SNOM signal for the lines shown in insets i,ii&iii. NM; nuclear membrane, PM; plasma membrane. Scale bars 2μm (a), 200nm (i-iii).*

as cristae are more easily identified here compared to the high-resolution images of myeloma cells in figure 4.5. A plasma membrane (PM) is also identifiable here (figure 5.4 (a) (ii)) but is not identifiable in the s-SNOM images of myeloma cells. These structures are probably better-visualised

due to the osmication of neurons better preserving membranous structures. The TEM images in figure 5.4 (c), (d), (e) and inset iv also show a PM, ER and mitochondrial membranes with similar morphologies to those seen in the s-SNOM images, once again supporting the identifications made.

To quantify the spatial resolution of s-SNOM images of these samples, line profiles were extracted from the images in figure 5.5 (a). To reduce noise, the line profiles were averaged over a width of 2 pixels, equating to 2.6nm in profiles 1 and 2 and 4nm in profiles 3–6. The line profiles in figure 5.5 (b) demonstrate sub 20nm spatial resolution, which is significantly better than the spatial resolution achieved with multiple myeloma cell samples in chapter 4. Again, this might be a result of the neurons being osmicated, providing additional fixation of samples through the fixation of lipids. This could translate to better spatial resolution through better preservation of cells, both chemically and morphologically, leading to sharper boundaries between cell structures.

5.3.3 Simultaneous mapping of cell chemistry and nanoparticle theranostics and characteristic stages of nanoparticle internalisation

Figure 5.6 (a) is an s-SNOM image of an area of a neuron containing AuNPs acquired at an imaging wavelength of 1660cm^{-1}. Rather than mapping the phase, ϕ_3, this image is a map of the amplitude, s_3. The high reflectivity of gold provides a large s-SNOM amplitude signal where AuNPs are located that contrasts strongly against the cell and embedding resin. This enables identification and mapping of AuNPs in the samples (inset i). At this wavelength, the corresponding s-SNOM phase image (figure 5.6 (b)) provides a chemical mapping of amide density. Thus figure 5.6 demonstrates how s-SNOM can be used to simultaneously map NPTs and cell chemistry.

The three AuNPs in figure 5.6 (a) (i) are internalised in a neuron at the edge of a vesicle-like structure, which is typical for the internalised AuNPs observed in these samples. Whilst three AuNPs are seen in this s-SNOM amplitude image, one of the AuNPs is not detectable in the s-SNOM phase image in figure 5.7 (b) (ii). The reason for this is presently unknown, but it might be related to these particular AuNPs being star-shaped, as this phenomenon is not observed for spherical AuNPs.

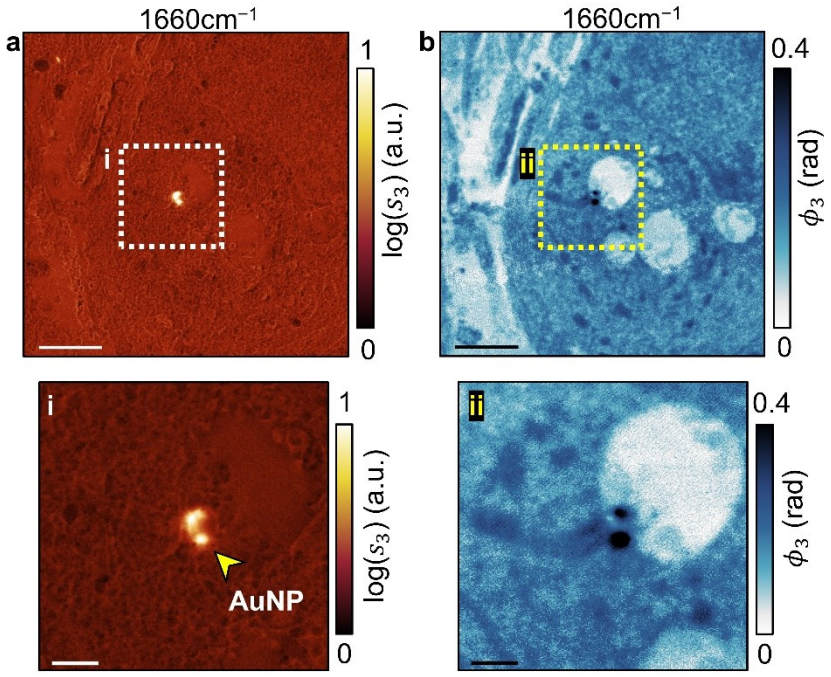

Figure 5.6 Simultaneous mapping of cell chemistry and nanoparticle theranostics. *s-SNOM amplitude (a) and phase (b) images of the same area of a neuron acquired at an imaging wavelength of 1660cm^{-1}. The image dimensions of (a) and (b) are 10μm x 10μm with 10nm pixel size. A pixel integration time of 3ms was used and thus the images took approximately 1 hour and 40 minutes to acquire. The tapping amplitude was ~72nm. Insets i&ii show gold nanoparticles in greater detail. AuNP; gold nanoparticle. Scale bars 2μm (a,b), 500nm (i,ii).*

Figure 5.7 shows s-SNOM and TEM images of (spherical) AuNPs at three characteristic stages of internalisation into neurons [171]. In the first stage (figure 5.7 (a,d,g)), AuNPs are surface associated, meaning they are adjacent to or touching the plasma membrane of a neuron. In the second stage (figure 5.7 (b,e,h)), AuNPs are embedded into the plasma membranes of neurons. This is characterised by a curvature of the membrane around the AuNPs. The membrane continues to curve around the AuNP and eventually reseals with the AuNP internalised [173]. Examples of internalised AuNPs are shown in figure 5.7 (c,f,i).

Figure 5.7 (a-f) are s-SNOM images acquired at an imaging wavelength of 1740cm^{-1}. This wavelength was chosen to maximise the contrast observed for membranous structures, enabling optimum imaging of AuNP interaction with cell membranes. The internalisation of AuNPs could also be imaged at other wavelengths to enable simultaneous mapping of cell chemistry as in figure 5.6 (b). This would provide a significant advantage over using TEM since cell chemistry could be monitored in a label-free way throughout the embedding process.

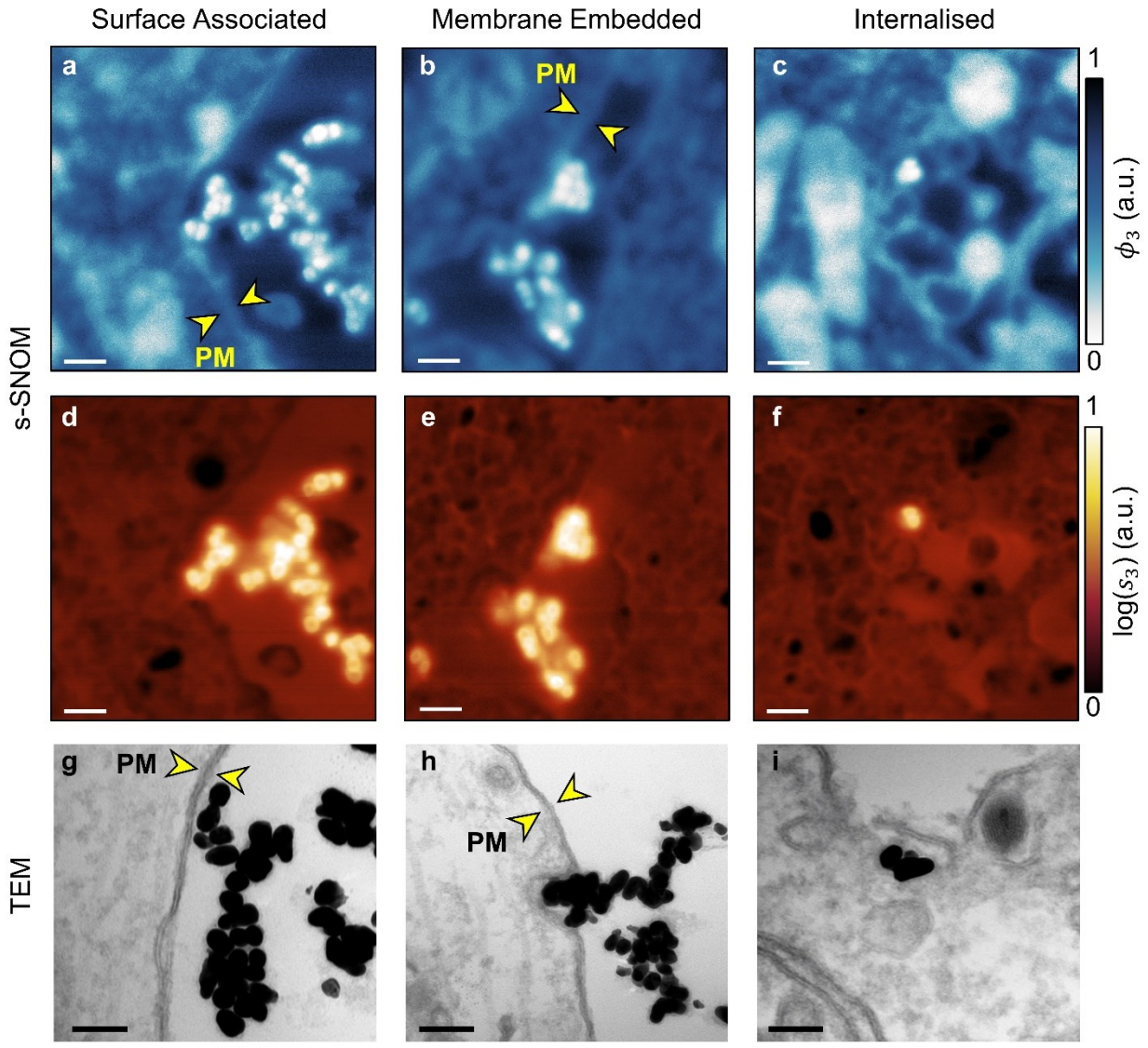

Figure 5.7 Characteristic stages of nanoparticle internalisation. *s-SNOM phase (a,b,c), s-SNOM amplitude (d,e,f) and TEM (g,h,i) images showing three stages of nanoparticle internalisation in hippocampal neurons. The s-SNOM image dimensions are 1.5μm x 1.5μm with 2nm pixel size. A pixel integration time of 7ms was used and thus the images each took approximately 2 hours and 10 minutes to acquire. The tapping amplitude was ~30nm. PM; plasma membrane. Scale bars 200nm (a–f), 100nm (g–i).*

5.4 Conclusions and further work

In this chapter, s-SNOM has been used to image intracellular structures and map the distribution of NPTs in hippocampal neurons. Many intracellular structures have been identified and validated by supporting TEM images of cell sections from the same cell block. Additional fixation with osmium tetroxide enabled better imaging of membranous structures, enabling the identification of the plasma

membrane. Osmication also seemed to improve the achievable spatial resolution, which might be due to the additional fixation of lipids leading to better preservation of structures, both chemically and morphologically.

Simultaneous mapping of NPTs and cell chemistry has also been demonstrated, which might give rise to studying the chemical changes associated with uptake of NPTs and the monitoring of organelle function and health in response to nanomedicines. Also, three characteristic stages of nanoparticle internalisation were identified using s-SNOM, proving s-SNOM as a valuable tool for mapping nanoparticle distribution in cells.

In addition to monitoring the changes in cell and organelle chemistry associated with nanomedicine treatment, relevant further work might involve studying the dynamics of how drugs and therapeutics are released from NPTs as they internalise into cells. This might begin by exploiting a spectral feature of a drug to distinguish NPTs carrying drug loads from those that are not. This could then be extended to quantifying the nanoparticle load, which would enable studying the dynamics and intracellular locations of drug release.

Chapter 6

Mapping mesoporous silica nanoparticles in whole malignant glioma cells

6.1 Mesoporous silica as a non-toxic nanoparticle theranostic

Whilst nanoparticle theranostics are commonly made of gold, there are concerns over its use in vivo due to its potential toxicity [189]. Of primary concern is the lack of understanding surrounding the accumulation and excretion of AuNPs from the body [190], with AuNPs posing a risk of blocking blood flow [189].

A number of NPTs based on non-toxic materials have been developed to combat this issue [189]. Amongst these materials are mesoporous silica nanoparticles (MSNs) [191, 192]; that is, silica nanoparticles containing nanometre-sized spherical voids (pores). MSNs are non-toxic, biodegradable and approved by the FDA for use in humans [193-198]. They are promising due to their large surface areas and tuneable pore sizes, which allow them to carry large drug-loads [199,

200]. As an example of their use, MSNs were shown to be more effective than their dense nanoparticle counterparts in a study concerning bone regeneration [201].

MSNs have an electron density that is sufficient for them to be imaged in cells using TEM [202]. They can also be functionalised with the fluorophore fluorescein isothiocyanate (FITC) for imaging with fluorescence techniques [170]. As with the gold-based NPTs in chapter 5, the challenge when imaging MSNs is to simultaneously map the cell chemistry to study changes in biochemistry in individual cell components, and to do this in a label-free way. As seen thus far, s-SNOM is well suited to this challenge.

6.2 Malignant glioma cell morphology and research questions

In this chapter, s-SNOM imaging is performed on malignant glioma cells from the U-87 MG cell line. Research questions concerning U-87 MG cells are often on the whole-cell level and they concern aspects such as cell migration and invasiveness. Examples include migration inhibition with the application of flavonoids [203], as well as cell-cell transfer of organelles through tunnelling nanotubes [204]. Often key to this research is obtaining morphological and chemical information of nanoscale cell components such as lamellipodia and filopodia [203], the structures that constitute the peripheries of cells, which makes s-SNOM a highly applicable technique.

As well as being biologically relevant, whole cell imaging (rather than sections of cells) is an exciting yet relatively unexplored area for s-SNOM. The main difficulty is that s-SNOM is a highly surface sensitive technique, meaning the contribution to the signal from a volume element decays rapidly with depth into the sample. As such, images of whole cells have a large contribution from the ~10nm cell membrane and imaging is generally limited to surface features. s-SNOM has been used for imaging amyloid β-sheets on the surface of neurons without requiring immunolabelling [113], as well as imaging the surface of red blood cells [114].

There is still a contribution to the s-SNOM signal from components below the surface [205], however, and it is possible to identify these components with chemical sensitivity [123]. This is exploited here in the form of imaging MSNs embedded and internalised in cells. s-SNOM also has the advantage

of delivering topographical information, allowing three-dimensional surface morphology of cell components such as lamellipodia and filopodia to be obtained. The results presented in this chapter focus on these two aspects of whole-cell imaging with s-SNOM.

6.3 Preparing MSN-treated U-87 MG cells for s-SNOM imaging

6.3.1 MSN synthesis

MSN synthesis was performed using a modified version of a type of sol-gel process known as a Stöber process [206]. Briefly, a colloidal suspension of a precursor ('sol') is transformed through chemical reaction into a solid and liquid mixture ('gel'), from which the solid part is isolated through evaporation of the liquid solvent. The resulting material can range from uniformly sized discrete nanoparticles (for example the MSNs used here) to the ultra-lightweight and thermally insulating materials known as aerogels. The MSNs are made mesoporous (pore diameters between 2nm and 50nm) by letting the nanoparticle structures grow around near-spherical surfactant aggregates which are later removed, leaving voids (pores) [207].

The process for producing MSNs was as follows (performed by Dr. Alessandra Pinna, Imperial College, adapted from [170]):

1. The surfactant-based template for producing pores was prepared by adding 1g of cetyltrimethylammonium bromide (CTAB) to 500ml of distilled water.
2. The pore template, contained in a flask, was immersed in paraffin oil at 70°C and stirred at 600rpm using a magnetic hotplate stirrer, followed by the addition of 3ml of 2 M sodium hydroxide (NaOH) catalyst.
3. The silica-based precursor, tetraethyl orthosilicate (TEOS), was added to the pore template solution, followed by 5ml of ethyl acetate (EtOAc).
4. The solution was aged at 70°C for 1 hour with stirring (600rpm) and 3 hours without stirring to allow formation of nanoparticles.

5. The solution was washed with ethanol three times and centrifuged for 40 min at 7830rpm.
6. Nanoparticles were isolated by drying the solution overnight at 60°C.
7. The CTAB surfactant aggregates were eliminated by heating in a 550°C furnace for 6 hours, leaving voids (pores) in the nanoparticles.
8. The diameter (d=(80±10)nm) and sphericity of MSNs was confirmed using TEM [170].

6.3.2 U-87 MG preparation and treatment with MSNs

U-87 MG cells were grown and treated with MSNs as follows (performed by Dr. Darya Kiryushko, Imperial College):

1. U-87 MG cells from the American Type Culture Collection (ATCC), provided by Dr. Jonny Taylor, Imperial College London, were grown on a silicon substrate in RPMI 1640 medium supplemented with 10% FBS, penicillin (100 U/mL), and streptomycin (100 µg/mL). All experiments were performed between passages 10 and 20 i.e. harvested and reseeded into daughter cultures between 10 and 20 times.
2. Cells were incubated with 50µg/ml of MSNs for 24 hours.
3. Cells were fixed with 2.5% glutaraldehyde and 2.5% paraformaldehyde in 0.1M HEPES for 30 minutes at room temperature.
4. Fixatives were removed and cells were rinsed three times in 0.1M HEPES.
5. Cells were dehydrated in a series of graded ethanol (EtOH) (12.5%, 25%, 50% and 70% for 5 mins each, 95% and 100% for 2 x 5 mins each).
6. Cells were further dehydrated in hexamethyldisilazane (HMDS) (HMDS:EtOH 1:1 for 10 mins, HMDS 2 x 10 mins).
7. HMDS was removed and cells were left to air dry in a desiccator at room temperature.

U-87 MG cells prepared as described are shown in figure 6.1. The image was acquired with the built-in optical microscope in the s-SNOM system which has a magnification of 20x.

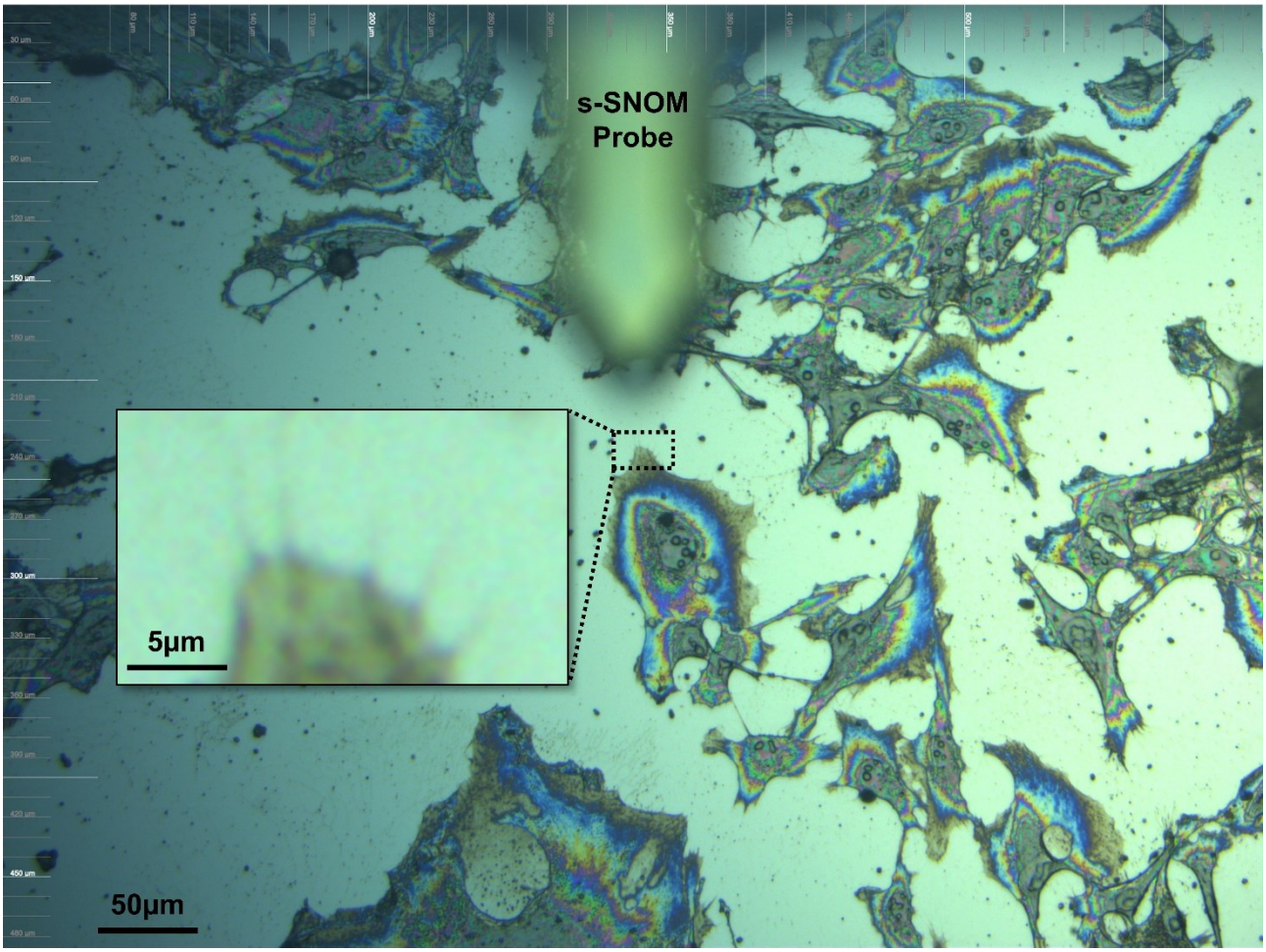

Figure 6.1 Optical microscope image of U-87 MG cells. *U-87 MG cells imaged at 20x magnification using the built-in optical microscope in the s-SNOM system. Cells were prepared using the protocol described in section 6.3.2. Inset shows a region of a cell chosen for imaging with s-SNOM.*

6.3.3 s-SNOM imaging of MSN-treated U-87 MG cells

s-SNOM imaging was performed with the setup described in section 4.2.2 using a tapping amplitude of approximately 50nm. U-87 MG cells are significantly larger (~50–100µm) than the multiple myeloma cells and hippocampal neurons (~10µm) investigated in chapters 4 and 5 respectively. The cell height is typically much greater than the ~3µm travel range of the piezoelectric sample stage on the s-SNOM system and, therefore, it was not possible to capture a whole cell in one image. Imaging was instead focused on the lamellipodia and filopodia at the peripheries of the cells. These regions were chosen since, as discussed, they are the focus of many research questions related to cell movement, cancer migration and cell-cell transfer [203, 204, 208].

6.4 Results and discussion

The results presented in this chapter begin with s-SNOM imaging of the periphery of a U-87 MG cell, including nanoscale chemical and topographical mapping of lamellipodia and filopodia. Following this, the IR chemical signature of MSNs is used to map their distribution in a U-87 MG cell, and the chemical and topographical mappings are used to determine the embedding status of the MSNs. Finally, a morphological erosion algorithm (MEA) is used to account for the broadening of image features due to the limited sharpness of the tip. This is shown to be necessary to accurately image the MSNs, and it is argued that it is also essential for accurately measuring lamellipodia and filopodia morphology.

6.4.1 Imaging whole U-87 malignant glioma cells with s-SNOM

Figure 6.2 (a) shows the topography of the periphery of a U-87 MG cell and reveals a thin (~100nm thick), sheet-like region, which is identified as the lamellipodium [209]. There are also finger-like structures that originate inside the lamellipodium and protrude outwards from it, which are identified as filopodia [210]. This is the first time these structures have been directly optically imaged (that is, without stains and labels) at this level of spatial resolution. Figure 6.2 (c) is an image of approximately the same region of the cell acquired with the built-in microscope in the s-SNOM system (20x magnification). Much of the detail in the filopodia structure is not identifiable in this image, including many of the smaller branches from the main protrusions from the cell. This motivates the use of nanoscale imaging techniques such as s-SNOM for investigating research questions relating to filopodia.

Figure 6.2 (b) is an s-SNOM image of the same region of the cell acquired at an imaging wavelength of 1667cm^{-1}, thus mapping the amide density in this region. Filopodia appear darker than the rest of the cell in the mapping. This is most likely because filopodia contain actin filaments that are bundled together by actin-bundling proteins [211] and thus have a large protein component. However, it is important to note that the increased s-SNOM signal could also be related to the topography, since a change in sample thickness can affect the s-SNOM signal. Indeed, when the phase, ϕ_3, is plot

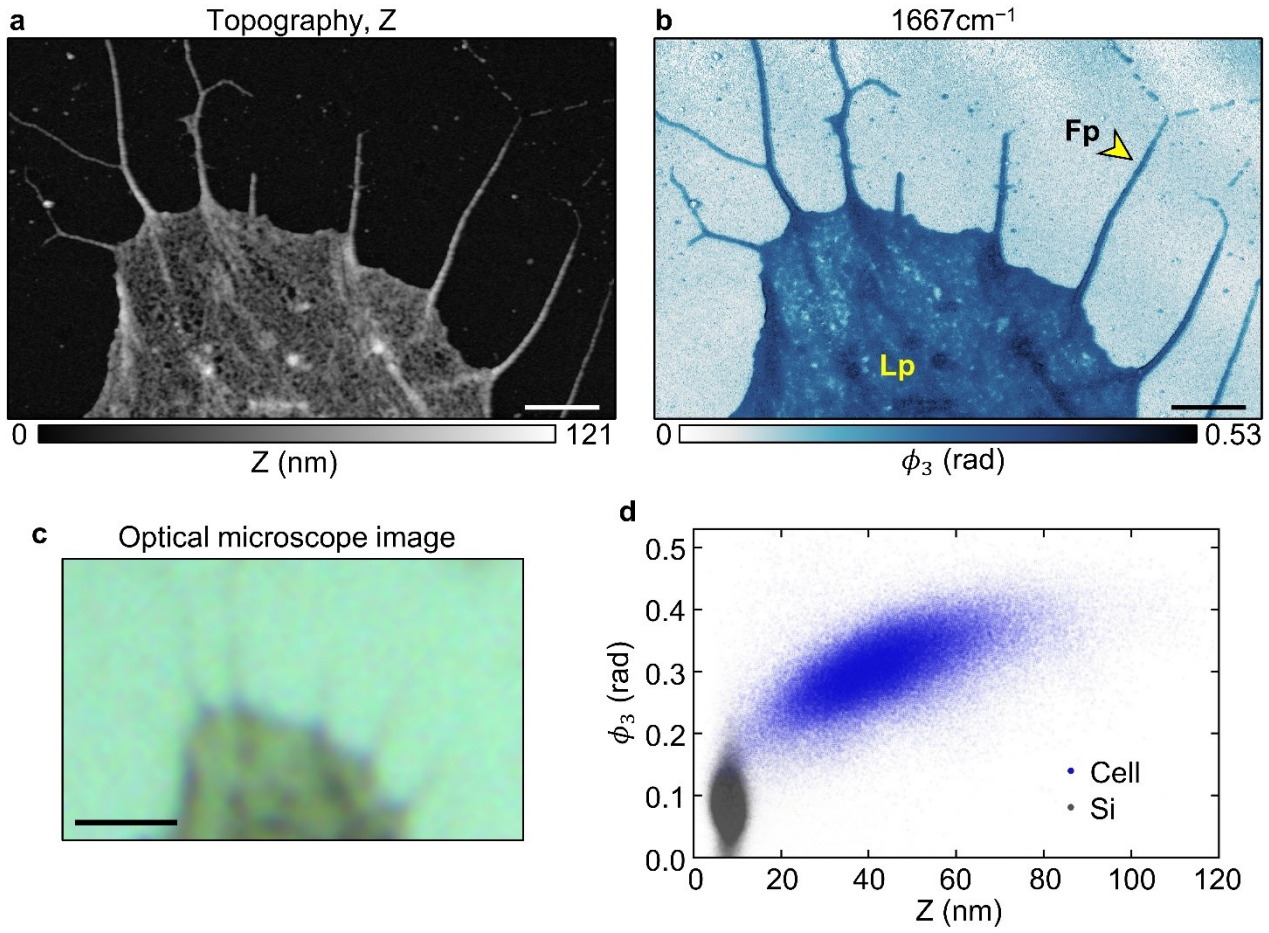

Figure 6.2 s-SNOM imaging of U-87 MG cells. (a) *Topography of a region at the periphery of a U-87 MG cell.* ***(b)*** *s-SNOM image of the same region acquired at an imaging wavelength of 1667cm^{-1}. The s-SNOM (and AFM) image dimensions are 16µm x 10µm with 15nm pixel size. A pixel integration time of 3ms was used and thus the images took approximately 1 hour and 10 minutes to acquire. The tapping amplitude was ~69nm.* ***(c)*** *Corresponding region imaged with the built-in microscope in the s-SNOM system.* ***(d)*** *Correlation between the s-SNOM phase and the sample height using the values at each pixel in the images. The cell and the substrate were split by masking images. Fp; filopodia, Lp; lamellipodium. Scale bars 2µm (a,b), 5µm (c).*

against the cell height, *Z*, for each pixel (figure 6.2 (d)), the two are correlated. This is a different result to the result obtained with the same analysis performed on the myeloma cell sections in figure 3.5 (e), in which there are distinct regions in the phase-Z plot corresponding to different regions of the cell. Thus, the s-SNOM image in figure 6.2 (b) is dependent on the cell topography, not just the chemistry. Consequently, it is important to also take the topography into account when imaging whole cells, specifically when comparing chemical mappings in different cell regions.

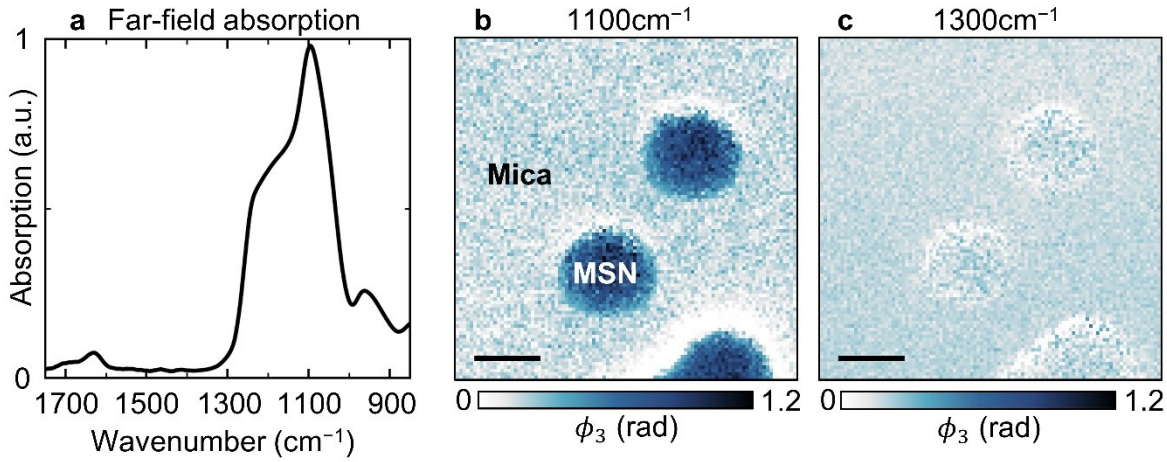

Figure 6.3 Far-field absorption spectrum and s-SNOM images of MSNs. (a) *Absorption spectra of mesoporous silica nanoparticles (MSNs) deposited on a zinc selenide substrate and measured with an FTIR spectrometer in transmission mode.* ***(b,c)*** *s-SNOM images of MSNs on a mica substrate acquired at imaging wavelengths of 1100cm^{-1} and 1300cm^{-1} respectively. The image dimensions are 0.5µm x 0.5µm with 5nm pixel size. A pixel integration time of 13ms was used and thus the images each took approximately 4 minutes to acquire. The tapping amplitude was ~72nm. Scale bars 100nm.*

6.4.2 Detecting silica nanoparticles in cells with chemical sensitivity

Figure 6.3 (a) is a far-field absorption spectrum of MSNs, acquired by dropcasting MSNs onto a ZnSe substrate and using an FTIR spectrometer in transmission mode. A ZnSe substrate was used for its high transmittance in the spectral region required, shown in figure 4.3. The absorption spectrum shows an absorption peak at approximately 1100cm^{-1}. Absorption exhibited by MSNs at this wavelength has previously been reported and is due to Si–O–Si stretching [212, 213]. This absorption feature serves as a means of detecting MSNs with chemical sensitivity using s-SNOM, providing that s-SNOM is sensitive to the level of absorption exhibited by single particles.

To demonstrate chemically specific detection of MSNs, the particles were dropcast on a mica substrate and imaged with s-SNOM. A mica substrate was used since the MSNs were not stable on a silicon substrate and were pushed around by the imaging probe. Mica has an absorption feature at approximately 1000cm^{-1} [214] (also Si–O–Si stretching) which means the absorption exhibited by the substrate might be slightly higher at 1100cm^{-1} than at 1300cm^{-1}. Despite this, the MSNs still exhibit large contrast against the substrate at 1100cm^{-1} (figure 6.3 (b)), but very little at 1300cm^{-1} (figure 6.3 (c)), confirming the ability to image them with chemical sensitivity using s-SNOM.

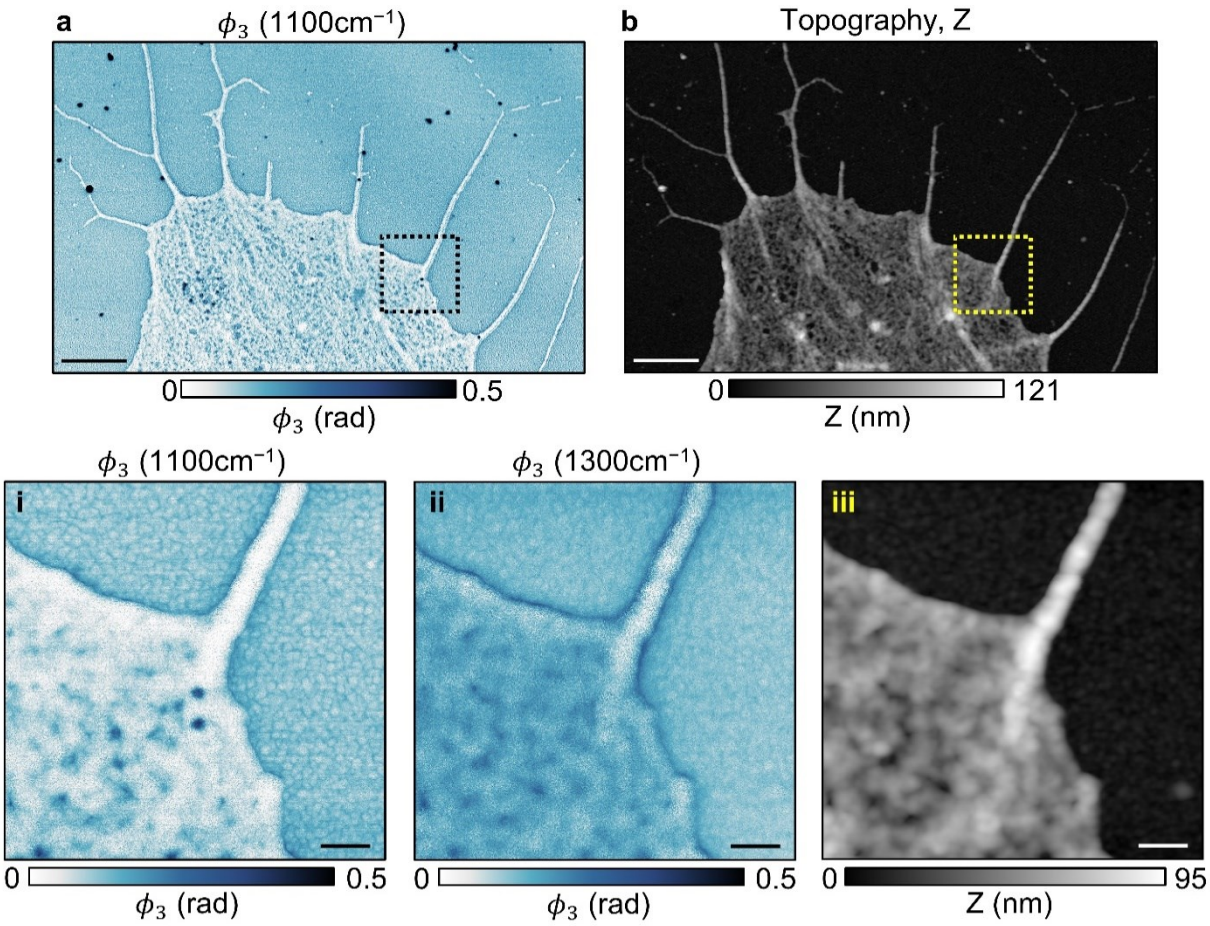

Figure 6.4 Detecting MSNs in U-87 MG cells with s-SNOM. (a) *s-SNOM image of a region of a U-87 MG cell acquired at an imaging wavelength of 1100cm^{-1}.* ***(b)*** *Topography of the same cell region. Insets i–iii show a region of the cell that contains mesoporous silica nanoparticles (MSNs). Inset i is acquired at 1100cm^{-1}, where MSNs absorb strongly. Inset ii is acquired at 1300cm^{-1}, where MSNs absorb weakly. Inset iii shows the topography of this region. The image dimensions are 16μm x 10μm with 15nm pixel size for (a,b) and 2.25μm x 2.25μm with 5nm pixel size for (i,ii,iii). A pixel integration time of 3ms was used and thus images (a,b) took approximately 1 hour and 10 minutes to acquire and images (i,ii,iii) took approximately 1 hour to acquire at each wavelength. The tapping amplitude was ~72nm for (a,b) and 45nm for (i,ii,iii). The change in tapping amplitude was due to the imaging probe being replaced between scans. Scale bars 2μm (a,b), 300nm (i–iii).*

Figure 6.4 shows s-SNOM images of the region of the U-87 MG cell imaged in figure 6.2 acquired at imaging wavelengths of 1100cm^{-1} and 1300cm^{-1} to facilitate the detection of MSNs. The image shown in figure 6.4 (a) inset (i), acquired at 1100cm^{-1}, shows two strongly absorbing particle-like features whose diameters are consistent with the ~80nm MSN diameter independently measured with TEM [170]. In the image acquired at 1300cm^{-1} (inset ii), where the MSNs exhibit little absorption, the particles are indistinguishable from the cell. These two images are consistent with the absorption feature of the MSNs at 1100cm^{-1}, so these particle-like features are therefore identified as MSNs.

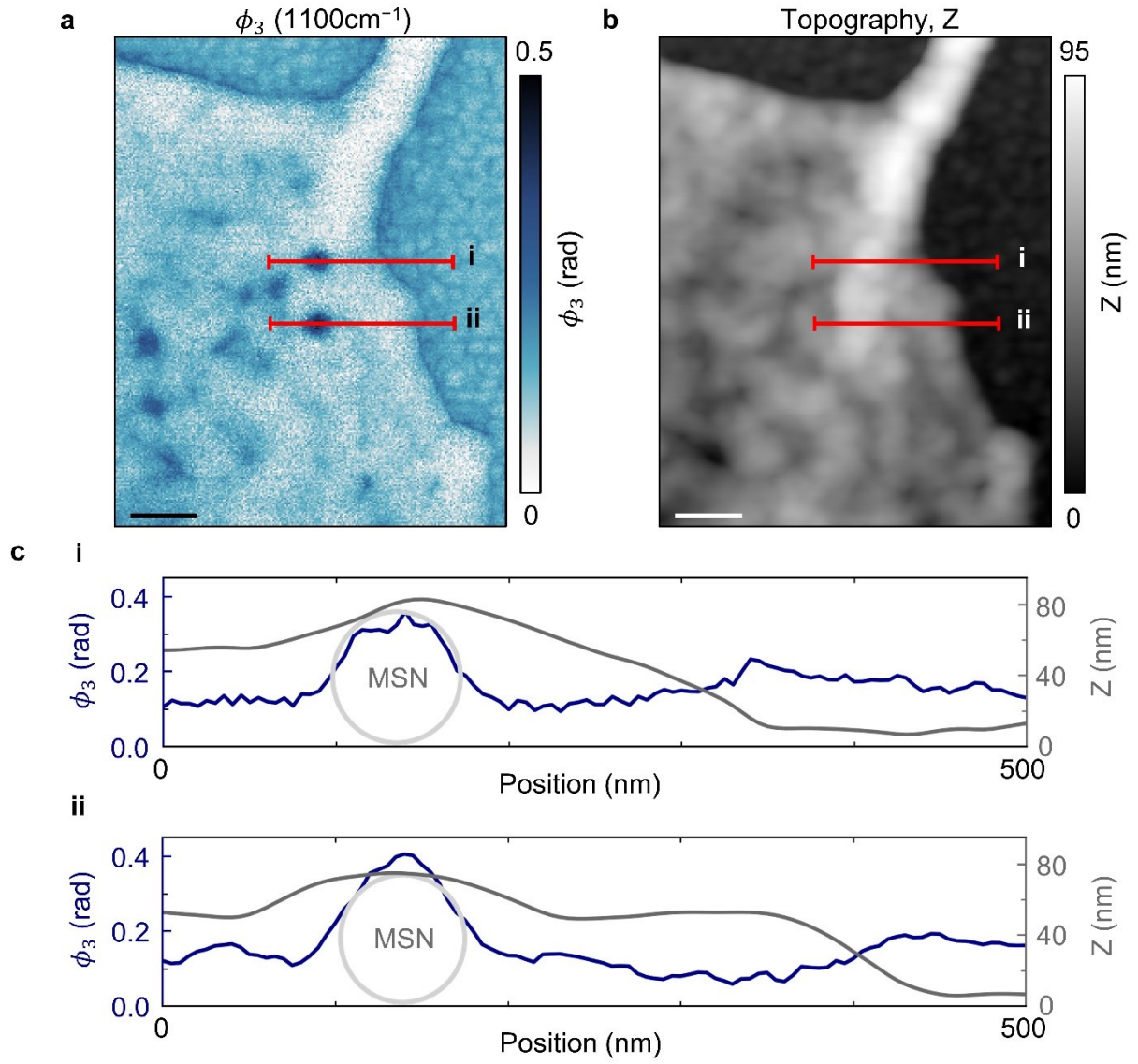

Figure 6.5 Determining the embedding status of internalised MSNs using topography measurements. (a) *s-SNOM image of a region of a U-87 malignant glioma cell containing two mesoporous silica nanoparticles (MSNs).* ***(b)*** *Topography in the same region. The image dimensions are 1.13μm x 1.42μm with 5nm pixel size. A pixel integration time of 3ms was used and thus images (a,b) took approximately 6 minutes to acquire. The tapping amplitude was ~45nm.* ***(c)*** *Spatial profiles of the s-SNOM signal and topography along lines i&ii which cross MSNs and the edge of the cell. Profiles were constructed by averaging over a width of 5 pixels (25nm). MSNs (d~80nm) shown for scale. Scale bars 200nm.*

Crucially, the MSNs are mapped without modification and in cells that are free of stains and labels. This is a key advantage of using s-SNOM compared to fluorescence techniques, which would require both the MSNs and the cells to be fluorescently labelled. Once again, this would pose the risk of perturbing the function of NPTs and the sample biology, as well as potentially missing out on important information due to lack of appropriate labelling. The distribution of MSNs could also be mapped using a technique such as SEM if a conductive coating is first applied to the cells. In this

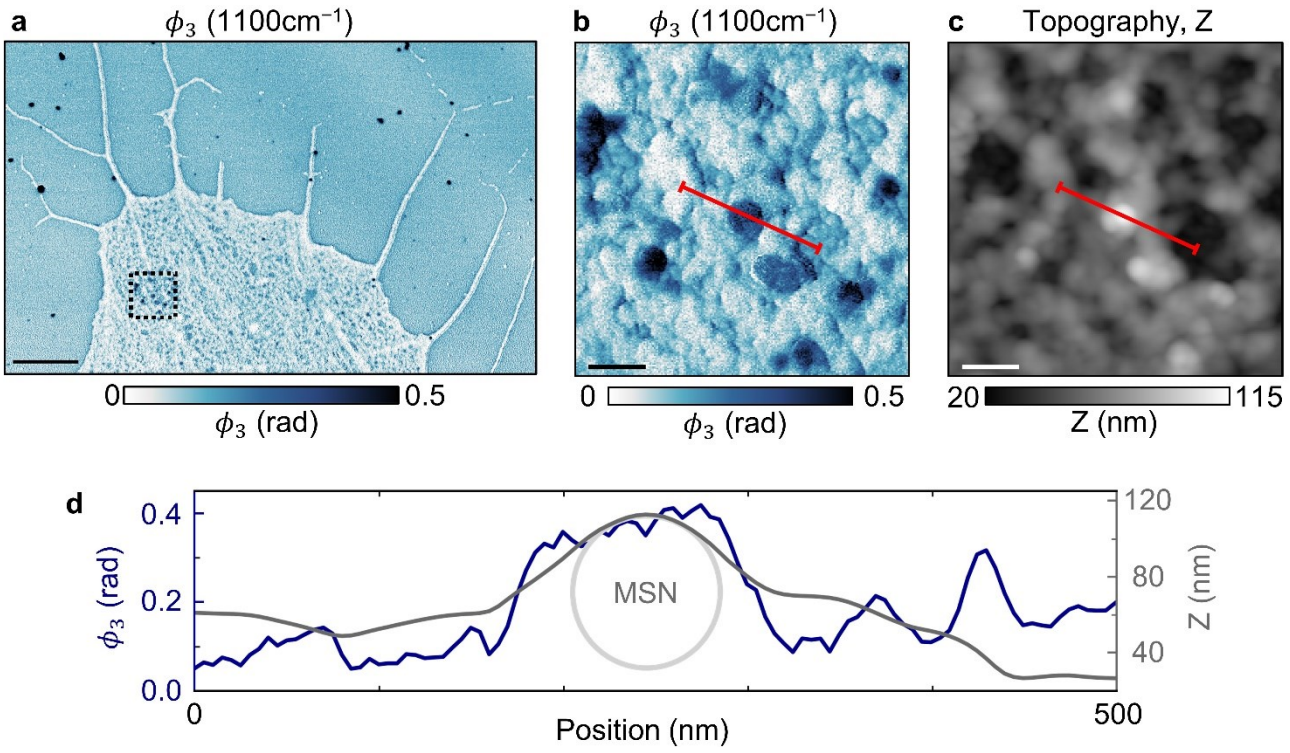

Figure 6.6 Determining the embedding status of embedded MSNs using topography measurements. (a) *s-SNOM image of a U-87 malignant glioma cell.* ***(b)*** *s-SNOM image of a region of the cell containing mesoporous silica nanoparticles (MSNs).* ***(c)*** *Topography in the same region. The image dimensions are 16μm x 10μm with 15nm pixel size for (a) and 1.13μm x 1.13μm with 5nm pixel size for (b,c). A pixel integration time of 3ms was used and thus (a) took approximately 1 hour and 10 minutes to acquire and images (b,c) took approximately 5 minutes to acquire. The tapping amplitude was ~72nm.* ***(d)*** *Spatial profiles of the s-SNOM signal and topography along the red line across an MSN. The profile was constructed by averaging over a width of 5 pixels (25nm). MSN (d~80nm) shown for scale. Scale bars 2μm (a), 200nm (b,c).*

case, the advantage of using s-SNOM is the ability to chemically map structures on the cell surface, and potentially detect biochemical changes induced by the application of MSNs or other NPTs.

6.4.3 Determining the embedding status of MSNs based on topography

Another key advantage of using s-SNOM, compared to EM or fluorescence techniques, is that topographical information is obtained by default rather than applying special 3D imaging techniques [215, 216]. Here it is shown that this topographical information can be used to confirm the embedding status of MSNs.

An example of using topography to determine the embedding status of MSNs is shown in figure 6.5. Spatial profiles of the s-SNOM signal and the topography along the lines passing through MSNs (i &

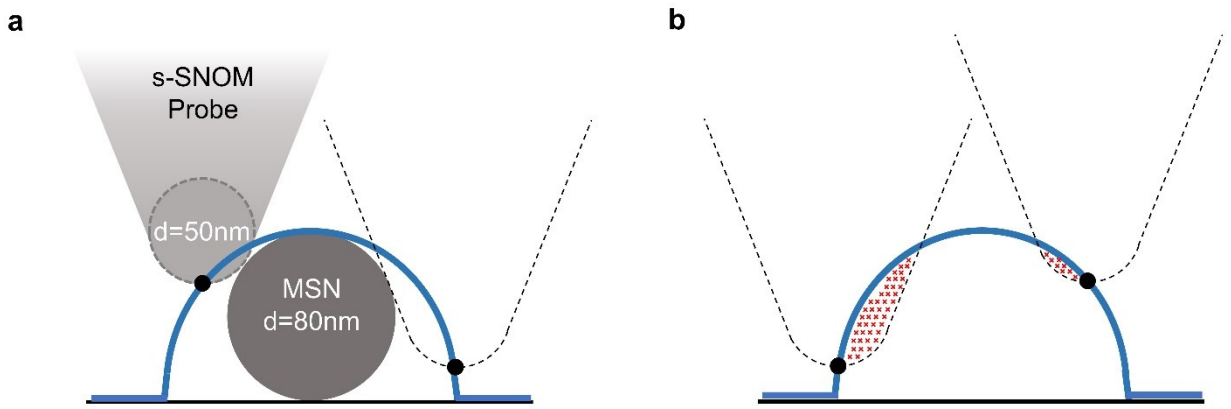

Figure 6.7 A 2D representation of the broadening of objects in topography images and a means of mitigation based on morphological erosion. (a) *The geometry of the tip of the s-SNOM probe means that objects (e.g. mesoporous silica nanoparticles (MSNs)) can appear larger than they are when measured (blue trace).* ***(b)*** *In post analysis, a model of the tip is placed at each point on the blue trace. The sample cannot occupy the red hashed regions because they are occupied by the tip during imaging. The red hashed regions (and similar regions constructed for all points on the blue trace) can therefore be removed from the image.*

ii) shown in figure 6.5 (a) and (b) are plot in figure 6.5 (c). The spatial profiles show that the topography does not follow the curvature of the MSNs. This might mean that the MSNs are fully embedded in the cell and perhaps even internalised, that is, the MSNs are covered by the cell membrane.

Figure 6.6 shows an example of an MSN that is not fully embedded into the cell. Figure 6.6 (d) shows that the topography along the red line shown in figure 6.6 (b) and (c) follows a curvature that is consistent with the MSN diameter. This suggests that the MSN is not fully embedded, but rather is exposed. The profile of the s-SNOM signal also shows a larger region exhibiting high absorption compared to the embedded MSNs. This might be more evidence to suggest that the MSN is exposed, rather than being covered by the cell membrane.

6.4.4 Correcting topography with a morphological erosion algorithm

Since imaging probes are not infinitely sharp, objects appear larger in topography images than they really are, leading to overestimates of their size. This is more noticeable for smaller objects that are comparable in size with the tip dimensions, such as MSNs. Figure 6.7 (a) is a two-dimensional representation of how a spherical particle appears larger when measured. The blue line is the path

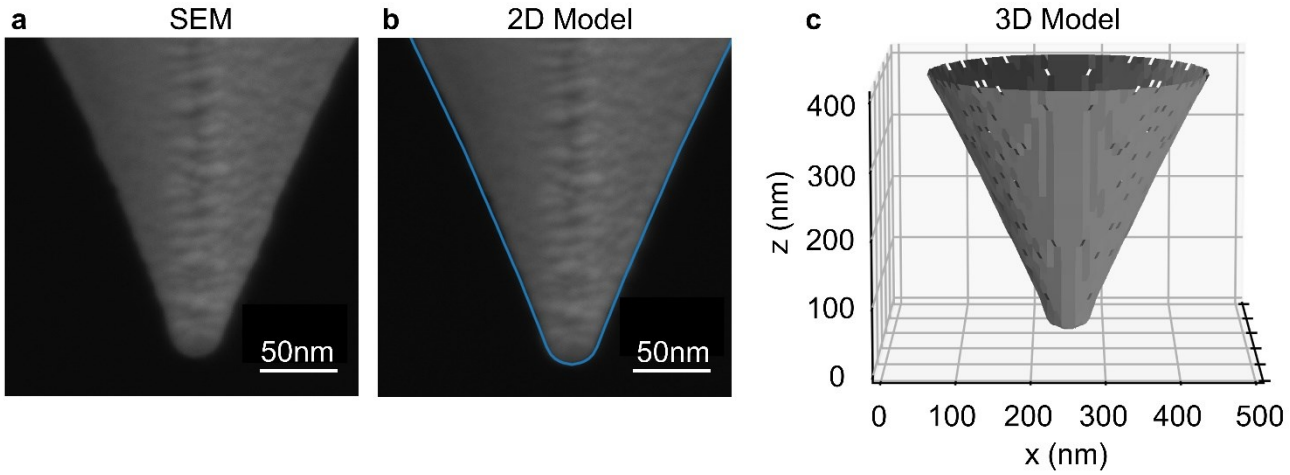

Figure 6.8 An s-SNOM probe imaged with SEM and modelled in 2D and 3D. (a) *An SEM image of the tip of the s-SNOM probe.* ***(b)*** *A two-dimensional model of the s-SNOM probe is constructed by tracing the outline of the probe in the SEM image.* ***(c)*** *A three-dimensional model of the s-SNOM probe is constructed by revolving the 2D model about the long axis of the probe.*

that the tip apex traces as the tip travels over the sphere, that is, the topography measured by the AFM system. Broadening occurs when the contact point between the tip and the sample is not at the apex of the tip, but rather moves round the tip towards the shaft. The radius of curvature of the tip, the aspect ratio of the shaft of the probe and the geometry of the object itself are all important in determining how much an object is broadened by.

Deconvolution algorithms can be applied to images to mitigate some of this broadening to reproduce the sample geometry more faithfully [217]. This is not uncommon in AFM applications, but (as far as the author is aware) it has never been applied to s-SNOM images, despite it being critical in some cases to obtain accurate sample morphology. Here, a morphological erosion algorithm (MEA) is used [218]. In this algorithm, a model of the tip is placed at a pixel in the image such that the tip apex coincides with the image surface. Two such locations are shown in 2D in figure 6.7 (b). Regions where the tip intersects with the image (such as the red hashed areas in figure 6.7 (b)) are removed from the image space. This is done on the basis that the tip must have occupied this space during imaging, so the sample cannot exist there. This is repeated for each pixel in the image.

A model of the tip is therefore required in order to apply an MEA to images. To this end, an s-SNOM probe was imaged using SEM (by Dr. Darya Kiryushko, Imperial College) to obtain the tip morphology (figure 6.8 (a)). A two-dimensional profile of the outline of the tip was created (figure 6.8

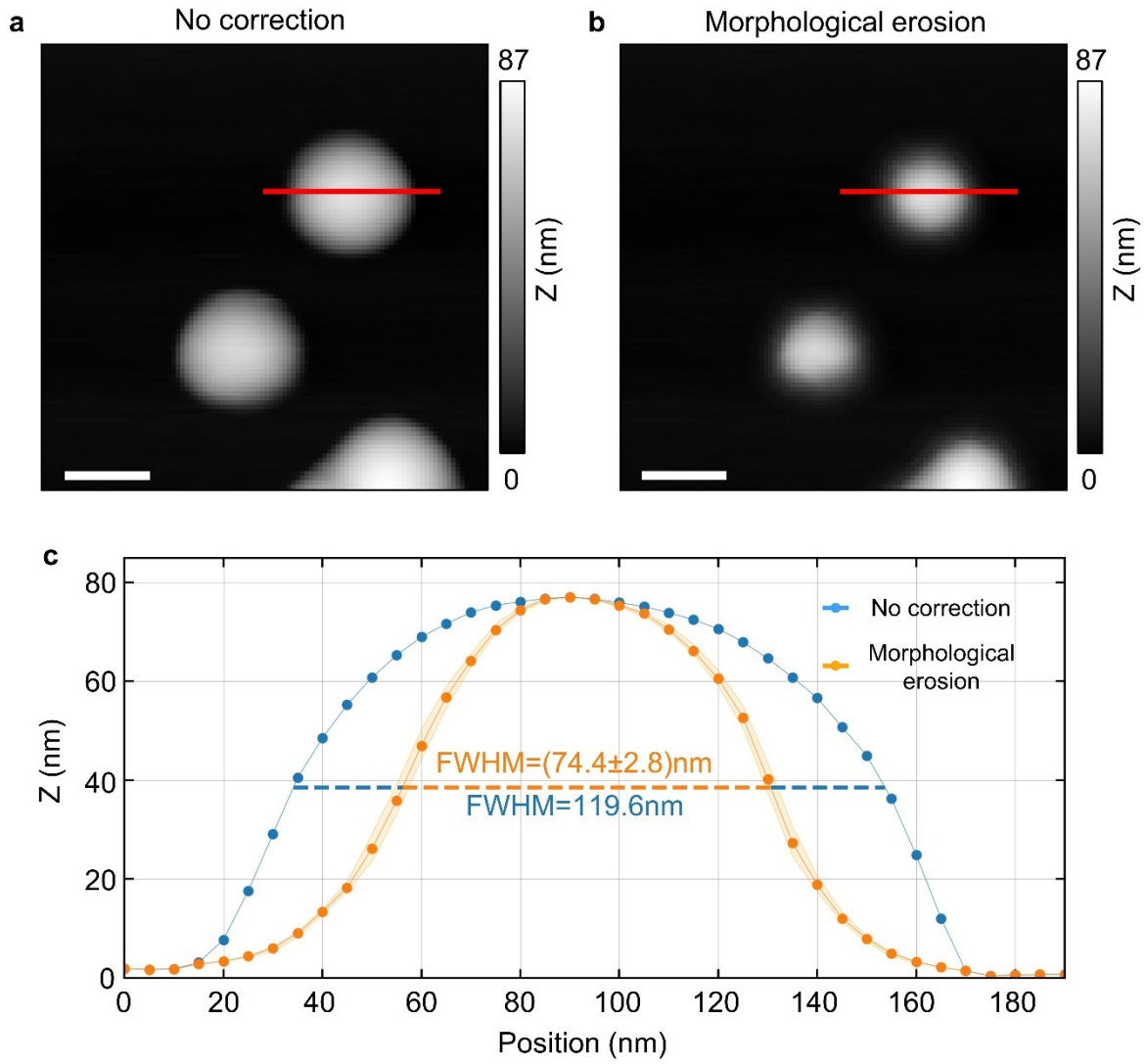

Figure 6.9 Correcting MSN topography using a morphological erosion algorithm. (a,b) *Topography of mesoporous silica nanoparticles (MSNs) deposited on a mica substrate before (a) and after (b) correction with a morphological erosion algorithm (MEA). The image dimensions are 0.5µm x 0.5µm with 5nm pixel size. A pixel integration time of 13ms was used and thus the image took approximately 4 minutes to acquire. The tapping amplitude was ~72nm.* ***(c)*** *Spatial profiles of topography along the red lines in (a) and (b). Profiles are 1 pixel (5nm) wide. The error in the corrected profile is a result of performing the MEA with three different tip radii (26nm, 28nm and 30nm). Scale bars 100nm.*

(b)) and was revolved around the tip axis to create a three-dimensional model (figure 6.8 (c)). Whilst the probe is pyramidal in shape, the sharpening process results in it becoming more radially symmetric towards the tip, thus supporting this radially symmetric model. The tip isn't perfectly resolved in SEM, which gives rise to uncertainty in the radius of curvature of the tip used in the model. Radii between 26nm and 30nm produced models that fit the SEM image of the tip. To account for the uncertainty in the tip geometry, the morphological erosion algorithm is performed using radii

of 26nm, 28nm and 30nm and the resulting images are averaged by taking the mean value of the topography at each pixel.

The MEA was first applied to the image of MSNs on a mica substrate (figure 6.3). Figure 6.9 (a) shows the topography before processing with the morphological erosion. The spatial profile of the topography along a line through the centre of the MSN is shown in figure 6.9 (c) (blue line). The full-width half-maximum (FWHM) of the trace – used as an estimate of the MSN diameter – is 119.6nm, which is approximately 50% larger than the (80±10)nm measured with TEM [170].

Figure 6.9 (b) shows the topography after processing with the MEA. The spatial profile of the topography along the same line through the centre of the MSN is shown in figure 6.9 (c) (orange line). The shading represents the range of values that arise from performing the morphological erosion with three different tip radii (26nm, 28nm and 30nm). The FWHM is (74.4±2.8)nm, where the error is the standard deviation of FWHM measurements for each tip radius used. This is consistent with the (80±10)nm measured with TEM [170], thus showing that using an MEA enables the topography of MSNs to be accurately measured.

6.4.5 Whole-cell imaging with a morphological erosion correction

The lamellipodia and filopodia of U-87 MG cells imaged here have similar dimensions to the MSNs (heights of approximately 100nm and, in the case of filopodia, widths of approximately 100nm). It is thus argued that use of an MEA is necessary to accurately map the topography of these structures.

Figure 6.10 (a) shows the topography of part of a lamellipodium and filopodium before correction with the MEA. The spatial profile of the topography across the width of the filopodium is plot in figure 6.10 (c), showing a FWHM of 146.6nm. The topography after correction with the MEA is shown in figure 6.10 (b). The FWHM of the spatial profile across the filopodium at the same location is significantly reduced at (113.0±3.7)nm. This large change suggests that correction with an MEA could be important in studies in which measuring the morphology of lamellipodia and filopodia accurately is important.

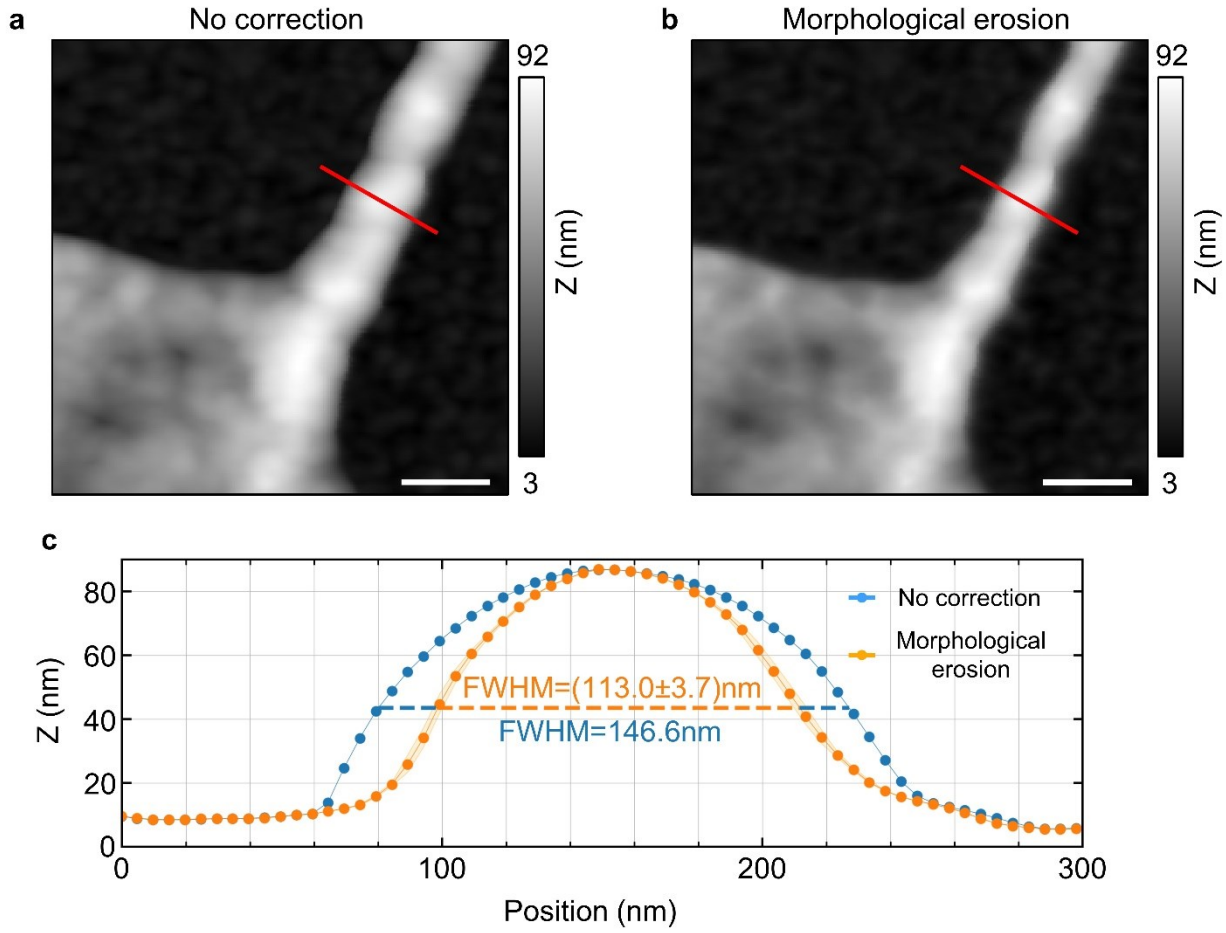

Figure 6.10 Correcting U-87 MG cell topography using a morphological erosion algorithm. ***(a,b)*** *Topography of the periphery of a U-87 MG cell before (a) and after (b) correction with a morphological erosion algorithm (MEA). The image dimensions are 1µm x 1µm with 5nm pixel size. A pixel integration time of 3ms was used and thus the image took approximately 17 minutes to acquire. The tapping amplitude was ~45nm.* ***(c)*** *Spatial profiles of the topography along the red lines in (a) and (b). Profiles are 1 pixel (5nm) wide. The error in the corrected profile is a result of performing the MEA with three different tip radii (26nm, 28nm and 30nm). Scale bars 200nm.*

The s-SNOM signal is strongly affected by changes in the contact point between the tip and the sample (that is, when the contact point moves away from the apex as shown in figure 6.7 (a)), as well as when there are multiple contact points between tip and sample [127]. The relationship between the s-SNOM signal and the sample topography can therefore be very complicated. Thus, s-SNOM images cannot be corrected with an MEA. However, s-SNOM images can be combined with topography images to exhibit more accurate cell morphology.

Topography and phase channels can be combined into a single quantity (for example, by multiplying them together) but then the mapping is no longer informative of cell chemistry. To preserve chemical information, s-SNOM images are here overlayed onto 3D images of cell topography. This is shown

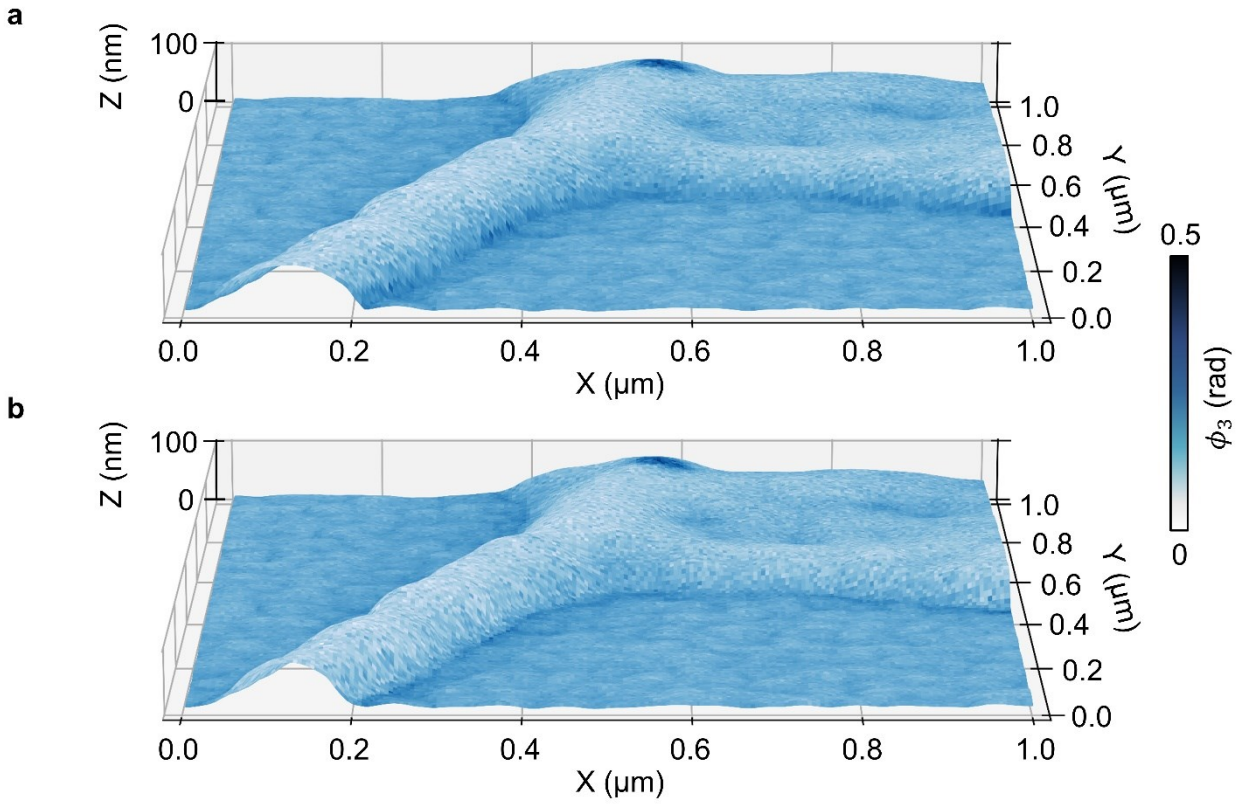

Figure 6.11 Combining chemical mapping and topography correction of a U-87 MG cell. *An s-SNOM image acquired at 1100cm^{-1} overlayed onto 3D surfaces of cell topography before (a) and after (b) correction with a morphological erosion algorithm. The image dimensions in X,Y are 1μm x 1μm with 5nm pixel size. A pixel integration time of 3ms was used and thus the image took approximately 17 minutes to acquire. The tapping amplitude was ~45nm.*

in figure 6.11 for the cell region shown in figure 6.10, where figure 6.11 (a) is the result using the unaltered topography image and figure 6.11 (b) is the result using the topography image that has been corrected with the MEA. The morphology in figure 6.11 (b) (notably the thinner filopodium) is a more accurate representation of the true cell morphology, whilst the chemical mapping remains unchanged.

6.5 Conclusions and further work

In this chapter, s-SNOM has been used as a tool for imaging interactions of MSNs with malignant glioma cells. The MSNs used are of great interest in the field of nanomedicine due to their biodegradability and biocompatibility. It has been shown here that s-SNOM can be used to map the distribution of MSNs in cells without the need for labelling of the particles or the cells. Further, the U-87 MG cells were imaged whole, allowing the morphology of lamellipodia and filopodia to be

obtained, which is important information in research areas relating to cell migration, cancer invasiveness and cell-cell transport.

By inspecting the topography of the cell surface at the locations of MSNs, it has been shown that embedded and internalised MSNs can be distinguished. This is crucial information when studying interactions between NPTs and cells, and an advantage of using s-SNOM over EM and fluorescence techniques, since the topographical information comes by default, rather than requiring complex 3D imaging techniques.

It has also been shown that a morphological erosion algorithm accounting for the limited sharpness of the imaging probe is required to accurately measure the topography of nanoparticles such as MSNs. It was argued that this also applies to lamellipodia and filopodia, due to them being similar in size to the MSNs. Further, overlaying of s-SNOM images onto three-dimensional representations of cell topography has been introduced as a means of presenting accurate cell morphology whilst preserving the chemical mapping.

Further work might incorporate correlative imaging with SEM. This would provide an independent measure of cell morphology to check the performance of the morphological erosion algorithm. It would also provide an independent mapping of the distribution of nanoparticles which could be used to check if s-SNOM can be used to image nanoparticles that are deep under the cell surface.

Further work should also focus on what kinds of chemical information can be obtained from whole cells. Whilst it is difficult to image intracellular structures in whole cells with s-SNOM, there are many applications in which chemical mapping of cell surfaces can reveal structures of interest. These include amyloid beta sheets in primary neurons, which are related to the development of Alzheimer's disease and have previously been imaged with s-SNOM [113].

Chapter 7

Conclusions and further work

7.1 Conclusions

The aim of this work was to show that s-SNOM can be used to image cells and intracellular structures with a spatial resolution that means it can rival EM and super-resolution microscopies, but with the significant advantage of providing chemical sensitivity without requiring samples to be stained and labelled. A range of relevant biological systems were imaged, including two types of human cells, as well as interactions between cells and nanoparticle theranostics used as nanomedicines.

In chapter 4, the label-free imaging capability of s-SNOM was demonstrated by imaging sections of multiple myeloma cells and comparing with EM images of stained cells of the same cell line. Several organelles and intracellular structures such as mitochondria, endoplasmic reticulum and nuclear components were identified directly optically at the nanoscale for the first time.

The rise/fall distance across the edges of biological structures was used as a measure of the spatial resolution achieved. Using this measure, the spatial resolution of images was shown to be ~30nm,

which beats diffraction by a factor of ~100 at the imaging wavelengths used. A more rigorous measurement of the achievable spatial resolution might involve imaging biological structures with known sizes, such as the nuclear pores that are used to demonstrate super-resolved microscopy [219].

Imaging at multiple wavelengths enabled the mapping of functional chemistry including amide groups in proteins and nucleobases and phosphodiester and C–O bonds in nucleic acids. The contrast in such images allows cells and intracellular structures to be visualised in terms of the concentration of the various chemical groups they contain, and such imaging could play a critical role in the future study of normal and pathological cell function. Specifically, the phase measurement, ϕ_3, was used in this thesis to compute the contrast between cellular regions. Here, it allowed the optimum imaging wavelength to be determined, but more generally this is a method of comparing the chemical content of different cells and subcellular components.

The resin embedding of samples used for much of this thesis – chosen for its ability to preserve biological samples extremely well – has been shown to be ideal for s-SNOM imaging and for making comparisons between s-SNOM and EM. However, it is important to note that the resin acts as a source of contrast in images which can be clearly seen when the imaging wavelength is tuned to that at which the resin absorbs strongly. This can be useful for mapping the cell density, but it also affects the signal measured at other wavelengths at which it is an unwanted background. In future, alternative embedding media and preparation methods such as cryogenic preparation of cells akin to cryo-EM should be investigated in an attempt to avoid issues associated with the embedding resin.

Demonstration of the specific detection of chemical species within cells, rather than sensitivity to chemical groups such as amides and phosphodiesters, would be a landmark of success for the bioimaging capabilities of s-SNOM. This might involve characterising the s-SNOM signals recorded for different known biomolecules, first in isolated environments and then inside cells. It is highly likely that nano-FTIR (that is, point spectroscopy localised to a s-SNOM probe using a broadband source) has a major part to play in this, since the identification of specific molecules, as in infrared spectroscopy, relies on interpretation of infrared spectra. Practically speaking, nano-FTIR is already frequently implemented into s-SNOM imaging setups, enabling the collection of infrared spectra at

multiple points within images [116]. The bulk of the work required to realise chemical specificity, then, lies in the analysis of the infrared spectra generated.

In chapter 5, interactions between gold nanoparticle theranostics and hippocampal neurons were imaged whilst simultaneously mapping cell chemistry. This provides another example of the application of s-SNOM to a real mammalian disease. s-SNOM images were once again accompanied by supporting EM images with the intention of driving more interest in s-SNOM amongst the bioimaging community. This investigation in particular demonstrates significant potential in nanomedicine whereby monitoring biochemical changes in cells in response to therapeutics, without needing to label the cells, might provide crucial information in the nanomedicine development process. In the interest of improving the quality of bioimaging in the s-SNOM community, it was also shown that osmicating samples might provide better structural and chemical integrity in samples, ultimately enabling higher resolution imaging with s-SNOM.

In chapter 6, mesoporous silica nanoparticles, which are promising due to their biodegradability and biocompatibility, were imaged interacting with malignant glioma cells. Inspecting the topography of the cell surface where MSNs were detected enabled the embedding status of the particles to be determined. This is the first time that s-SNOM has been used for this purpose and, given the relative ease of sample preparation in this case, it is quite possible that s-SNOM will in future be employed in this way to study the efficacy of a range of therapeutic nanostructures. Such investigations provide crucial information for nanomedicine development that can be hard to obtain using conventional imaging techniques, giving s-SNOM a niche in this area.

A morphological erosion algorithm was employed as part of the image processing in chapter 6. To the author's knowledge, this is the first time that such an algorithm has been applied to an s-SNOM investigation. It was shown that it is important to use such an algorithm to accurately represent the morphology of nanoparticles such as the MSNs used here. By extension, it is also important in accurately measuring cell morphology, and indeed there was a significant change to the measurement of the morphology of cells after the algorithm was applied. It is expected that such algorithms might become commonplace in imaging processing protocols for investigations of whole cells using s-SNOM.

7.2 Further work

Perhaps the most obvious and arguably the most accessible further work would be to implement a system for fully correlating s-SNOM images with an EM technique. This would provide further validation for the identifications of cell components and would be useful for all future s-SNOM applications in biological systems, whether in detecting chemical changes in pathological processes or mapping the distribution of nanoparticles in cells. Correlating the techniques might involve imaging serial sections with s-SNOM and TEM, or perhaps using SEM on s-SNOM samples after application of a conductive coating.

A much larger, high impact piece of work would be to use the chemical mapping capability of s-SNOM to generate insight into pathological changes that happen at the cellular level. For this, images of a large number of cells would need to be generated in order to collect statistics from a large sample size. Hopefully, this work serves as the groundwork for generating high quality images routinely. Related to this, future work might involve localising drugs applied to cells by leveraging their IR signatures. This would allow the operational mechanisms and efficacies of drugs to be studied, along with the biochemical response at the cellular level, all without modifying drugs or cells with fluorescent labels. It seems likely that machine learning models would be a useful tool in such studies, for example in classifying cancer presence and aggressiveness based on nanoscale chemical changes.

Another area of future work might be related to studying the dynamics of drug release from nanoparticle theranostics. This might begin with distinguishing particles carrying drug loads from those that are not, and eventually might lead to studying the dynamics and location of drug release as NPTs are internalised into cells. Correlating this information with biochemical changes in organelles would provide a huge amount of insight into the operation and efficacy of NPTs and thus have a huge impact in nanomedicine development.

Finally, work might also focus on applying s-SNOM to more types of samples, or perhaps to image intracellular structures in whole cells, with careful analysis [123] used to resolve the signal generated from regions below the cell membrane. There is also the possibility of imaging live cells [220],

although this introduces a number of technical challenges. More readily accessible is the potential for imaging FFPE prepared samples that can be prepared routinely by pathologists at a fraction of the time and cost of resin-embedded samples. In initial tests, it appears that intracellular structures are not preserved well enough by the FFPE process to benefit from imaging with s-SNOM. However, it might be that small adaptations to the process might result in well-preserved samples from which ultrastructural information can be obtained using s-SNOM.

Bibliography

1. Rayleigh, *XXXI. Investigations in optics, with special reference to the spectroscope.* The London, Edinburgh, and Dublin Philosophical Magazine and Journal of Science, 1879. **8**(49): p. 261-274.
2. Lipson, A., S.G. Lipson, and H. Lipson, *Optical Physics*. 2010: Cambridge University Press.
3. Lichtman, J.W. and J.-A. Conchello, *Fluorescence microscopy.* Nature methods, 2005. **2**(12): p. 910-919.
4. Ruska, H., B.v. Borries, and E. Ruska, *Die Bedeutung der übermikroskopie für die Virusforschung.* Archiv für die gesamte Virusforschung, 1939. **1**: p. 155-169.
5. Kruger, D.H., P. Schneck, and H.R. Gelderblom, *Helmut Ruska and the visualisation of viruses.* The Lancet, 2000. **355**(9216): p. 1713-1717.
6. Koster, A. and J. Klumperman, *Electron microscopy in cell biology: Integrating structure and function.* Nature reviews. Molecular cell biology, 2003. **Suppl**: p. SS6-10.
7. Goldsmith, C.S. and S.E. Miller, *Modern uses of electron microscopy for detection of viruses.* Clinical microbiology reviews, 2009. **22**(4): p. 552-563.
8. Graham, L. and J.M. Orenstein, *Processing tissue and cells for transmission electron microscopy in diagnostic pathology and research.* Nature protocols, 2007. **2**(10): p. 2439-2450.
9. Brunk, U., V.P. Collins, and E. Arro, *The fixation, dehydration, drying and coating of cultured cells for SEM.* Journal of microscopy, 1981. **123**(2): p. 121-131.
10. Goldstein, A., et al., *High resolution SEM imaging of gold nanoparticles in cells and tissues.* Journal of microscopy, 2014. **256**(3): p. 237-247.
11. Ng, C.T. and L. Gan, *Investigating eukaryotic cells with cryo-ET.* Molecular biology of the cell, 2020. **31**(2): p. 87-100.
12. Hermann, R., P. Walther, and M. Müller, *Immunogold labeling in scanning electron microscopy.* Histochemistry and Cell Biology, 1996. **106**(1): p. 31-39.
13. Peters, P.J., E. Bos, and A. Griekspoor, *Cryo-Immunogold Electron Microscopy.* Current Protocols in Cell Biology, 2006. **30**(1): p. 4.7.1-4.7.19.
14. Catelas, I., et al., *Comparison of in vitro with in vivo characteristics of wear particles from metal–metal hip implants.* Journal of Biomedical Materials Research Part B: Applied Biomaterials: An Official Journal of The Society for Biomaterials, The Japanese Society for Biomaterials, and The Australian Society for Biomaterials and the Korean Society for Biomaterials, 2004. **70**(2): p. 167-178.
15. Goode, A.E., et al., *Chemical speciation of nanoparticles surrounding metal-on-metal hips.* Chemical Communications, 2012. **48**(67): p. 8335-8337.
16. Rittweger, E., et al., *STED microscopy reveals crystal colour centres with nanometric resolution.* Nature Photonics, 2009. **3**(3): p. 144-147.
17. Sydor, A.M., et al., *Super-Resolution Microscopy: From Single Molecules to Supramolecular Assemblies.* Trends in Cell Biology, 2015. **25**(12): p. 730-748.
18. Heintzmann, R. and T. Huser, *Super-resolution structured illumination microscopy.* Chemical reviews, 2017. **117**(23): p. 13890-13908.
19. Hell, S.W. and J. Wichmann, *Breaking the diffraction resolution limit by stimulated emission: stimulated-emission-depletion fluorescence microscopy.* Optics Letters, 1994. **19**(11): p. 780-782.
20. Klar, T.A., et al., *Fluorescence microscopy with diffraction resolution barrier broken by stimulated emission.* Proceedings of the National Academy of Sciences, 2000. **97**(15): p. 8206-8210.
21. Göttfert, F., et al., *Coaligned dual-channel STED nanoscopy and molecular diffusion analysis at 20 nm resolution.* Biophysical journal, 2013. **105**(1): p. L01-L03.
22. Lelek, M., et al., *Single-molecule localization microscopy.* Nature Reviews Methods Primers, 2021. **1**(1): p. 39.

23. Betzig, E., et al., *Imaging Intracellular Fluorescent Proteins at Nanometer Resolution.* Science, 2006. **313**(5793): p. 1642-1645.
24. Hess, S.T., T.P.K. Girirajan, and M.D. Mason, *Ultra-high resolution imaging by fluorescence photoactivation localization microscopy.* Biophysical journal, 2006. **91**(11): p. 4258-4272.
25. Rust, M.J., M. Bates, and X. Zhuang, *Sub-diffraction-limit imaging by stochastic optical reconstruction microscopy (STORM).* Nature Methods, 2006. **3**(10): p. 793-796.
26. Paddock, S.W., *Principles and practices of laser scanning confocal microscopy.* Molecular biotechnology, 2000. **16**: p. 127-149.
27. Oreopoulos, J., R. Berman, and M. Browne, *Spinning-disk confocal microscopy: present technology and future trends.* Methods in cell biology, 2014. **123**: p. 153-175.
28. Weber, M., M. Mickoleit, and J. Huisken, *Light sheet microscopy*, in *Methods in cell biology*. 2014, Elsevier. p. 193-215.
29. Stelzer, E.H., et al., *Light sheet fluorescence microscopy.* Nature Reviews Methods Primers, 2021. **1**(1): p. 73.
30. Datta, R., et al., *Fluorescence lifetime imaging microscopy: fundamentals and advances in instrumentation, analysis, and applications.* Journal of biomedical optics, 2020. **25**(7): p. 071203-071203.
31. Berezin, M.Y. and S. Achilefu, *Fluorescence lifetime measurements and biological imaging.* Chemical reviews, 2010. **110**(5): p. 2641-2684.
32. Herman, B., et al., *Recent developments in monitoring calcium and protein interactions in cells using fluorescence lifetime microscopy.* Journal of Fluorescence, 1997. **7**: p. 85-91.
33. van Munster, E.B. and T.W. Gadella, *Fluorescence lifetime imaging microscopy (FLIM).* Microscopy Techniques: -/-, 2005: p. 143-175.
34. Hirvonen, L.M., et al., *Lightsheet fluorescence lifetime imaging microscopy with wide‐field time‐correlated single photon counting.* Journal of biophotonics, 2020. **13**(2): p. e201960099.
35. Thiele, J.C., et al., *Confocal fluorescence-lifetime single-molecule localization microscopy.* ACS nano, 2020. **14**(10): p. 14190-14200.
36. Wang, L., et al., *Resolution improvement in STED super-resolution microscopy at low power using a phasor plot approach.* Nanoscale, 2018. **10**(34): p. 16252-16260.
37. Sekar, R.B. and A. Periasamy, *Fluorescence resonance energy transfer (FRET) microscopy imaging of live cell protein localizations.* The Journal of cell biology, 2003. **160**(5): p. 629.
38. Martin, S.F., et al., *Quantitative analysis of multi‐protein interactions using FRET: Application to the SUMO pathway.* Protein Science, 2008. **17**(4): p. 777-784.
39. Loura, L.M. and M. Prieto, *FRET in membrane biophysics: An overview.* Frontiers in physiology, 2011. **2**: p. 82.
40. Lohse, M.J., S. Nuber, and C. Hoffmann, *Fluorescence/bioluminescence resonance energy transfer techniques to study G-protein-coupled receptor activation and signaling.* Pharmacological reviews, 2012. **64**(2): p. 299-336.
41. Bastiaens, P.I. and A. Squire, *Fluorescence lifetime imaging microscopy: spatial resolution of biochemical processes in the cell.* Trends in cell biology, 1999. **9**(2): p. 48-52.
42. Elangovan, M., R. Day, and A. Periasamy, *Nanosecond fluorescence resonance energy transfer‐fluorescence lifetime imaging microscopy to localize the protein interactions in a single living cell.* Journal of microscopy, 2002. **205**(1): p. 3-14.
43. Szalai, A.M., et al., *Super-resolution imaging of energy transfer by intensity-based STED-FRET.* Nano Letters, 2021. **21**(5): p. 2296-2303.
44. Dorling, K.M. and M.J. Baker, *Rapid FTIR chemical imaging: highlighting FPA detectors.* Trends in biotechnology, 2013. **31**(8): p. 437-438.
45. Walsh, M.J., et al. *High-resolution mid-infrared imaging for disease diagnosis*. in *Biomedical Vibrational Spectroscopy V: Advances in Research and Industry*. 2012. SPIE.
46. Kröger, N., et al., *Quantum cascade laser–based hyperspectral imaging of biological tissue.* Journal of biomedical optics, 2014. **19**(11): p. 111607-111607.
47. Kröger-Lui, N., et al., *Rapid identification of goblet cells in unstained colon thin sections by means of quantum cascade laser-based infrared microspectroscopy.* Analyst, 2015. **140**(7): p. 2086-2092.
48. Bassan, P., et al., *Large scale infrared imaging of tissue micro arrays (TMAs) using a tunable Quantum Cascade Laser (QCL) based microscope.* Analyst, 2014. **139**(16): p. 3856-3859.

49. Amrania, H., et al., *Digistain: a digital staining instrument for histopathology.* Optics Express, 2012. **20**(7): p. 7290.
50. Binnig, G., C.F. Quate, and C. Gerber, *Atomic force microscope.* Physical review letters, 1986. **56**(9): p. 930.
51. Grandbois, M., H. Clausen-Schaumann, and H. Gaub, *Atomic force microscope imaging of phospholipid bilayer degradation by phospholipase A2.* Biophysical journal, 1998. **74**(5): p. 2398-2404.
52. Medalsy, I., U. Hensen, and D.J. Muller, *Imaging and quantifying chemical and physical properties of native proteins at molecular resolution by force–volume AFM.* Angewandte Chemie International Edition, 2011. **50**(50): p. 12103-12108.
53. Stoffler, D., et al., *Calcium-mediated structural changes of native nuclear pore complexes monitored by time-lapse atomic force microscopy.* Journal of molecular biology, 1999. **287**(4): p. 741-752.
54. MuÈller, D.J. and A. Engel, *Voltage and pH-induced channel closure of porin OmpF visualized by atomic force microscopy.* Journal of molecular biology, 1999. **285**(4): p. 1347-1351.
55. Müller, D.J. and Y.F. Dufrêne, *Atomic force microscopy: a nanoscopic window on the cell surface.* Trends in cell biology, 2011. **21**(8): p. 461-469.
56. Lekka, M., et al., *Cancer cell detection in tissue sections using AFM.* Archives of biochemistry and biophysics, 2012. **518**(2): p. 151-156.
57. Dufrêne, Y.F., et al., *Imaging modes of atomic force microscopy for application in molecular and cell biology.* Nature Nanotechnology, 2017. **12**(4): p. 295-307.
58. Hu, X., et al., *Review on near-field detection technology in the biomedical field.* Advanced Photonics Nexus, 2023. **2**(4): p. 044002.
59. Stöckle, R.M., et al., *Nanoscale chemical analysis by tip-enhanced Raman spectroscopy.* Chemical Physics Letters, 2000. **318**(1-3): p. 131-136.
60. Bonhommeau, S., G.S. Cooney, and Y. Huang, *Nanoscale chemical characterization of biomolecules using tip-enhanced Raman spectroscopy.* Chem Soc Rev, 2022. **51**(7): p. 2416-2430.
61. Deckert-Gaudig, T., et al., *Spatially resolved spectroscopic differentiation of hydrophilic and hydrophobic domains on individual insulin amyloid fibrils.* Scientific Reports, 2016. **6**(1): p. 33575.
62. Pandey, Y., et al., *Nanoscale Chemical Imaging of Supported Lipid Monolayers using Tip-Enhanced Raman Spectroscopy.* Angewandte Chemie International Edition, 2021. **60**(35): p. 19041-19046.
63. Cialla, D., et al., *Raman to the limit: tip‐enhanced Raman spectroscopic investigations of a single tobacco mosaic virus.* Journal of Raman Spectroscopy: An International Journal for Original Work in all Aspects of Raman Spectroscopy, Including Higher Order Processes, and also Brillouin and Rayleigh Scattering, 2009. **40**(3): p. 240-243.
64. Neugebauer, U., et al., *On the way to nanometer‐sized information of the bacterial surface by tip‐enhanced Raman spectroscopy.* Chemphyschem: a European journal of chemical physics and physical chemistry, 2006. **7**(7): p. 1428-1430.
65. Watkins-Mariani, M., T. Deckert-Gaudig, and V. Deckert, *Label-free in vitro visualization and characterization of caveolar bulbs during stimulated re-epithelialization.* Analytical and bioanalytical chemistry, 2014. **406**: p. 6993-7002.
66. Lee, J., et al., *Visualizing vibrational normal modes of a single molecule with atomically confined light.* Nature, 2019. **568**(7750): p. 78-82.
67. Zhang, R., et al., *Chemical mapping of a single molecule by plasmon-enhanced Raman scattering.* Nature, 2013. **498**(7452): p. 82-86.
68. Kurouski, D., et al., *Infrared and Raman chemical imaging and spectroscopy at the nanoscale.* Chemical Society Reviews, 2020. **49**(11): p. 3315-3347.
69. Xiao, L. and Z.D. Schultz, *Spectroscopic imaging at the nanoscale: Technologies and recent applications.* Analytical chemistry, 2018. **90**(1): p. 440.
70. Clede, S., et al., *Detection of an estrogen derivative in two breast cancer cell lines using a single core multimodal probe for imaging (SCoMPI) imaged by a panel of luminescent and vibrational techniques.* Analyst, 2013. **138**(19): p. 5627-5638.

71. Dazzi, A. and C.B. Prater, *AFM-IR: Technology and Applications in Nanoscale Infrared Spectroscopy and Chemical Imaging.* Chemical Reviews, 2017. **117**(7): p. 5146-5173.
72. Perez-Guaita, D., et al., *Multispectral atomic force microscopy-infrared nano-imaging of malaria infected red blood cells.* Analytical chemistry, 2018. **90**(5): p. 3140-3148.
73. Quaroni, L., et al., *Mid-infrared spectroscopy and microscopy of subcellular structures in eukaryotic cells with atomic force microscopy–infrared spectroscopy.* RSC advances, 2018. **8**(5): p. 2786-2794.
74. Dazzi, A., et al., *Chemical mapping of the distribution of viruses into infected bacteria with a photothermal method.* Ultramicroscopy, 2008. **108**(7): p. 635-641.
75. Giliberti, V., et al., *Protein clustering in chemically stressed HeLa cells studied by infrared nanospectroscopy.* Nanoscale, 2016. **8**(40): p. 17560-17567.
76. Centrone, A., *Infrared imaging and spectroscopy beyond the diffraction limit.* Annual review of analytical chemistry, 2015. **8**: p. 101-126.
77. Ingham, J., et al., *An evaluation of the application of the aperture infrared SNOM technique to biomedical imaging.* Biomedical Physics & Engineering Express, 2018. **4**(2): p. 025011.
78. Smith, C.I., et al., *Application of a quantum cascade laser aperture scanning near-field optical microscope to the study of a cancer cell.* Analyst, 2018. **143**(24): p. 5912-5917.
79. Ingham, J., et al., *Submicron infrared imaging of an oesophageal cancer cell with chemical specificity using an IR-FEL.* Biomedical Physics & Engineering Express, 2018. **5**(1): p. 015009.
80. Andolfi, L., et al., *The crocidolite fibres interaction with human mesothelial cells as investigated by combining electron microscopy, atomic force and scanning near-field optical microscopy.* Journal of Microscopy, 2013. **249**(3): p. 173-183.
81. Andolfi, L., et al., *The application of scanning near field optical imaging to the study of human sperm morphology.* Journal of Nanobiotechnology, 2015. **13**(1): p. 2.
82. Ellis, B.G., et al., *Insight into metastatic oral cancer tissue from novel analyses using FTIR spectroscopy and aperture IR-SNOM.* Analyst, 2021. **146**(15): p. 4895-4904.
83. Prato, S., *SNOM on cell thin sections: observation of Jurkat and MDAMB453 cells.* Journal of Microscopy, 2007. **229**(2008): p. 440-446.
84. Lahrech, A., et al., *Infrared-reflection-mode near-field microscopy using an apertureless probe with a resolution of λ/600.* Optics Letters, 1996. **21**(17): p. 1315-1317.
85. Keilmann, F., *Vibrational-infrared near-field microscopy.* Vibrational Spectroscopy, 2002. **29**(1): p. 109-114.
86. Taubner, T., R. Hillenbrand, and F. Keilmann, *Nanoscale polymer recognition by spectral signature in scattering infrared near-field microscopy.* Applied Physics Letters, 2004. **85**(21): p. 5064-5066.
87. Raschke, M.B. and C. Lienau, *Apertureless near-field optical microscopy: Tip–sample coupling in elastic light scattering.* Applied Physics Letters, 2003. **83**(24): p. 5089-5091.
88. Zenhausern, F., M.P. O'Boyle, and H.K. Wickramasinghe, *Apertureless near-field optical microscope.* Applied Physics Letters, 1994. **65**(13): p. 1623-1625.
89. Zenhausern, F., Y. Martin, and H.K. Wickramasinghe, *Scanning Interferometric Apertureless Microscopy: Optical Imaging at 10 Angstrom Resolution.* Science, 1995. **269**(5227): p. 1083-1085.
90. Chen, X., et al., *Modern Scattering-Type Scanning Near-Field Optical Microscopy for Advanced Material Research.* Advanced Materials, 2019. **31**(24): p. 1804774.
91. Neuman, T., et al., *Mapping the near fields of plasmonic nanoantennas by scattering-type scanning near-field optical microscopy.* Laser & Photonics Reviews, 2015. **9**(6): p. 637-649.
92. Chen, J., et al., *Optical nano-imaging of gate-tunable graphene plasmons.* Nature, 2012. **487**(7405): p. 77-81.
93. Fei, Z., et al., *Gate-tuning of graphene plasmons revealed by infrared nano-imaging.* Nature, 2012. **487**(7405): p. 82-85.
94. Bohn, B.J., et al., *Near-field imaging of phased array metasurfaces.* Nano letters, 2015. **15**(6): p. 3851-3858.
95. Schnell, M., et al., *Real-space mapping of the chiral near-field distributions in spiral antennas and planar metasurfaces.* Nano letters, 2016. **16**(1): p. 663-670.

96. Rensberg, J., et al., *Active optical metasurfaces based on defect-engineered phase-transition materials.* Nano letters, 2016. **16**(2): p. 1050-1055.
97. Huber, A.J., et al., *Terahertz near-field nanoscopy of mobile carriers in single semiconductor nanodevices.* Nano letters, 2008. **8**(11): p. 3766-3770.
98. Huber, A., J. Wittborn, and R. Hillenbrand, *Infrared spectroscopic near-field mapping of single nanotransistors.* Nanotechnology, 2010. **21**(23): p. 235702.
99. Filimon, M., et al., *Smart polymer surfaces: mapping chemical landscapes on the nanometre scale.* Soft Matter, 2010. **6**(16): p. 3764-3768.
100. Pollard, B., et al., *Vibrational nano-spectroscopic imaging correlating structure with intermolecular coupling and dynamics.* Nature Communications, 2014. **5**(1): p. 3587.
101. Jiang, J., et al., *Protein Bricks: 2D and 3D Bio‐Nanostructures with Shape and Function on Demand.* Advanced Materials, 2018. **30**(20): p. 1705919.
102. Qin, N., et al., *Nanoscale probing of electron-regulated structural transitions in silk proteins by near-field IR imaging and nano-spectroscopy.* Nature communications, 2016. **7**(1): p. 13079.
103. Dominguez, G., et al., *Nanoscale infrared spectroscopy as a non-destructive probe of extraterrestrial samples.* Nature Communications, 2014. **5**(1): p. 5445.
104. Amenabar, I., et al., *Structural analysis and mapping of individual protein complexes by infrared nanospectroscopy.* Nature Communications, 2013. **4**(1): p. 2890.
105. O'Callahan, B.T., et al., *Ultrasensitive Tip- and Antenna-Enhanced Infrared Nanoscopy of Protein Complexes.* The Journal of Physical Chemistry C, 2019. **123**(28): p. 17505-17509.
106. Kopf, I., et al., *Detection of hybridization on nanografted oligonucleotides using scanning near-field infrared microscopy.* The Journal of Physical Chemistry C, 2010. **114**(2): p. 1306-1311.
107. Kästner, B., et al., *Infrared Nanospectroscopy of Phospholipid and Surfactin Monolayer Domains.* ACS Omega, 2018. **3**(4): p. 4141-4147.
108. Berweger, S., et al., *Nano-Chemical Infrared Imaging of Membrane Proteins in Lipid Bilayers.* Journal of the American Chemical Society, 2013. **135**(49): p. 18292-18295.
109. Paulite, M., et al., *Imaging Secondary Structure of Individual Amyloid Fibrils of a β2-Microglobulin Fragment Using Near-Field Infrared Spectroscopy.* Journal of the American Chemical Society, 2011. **133**(19): p. 7376-7383.
110. Qiao, Z., et al., *Infrared nanoimaging of nanoscale sliding dislocation of collagen fibrils.* Nano Research, 2021. **15**(3): p. 2355-2361.
111. Brehm, M., et al., *Infrared Spectroscopic Mapping of Single Nanoparticles and Viruses at Nanoscale Resolution.* Nano Letters, 2006. **6**(7): p. 1307-1310.
112. Mészáros, L.S., et al., *Spectroscopic investigations under whole-cell conditions provide new insight into the metal hydride chemistry of [FeFe]-hydrogenase.* Chemical Science, 2020. **11**(18): p. 4608-4617.
113. Freitas, R.O., et al., *Nano-Infrared Imaging of Primary Neurons.* Cells, 2021. **10**(10): p. 2559.
114. Tranca, D.E., et al., *Nanoscale mapping of refractive index by using scattering-type scanning near-field optical microscopy.* Nanomedicine: Nanotechnology, Biology and Medicine, 2018. **14**(1): p. 47-50.
115. Stanciu, S.G., et al., *Correlative imaging of biological tissues with apertureless scanning near-field optical microscopy and confocal laser scanning microscopy.* Biomedical Optics Express, 2017. **8**(12): p. 5374-5383.
116. Kanevche, K., et al., *Infrared nanoscopy and tomography of intracellular structures.* Commun Biol, 2021. **4**(1): p. 1341.
117. Novotny, L. and B. Hecht, *Principles of Nano-Optics*. 2012: Cambridge University Press.
118. Alonso, J.L. and W.H. Goldmann, *Feeling the forces: atomic force microscopy in cell biology.* Life sciences, 2003. **72**(23): p. 2553-2560.
119. Keilmann, F. and R. Hillenbrand, *Near-field microscopy by elastic light scattering from a tip.* Philosophical Transactions of the Royal Society of London. Series A: Mathematical, Physical and Engineering Sciences, 2004. **362**(1817): p. 787-805.
120. Cvitkovic, A., N. Ocelic, and R. Hillenbrand, *Analytical model for quantitative prediction of material contrasts in scattering-type near-field optical microscopy.* Optics Express, 2007. **15**(14): p. 8550.

121. Autore, M., et al., *Substrate Matters: Surface-Polariton Enhanced Infrared Nanospectroscopy of Molecular Vibrations.* Nano Letters, 2019. **19**(11): p. 8066-8073.
122. Aizpurua, J., et al., *Substrate-enhanced infrared near-field spectroscopy.* Optics Express, 2008. **16**(3): p. 1529.
123. Mester, L., et al., *Subsurface chemical nanoidentification by nano-FTIR spectroscopy.* Nature Communications, 2020. **11**(1): p. 3359.
124. Hauer, B., A.P. Engelhardt, and T. Taubner, *Quasi-analytical model for scattering infrared near-field microscopy on layered systems.* Optics Express, 2012. **20**(12): p. 13173.
125. Chen, X., et al., *Rigorous numerical modeling of scattering-type scanning near-field optical microscopy and spectroscopy.* Applied Physics Letters, 2017. **111**(22): p. 223110.
126. Chen, X., et al., *THz Near-Field Imaging of Extreme Subwavelength Metal Structures.* ACS Photonics, 2020. **7**(3): p. 687-694.
127. Babicheva, V.E., et al., *Near-field edge fringes at sharp material boundaries.* Optics Express, 2017. **25**(20): p. 23935.
128. Mastel, S., et al., *Understanding the Image Contrast of Material Boundaries in IR Nanoscopy Reaching 5 nm Spatial Resolution.* ACS Photonics, 2018. **5**(8): p. 3372-3378.
129. Maissen, C., et al., *Probes for Ultrasensitive THz Nanoscopy.* ACS Photonics, 2019. **6**(5): p. 1279-1288.
130. Huth, F., et al., *Nano-FTIR Absorption Spectroscopy of Molecular Fingerprints at 20 nm Spatial Resolution.* Nano Letters, 2012. **12**(8): p. 3973-3978.
131. Faist, J., et al., *Quantum cascade laser.* Science, 1994. **264**(5158): p. 553-556.
132. Maulini, R., et al., *Broadband tuning of external cavity bound-to-continuum quantum-cascade lasers.* Applied Physics Letters, 2004. **84**(10): p. 1659-1661.
133. Ocelic, N., A. Huber, and R. Hillenbrand, *Pseudoheterodyne detection for background-free near-field spectroscopy.* Applied Physics Letters, 2006. **89**(10): p. 101124.
134. Hillenbrand, R., T. Taubner, and F. Keilmann, *Phonon-enhanced light–matter interaction at the nanometre scale.* Nature, 2002. **418**(6894): p. 159-162.
135. Mester, L., A.A. Govyadinov, and R. Hillenbrand, *High-fidelity nano-FTIR spectroscopy by on-pixel normalization of signal harmonics.* Nanophotonics, 2021. **11**(2): p. 377-390.
136. Govyadinov, A.A., et al., *Quantitative measurement of local infrared absorption and dielectric function with tip-enhanced near-field microscopy.* The journal of physical chemistry letters, 2013. **4**(9): p. 1526-1531.
137. Wang, H., L. Wang, and X.G. Xu, *Scattering-type scanning near-field optical microscopy with low-repetition-rate pulsed light source through phase-domain sampling.* Nature Communications, 2016. **7**(1): p. 13212.
138. Stuart, B.H., *Infrared Spectroscopy: Fundamentals and Applications: Stuart/Infrared Spectroscopy: Fundamentals and Applications*. Analytical Techniques in the Sciences. 2004, Chichester, UK: John Wiley & Sons, Ltd.
139. Movasaghi, Z., S. Rehman, and D.I. ur Rehman, *Fourier Transform Infrared (FTIR) Spectroscopy of Biological Tissues.* Applied Spectroscopy Reviews, 2008. **43**(2): p. 134-179.
140. Griffiths, P.R., *Fourier transform infrared spectrometry.* Science, 1983. **222**(4621): p. 297-302.
141. Amarie, S., T. Ganz, and F. Keilmann, *Mid-infrared near-field spectroscopy.* Optics Express, 2009. **17**(24): p. 21794-21801.
142. Water vapour infrared absorption spectrum. HITRAN. Atomic and Molecular Physics Division, Harvard-Smithsonian Center for Astrophysics. https://hitran.iao.ru/. Access date: 11/07/23.
143. Krutokhvostov, R., et al., *Enhanced resolution in subsurface near-field optical microscopy.* Optics Express, 2012. **20**(1): p. 593-600.
144. Taubner, T., F. Keilmann, and R. Hillenbrand, *Effect of tip modulation on image contrast in scattering-type near-field optical microscopy.* Journal of the Korean Physical Society, 2005. **47**(9): p. 213.
145. Hauer, B., A.P. Engelhardt, and T. Taubner, *Quasi-analytical model for scattering infrared near-field microscopy on layered systems.* Optics Express, 2012. **20**(12): p. 13173-13188.
146. Kuo, J., *Electron Microscopy: Methods and Protocols*. Second Edition ed. Methods in Molecular Biology. 2007, Totowa, NJ: Humana Press Inc.

147. Lau, L., et al., *STED microscopy with optimized labeling density reveals 9-fold arrangement of a centriole protein.* Biophys J, 2012. **102**(12): p. 2926-35.
148. Sahl, S.J., S.W. Hell, and S. Jakobs, *Fluorescence nanoscopy in cell biology.* Nat Rev Mol Cell Biol, 2017. **18**(11): p. 685-701.
149. Hink, M.A., et al., *Structural Dynamics of Green Fluorescent Protein Alone and Fused with a Single Chain Fv Protein*.* Journal of Biological Chemistry, 2000. **275**(23): p. 17556-17560.
150. Auner, H.W. and S. Cenci, *Recent advances and future directions in targeting the secretory apparatus in multiple myeloma.* British Journal of Haematology, 2015. **168**(1): p. 14-25.
151. Greaves, G.E., et al., *Label-free nanoscale mapping of intracellular organelle chemistry.* Communications Biology, 2023. **6**(1): p. 583.
152. Zlei, M., et al., *Characterization of in vitro growth of multiple myeloma cells.* Experimental Hematology, 2007. **35**(10): p. 1550-1561.
153. Chow, K.-H., R.E. Factor, and K.S. Ullman, *The nuclear envelope environment and its cancer connections.* Nature Reviews Cancer, 2012. **12**(3): p. 196-209.
154. Ochs, R., et al., *Fibrillarin: a new protein of the nucleolus identified by autoimmune sera.* Biology of the Cell, 1985. **54**(2): p. 123-133.
155. Ginisty, H., F. Amalric, and P. Bouvet, *Nucleolin functions in the first step of ribosomal RNA processing.* The EMBO journal, 1998. **17**(5): p. 1476-1486.
156. Biggiogera, M., et al., *Simultaneous immunoelectron microscopic visualization of protein B23 and C23 distribution in the HeLa cell nucleolus.* Journal of Histochemistry & Cytochemistry, 1989. **37**(9): p. 1371-1374.
157. Gerace, L. and B. Burke, *Functional organization of the nuclear envelope.* Annual review of cell biology, 1988. **4**(1): p. 335-374.
158. Kornberg, R.D., *Chromatin Structure: A Repeating Unit of Histones and DNA.* Science, 1974. **184**(4139): p. 868-871.
159. Sirri, V., et al., *Nucleolus: the fascinating nuclear body.* Histochemistry and Cell Biology, 2008. **129**(1): p. 13-31.
160. McBride, H.M., M. Neuspiel, and S. Wasiak, *Mitochondria: More Than Just a Powerhouse.* Current Biology, 2006. **16**(14): p. R551-R560.
161. Schwarz, D.S. and M.D. Blower, *The endoplasmic reticulum: structure, function and response to cellular signaling.* Cellular and Molecular Life Sciences, 2016. **73**(1): p. 79-94.
162. Amrania, H., et al., *Mid-infrared imaging in breast cancer tissue: an objective measure of grading breast cancer biopsies.* Convergent Science Physical Oncology, 2018. **4**(2): p. 025001.
163. Belhassen, J., et al., *Toward augmenting tip-enhanced nanoscopy with optically resolved scanning probe tips.* Advanced Photonics Nexus, 2023. **2**(2): p. 026002.
164. Califf, R.M., *Biomarker definitions and their applications.* Experimental Biology and Medicine, 2018. **243**(3): p. 213-221.
165. Petrov, M. and I. Sokolov, *Identification of Geometrical Features of Cell Surface Responsible for Cancer Aggressiveness: Machine Learning Analysis of Atomic Force Microscopy Images of Human Colorectal Epithelial Cells.* Biomedicines, 2023. **11**(1): p. 191.
166. Sim, S. and N.K. Wong, *Nanotechnology and its use in imaging and drug delivery.* Biomedical reports, 2021. **14**(5): p. 1-9.
167. Chen, F., E.B. Ehlerding, and W. Cai, *Theranostic nanoparticles.* Journal of Nuclear Medicine, 2014. **55**(12): p. 1919-1922.
168. Gao, Q., et al., *Gold nanoparticles in cancer theranostics.* Frontiers in bioengineering and biotechnology, 2021. **9**: p. 647905.
169. Chen, F., et al., *Multifunctional nanomedicine with silica: Role of silica in nanoparticles for theranostic, imaging, and drug monitoring.* Journal of colloid and interface science, 2018. **521**: p. 261-279.
170. Pinna, A., et al., *Nanoceria provides antioxidant and osteogenic properties to mesoporous silica nanoparticles for osteoporosis treatment.* Acta Biomaterialia, 2021. **122**: p. 365-376.
171. Morfill, C., et al., *Nanostars Carrying Multifunctional Neurotrophic Dendrimers Protect Neurons in Preclinical In Vitro Models of Neurodegenerative Disorders.* ACS Applied Materials & Interfaces, 2022. **14**(42): p. 47445-47460.

172. Pujals, S. and L. Albertazzi, *Super-resolution microscopy for nanomedicine research.* ACS nano, 2019. **13**(9): p. 9707-9712.
173. Augustine, R., et al., *Cellular uptake and retention of nanoparticles: Insights on particle properties and interaction with cellular components.* Materials Today Communications, 2020. **25**: p. 101692.
174. Zhang, C., et al., *Antibiotic-derived lipid nanoparticles to treat intracellular Staphylococcus aureus.* ACS applied bio materials, 2019. **2**(3): p. 1270-1277.
175. Simonsen, J.B. and E.B. Kromann, *Pitfalls and opportunities in quantitative fluorescence-based nanomedicine studies–A commentary.* Journal of Controlled Release, 2021. **335**: p. 660-667.
176. Valente, P., et al., *Conopeptide-Functionalized Nanoparticles Selectively Antagonize Extrasynaptic N-Methyl-d-aspartate Receptors and Protect Hippocampal Neurons from Excitotoxicity In Vitro.* ACS Nano, 2020. **14**(6): p. 6866-6877.
177. Stanciu, S.G., et al., *Scattering-type scanning near-field optical microscopy of polymer-coated gold nanoparticles.* ACS omega, 2022. **7**(13): p. 11353-11362.
178. Sztandera, K., M. Gorzkiewicz, and B. Klajnert-Maculewicz, *Gold nanoparticles in cancer treatment.* Molecular pharmaceutics, 2018. **16**(1): p. 1-23.
179. Elahi, N., M. Kamali, and M.H. Baghersad, *Recent biomedical applications of gold nanoparticles: A review.* Talanta, 2018. **184**: p. 537-556.
180. Zhang, J., D. Khanal, and M.M.B. Holl, *Applications of AFM-IR for drug delivery vector characterization: infrared, thermal, and mechanical characterization at the nanoscale.* Advanced Drug Delivery Reviews, 2022. **192**: p. 114646.
181. Pancani, E., et al., *High-Resolution Label-Free Detection of Biocompatible Polymeric Nanoparticles in Cells.* Particle & Particle Systems Characterization, 2018. **35**(3): p. 1700457.
182. Mathurin, J., et al., *Photothermal AFM-IR spectroscopy and imaging: Status, challenges, and trends.* Journal of Applied Physics, 2022. **131**(1): p. 010901.
183. Dmytriyeva, O., et al., *The metastasis-promoting S100A4 protein confers neuroprotection in brain injury.* Nature Communications, 2012. **3**(1): p. 1197.
184. Wigglesworth, V.B., *The use of osmium in the fixation and staining of tissues.* Proceedings of the Royal Society of London. Series B-Biological Sciences, 1957. **147**(927): p. 185-199.
185. Greaves, G., et al., *Infrared nanoimaging of neuronal ultrastructure and nanoparticle interaction with cells.* Nanoscale, 2024.
186. Yuan, H., et al., *Gold nanostars: surfactant-free synthesis, 3D modelling, and two-photon photoluminescence imaging.* Nanotechnology, 2012. **23**(7): p. 075102.
187. Soroka, V., et al., *Induction of neuronal differentiation by a peptide corresponding to the homophilic binding site of the second Ig module of the neural cell adhesion molecule.* Journal of Biological Chemistry, 2002. **277**(27): p. 24676-24683.
188. Osmium tetroxide infrared absorption spectrum. SpectraBase. Bio-Rad Laboratories. https://spectrabase.com/spectrum/D56i42YKluX. Access date: 13/06/23. (CAS RN: 20816-12-0)
189. Kwon, S., et al., *Silica-based mesoporous nanoparticles for controlled drug delivery.* Journal of tissue engineering, 2013. **4**: p. 2041731413503357.
190. Liu, Y., B. Zhang, and B. Yan, *Enabling anticancer therapeutics by nanoparticle carriers: the delivery of Paclitaxel.* International journal of molecular sciences, 2011. **12**(7): p. 4395-4413.
191. Lu, J., et al., *Mesoporous Silica Nanoparticles as a Delivery System for Hydrophobic Anticancer Drugs.* Small, 2007. **3**(8): p. 1341-1346.
192. Slowing, I.I., et al., *Mesoporous silica nanoparticles as controlled release drug delivery and gene transfection carriers.* Advanced Drug Delivery Reviews, 2008. **60**(11): p. 1278-1288.
193. Chu, Z., et al., *Cellular uptake, evolution, and excretion of silica nanoparticles in human cells.* Nanoscale, 2011. **3**(8): p. 3291-3299.
194. Phillips, E., et al., *Clinical translation of an ultrasmall inorganic optical-PET imaging nanoparticle probe.* Sci Transl Med, 2014. **6**(260): p. 260ra149.
195. Anselmo, A.C. and S. Mitragotri, *Nanoparticles in the clinic.* Bioeng Transl Med, 2016. **1**(1): p. 10-29.
196. Chan, W.T., et al., *In vivo toxicologic study of larger silica nanoparticles in mice.* Int J Nanomedicine, 2017. **12**: p. 3421-3432.

197. Zhai, W., et al., *Degradation of hollow mesoporous silica nanoparticles in human umbilical vein endothelial cells.* J Biomed Mater Res B Appl Biomater, 2012. **100**(5): p. 1397-403.
198. Gunduz, O., et al., *Mesoporous materials used in medicine and environmental applications.* Curr Top Med Chem, 2015. **15**(15): p. 1501-1515.
199. Ritter, H., J.H. Ramm, and D. Brühwiler, *Influence of the Structural Properties of Mesoporous Silica on the Adsorption of Guest Molecules.* Materials (Basel), 2010. **3**(8): p. 4500-4509.
200. Zhou, Y., et al., *Mesoporous silica nanoparticles for drug and gene delivery.* Acta Pharm Sin B, 2018. **8**(2): p. 165-177.
201. Vallet-Regí, M., et al., *Bone-regenerative bioceramic implants with drug and protein controlled delivery capability.* Progress in Solid State Chemistry, 2008. **36**(3): p. 163-191.
202. Guo, H., et al., *Hollow mesoporous silica nanoparticles for intracellular delivery of fluorescent dye.* Chemistry Central Journal, 2011. **5**: p. 1-10.
203. Cheng, W.-Y., et al., *Luteolin inhibits migration of human glioblastoma U-87 MG and T98G cells through downregulation of Cdc42 expression and PI3K/AKT activity.* Molecular biology reports, 2013. **40**: p. 5315-5326.
204. Civita, P., D. M. Leite, and G.J. Pilkington, *Pre-clinical drug testing in 2D and 3D human in vitro models of glioblastoma incorporating non-neoplastic astrocytes: tunneling nano tubules and mitochondrial transfer modulates cell behavior and therapeutic response.* International Journal of Molecular Sciences, 2019. **20**(23): p. 6017.
205. Zhang, W. and Y. Chen, *Visibility of subsurface nanostructures in scattering-type scanning near-field optical microscopy imaging.* Optics Express, 2020. **28**(5): p. 6696-6707.
206. Stöber, W., A. Fink, and E. Bohn, *Controlled growth of monodisperse silica spheres in the micron size range.* Journal of colloid and interface science, 1968. **26**(1): p. 62-69.
207. Grün, M., I. Lauer, and K.K. Unger, *The synthesis of micrometer-and submicrometer-size spheres of ordered mesoporous oxide MCM-41.* Advanced Materials, 1997. **9**(3): p. 254-257.
208. Jacquemet, G., H. Hamidi, and J. Ivaska, *Filopodia in cell adhesion, 3D migration and cancer cell invasion.* Current opinion in cell biology, 2015. **36**: p. 23-31.
209. Small, J.V., et al., *The lamellipodium: where motility begins.* Trends in Cell Biology, 2002. **12**(3): p. 112-120.
210. Mattila, P.K. and P. Lappalainen, *Filopodia: molecular architecture and cellular functions.* Nature Reviews Molecular Cell Biology, 2008. **9**(6): p. 446-454.
211. Khurana, S. and S.P. George, *The role of actin bundling proteins in the assembly of filopodia in epithelial cells.* Cell Adhesion & Migration, 2011. **5**(5): p. 409-420.
212. Mehmood, Y., et al., *Facile synthesis of mesoporous silica nanoparticles using modified sol-gel method: Optimization and in vitro cytotoxicity studies.* Pak. J. Pharm. Sci, 2019. **32**(4): p. 1805-1812.
213. Liu, F., et al., *Outside-in stepwise functionalization of mesoporous silica nanocarriers for matrix type sustained release of fluoroquinolone drugs.* Journal of Materials Chemistry B, 2015. **3**(10): p. 2206-2214.
214. MICA infrared absorption spectrum. SpectraBase. Bio-Rad Laboratories. https://spectrabase.com/spectrum/4Uhr8i2p6ST. Access date: 23/06/23. (CAS RN: 12001-26-2)
215. Miranda, K., et al., *Three dimensional reconstruction by electron microscopy in the life sciences: An introduction for cell and tissue biologists.* Molecular Reproduction and Development, 2015. **82**(7-8): p. 530-547.
216. Sauer, M. and M. Heilemann, *Single-Molecule Localization Microscopy in Eukaryotes.* Chemical Reviews, 2017. **117**(11): p. 7478-7509.
217. Udpa, L., et al., *Deconvolution of atomic force microscopy data for cellular and molecular imaging.* IEEE Signal Processing Magazine, 2006. **23**(3): p. 73-83.
218. Villarrubia, J.S., *Morphological estimation of tip geometry for scanned probe microscopy.* Surface science, 1994. **321**(3): p. 287-300.
219. Thevathasan, J.V., et al., *Nuclear pores as versatile reference standards for quantitative superresolution microscopy.* Nature Methods, 2019. **16**(10): p. 1045-1053.
220. Kaltenecker, K.J., et al., *Infrared-spectroscopic, dynamic near-field microscopy of living cells and nanoparticles in water.* Scientific Reports, 2021. **11**(1): p. 21860.